RARE-EARTH DOPED APATITE NANOCRYSTALS FOR CELL AND IMPLANTED BIOMATERIAL TRACKING

A Dissertation
Presented to
The Academic Faculty

by

Xiyu Li

In Partial Fulfillment
of the Requirements for the Degree
Doctor of Philosophy in the
Department of Biomedical Engineering
College of Engineering

Peking University/Georgia Institute of Technology/Emory University
August 2016

RARE-EARTH DOPED APATITE NANOCRYSTALS FOR CELL AND IMPLANTED BIOMATERIAL TRACKING

Approved by:

Dr. Haifeng Chen, Advisor
Department of Biomedical
Peking University

Dr. Younan Xia, Co-advisor
Department of Biomedical
Georgia Institute of Technology

Dr. Ying Luo
Department of Biomedical
Peking University

Dr. Xiaojie Duan
Department of Biomedical
Peking University

Dr. Yingfang Ao
Institute of Sports Medicine
Peking University Third Hospital

Date Approved: June 2, 2016

To my parents

ACKNOWLEDGEMENTS

Firstly, I would like to express my sincere thanks to my advisors Dr. Haifeng Chen and Dr. Younan Xia for their guidance and help during my journey of pursuing the Ph.D. degree. Since 2011, I came to Dr. Chen's lab and conducted research under his direct. He widened my horizon for science and I learned a lot from him on how to be a contributive researcher and meanwhile a responsible man. I spent one year in Dr. Xia's lab from 2014. I also learned so much from him on pursuing perfect and high efficiency. Thanks for their support and the Wallace H. Coulter Foundation on the PKU/Georgia Tech/Emory Joint Ph.D. program. And I would like to thank my thesis committee members: Dr. Ying Luo, Dr. Xiaojie Duan, and Dr. Yingfang Ao.

I would like to especially thank my mother and father; they have always been my biggest support through these years. I would like to share with them my happiness as well as frustration. They respected my decisions and got my back. I love my parents, and will love them more in future.

I would also like to thank my colleagues and friends form both Beijing and Atlanta. They have been really kind and helpful throughout these years. I would like to thank Juan Wang, Muyang Sun, Alice Cheng, Xiaokun Wang, Shize Liu, Lin Yin, Qinghuan Ji, and Nier Wu from Chen lab, PKU; Wenying Liu, Chunlei Zhu, Jessica from Xia lab, Ga tech. And my friends Kedi Zhou, Jinyang Wang (PKU), Anqi Jiao, Honglin Ren (GSU), Yanbo Liu (Emory) etc. helped me to adapt to the new environment when I just arrived to Atlanta and we shared happy time together.

I would like to thank collaborators for their support and help: Haifeng Zeng, Xie fang from Dr. Li Teng's lab at Plastic Surgery Hospital of Peking Union Medical College and Chinese Academy of Medical Sciences, Jingxian Zhu, Xiaoqing Hu from Dr. Yingfang Ao's lab at Peking University Third Hospital. I would like to thank Xuemei Li for guiding me how to operate TEM, and Qin Zhou for cell and animal experiments.

I would like to thank Dr. Cheng Zhu for setting up and running the joint program, and thank Jialei Luo and Shannon Sullivan for the administration work help.

TABLE OF CONTENTS

Page

LIST OF TABLES

Page

LIST OF FIGURES

Page

LIST OF SYMBOLS AND ABBREVIATIONS

©	A vacancy of Ca site
ALP	Alkaline phosphatase
BCP	Biphasic calcium phosphate
BMSCs	Bone marrow mesenchymal stem cells
CT	Computed tomography
DCCBM	Decalcified cortical-cancellous bone matrix
EDS	Energy dispersive spectroscopy
EDTA	Ethylene diamine tetraacetic acid
ESA	Excited state absorption
ESEM	Environmental scanning electron microscopy
ETU	Energy transfer upconversion
FA	Fluorapatite
FT-IR	Fourier transform infrared spectroscopy
HA	Hydroxyapatite
HAp	Poorly crystalline HA
HAx	Highly crystalline HA
HRTEM	High resolution transmission electron microscopy
ICP-OES	Inductively coupled plasma optical emission spectroscopy
Ln	Lanthanides (Tb, Eu, Yb, Ho etc.)
MG63	An osteoblastic cell from human osteosarcoma

MRI	Magnetic resonance imaging
MTT	3-[4,5-dimethylthiazol-2yl]-2,5-diphenyl-2H-tetrazoliumbromide
NIR	Near-infrared
NPs	Nanoparticles
OCT	Optical coherence tomography
PAA	Polyacrylic acid
PCL	Poly (ε-caprolactone)
PCR	Polymerase chain reaction
PET	Positron emission tomography
PLGA	Poly (lactic-co-glycolic acid)
QDs	Quantum dots
SAED	Selected area electron diffraction
SAXS	Small-angle X-ray scattering
SDS	Sodium dodecyl sulphate
SEM	Scanning electron microscope
SPECT	Single photon emission computed tomography.
TEM	Transmission electron microscope
UCNPs	Upconversion nanoparticles
UV	Ultraviolet
XRD	X-ray diffraction

SUMMARY

Apatite nanoparticles are the main inorganic component of human hard tissues, and have been used in repair of bone defects or scaffolds for bone tissue engineering. It has a stable hexagonal crystal structure, which could be employed as a host matrix for lanthanides doping to prepare both downconversion and upconversion fluorescent nanoparticles. In the thesis, lanthanide doped apatite nanoparticles have been prepared by hydrothermal synthesis, and their structure, luminescence properties, cell proliferation, and their fluorescent tracking *in vitro* and *in vivo* have been investigated. The novel apatite fluorescence probe is expected to overcome the shortcomings such as instability and photobleaching of organic fluorophores, and the potential toxicity from quantum dots.

The terbium (Tb) doped fluorapatite (FA:Tb) and hydroxyapatite (HA:Tb) nanocrystals with a uniform slender morphology exhibit bright green fluorescence, good cytocompatibility and excellent cell imaging capacity, providing feasibility for imaging and tracking of cells with multilineage differentiation. The Yb^{3+}/Ho^{3+} co-doped apatite nanoparticles are firstly prepared with both green and red upconversion emissions under 980 nm near-infrared excitation. The 543 and 654 nm upconversion emission signals could be assigned, respectively, to $^5F_4$ ($^5S_2$) - $^5I_8$ and $^5F_5$ - $^5I_8$ transitions of holmium after energy transfer from ytterbium under 980 nm excitation. The FA:Yb^{3+}/Ho^{3+} results in a superior green luminescence, while HA:Yb^{3+}/Ho^{3+} dominates in red emission. The difference in green and red emission behavior between FA:Yb^{3+}/Ho^{3+} and HA:Yb^{3+}/Ho^{3+} is dependent on their lattice structure and composition. Several reasonable lanthanide embedding lattice models along the fluorine channel or hydroxyl channel of FA or HA crystal cell are proposed, and reveal a necessity for coexistent substitution mechanism.

The upconversion apatite nanoparticles are used for the first time to clearly distinguish the implanted material from bone tissue, and to track their respective distribution *in vivo*. The superposition of fluorescent images including the upconversion apatite and the Masson's stained bone tissue indicates that new bone tissue could grow into the interval space between the apatite particles and fully integrate with these particles. The upconversion material and fluorescence superposition method provide a novel strategy for long-term discriminable fluorescence tracking of implanted materials and scaffolds.

These fluorescent apatite nanoparticles can not only form bonding with bone tissue, but also provide stable and clear fluorescence, which can be utilized for long-term bioimaging, distinguishing scaffold from newly formed bone tissue or identifying the interface between implanted material and bone tissue, and tracking the distribution of degraded scaffold fragments *in vivo*. Both the lanthanide doped apatite nanoparticles and the method presented in this research will have a promising prospect for future biomedical applications.

CHAPTER 1 INTRODUCTION

Overview aims

Bone tissue engineering have been the hot topics of biomaterial research in recent years, in which hydroxyapatite usually acts as the bioactive component, mainly due to the fact that the inorganic constituent of human calcified tissues is from apatite crystals.[1, 2] Synthetic apatites, including hydroxyapatite [$Ca_{10}(PO_4)_6(OH)_2$, HA] and fluorapatite [$Ca_{10}(PO_4)_6F_2$, FA], have been widely used as defect fillers of bones and teeth or component of tissue engineering scaffolds based on their good biocompatibility and bone-bonding capacity.[3, 4] We already know that the bone mesenchymal stem cells (BMSCs) can differentiate into osteoblasts or chondrogenic cells and play an important role during osteogenesis. However, we lack a tracer method to see how BMSCs can differentiate into osteoblasts or chondrogenic cells. We also know that, the implanted apatite-based biomaterials can bond with bone tissue or undergo degradation while the formation of new bone, but how the apatite biomaterials are involved in bone regeneration and what happens during the process are still unclear.

The specific aims of this research is to design and prepare new fluorescent probes based on rare earth doped apatite nanoparticles to track the differentiation and osteogenic processes of cells and bony tissues, including selecting right doping matrix and dopants, evaluating the system and tracking the cells and implanted biomaterials.

Background

Bone tissue engineering technology has significantly evolved with nanoscale strategies for materials construction and synergetic strategies for combining with cells and

molecules.[5, 6] Thus tissue engineers need versatile imaging tools to assess the construction, including morphology and interactions with cells and tissue. Numerous studies still use conventional methods, such as Hematoxylin and eosin (H&E) or Masson's staining to distinguish the newly formed bone tissue on the histological section of scaffolds.[3] However, it is invasive and provides limited information especially in the case of *in vivo* approaches;[7] it is difficult to clearly distinguish the scaffold material and material-tissue interface on these histological sections. Previous studies have used environmental scanning electron microscopy (ESEM) to distinguish the newly mineralized bone from the biphasic calcium phosphate (BCP) scaffold during osteogenesis based on the image grey values.[8] However, this method only provides a limited field of view, hardly allowing a full correlative investigation on changes in the ultrastructure over a macroscopic sample. Small-angle X-ray scattering (SAXS) remains constrained to isotropically oriented ultrastructures.[9] Therefore, novel methods are needed to distinguish the scaffold from the newly formed bone tissue.

Figure 1-1 briefly presents common imaging methods with their own range of imaging depth and the information they can provide，including magnetic resonance imaging (MRI), X-ray computed tomography (CT), positron emission tomography (PET), single photon emission computed tomography (SPECT), ultrasound and photoacoustic imaging, optical coherence tomography (OCT), optical imaging including upconversion (UC) luminescence imaging. CT, PET, and SPECT are radiodiagnostic modes, and MRI needs large concentration of contrast agents, though some improvement has been achieved.[10] Fluorescence microscopy has been the most commonly used imaging tools on *in vitro* studies, *ex vivo* verification including histology.[11] Owing to high sensitivity and spatial

resolution, fluorescence microscopy has been used to distinguish matrix and matrix-embedded cells.[12] Two-photon fluorescence microscopy involving near-infrared wavelengths can increase penetration depth up to ~500 μm, and decrease photodamage and photobleaching because they occur only at the focus of the beam.[13, 14] Mesenchymal stem cells embedded in various environments[15] and scaffolds[16] can be monitored using two-photon fluorescence microscopy. Therefore, incorporating fluorescence into scaffolds is one prospective strategy for achieving the purpose in this thesis.

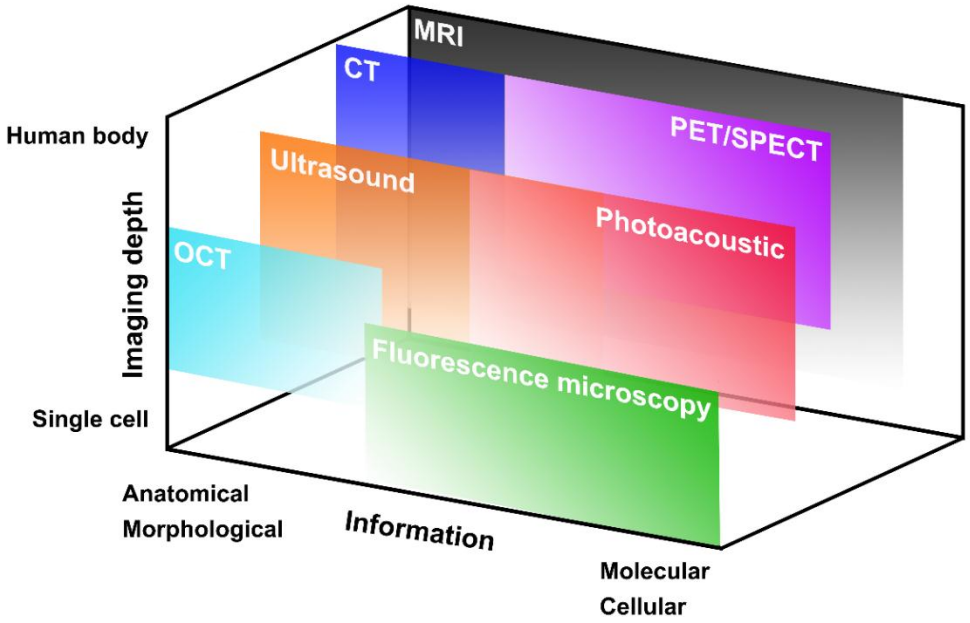

Figure 1-1 Imaging depth and information for various imaging modalities.

Fluorescent probes

Fluorescent probes play a key role in bioimaging to label the target and amplify fluorescent signal. The fluorophores can absorb light and jump to an excited state and then return to the ground state by emitting lower energy light. This energy difference between excitation and emission is called the Stokes shift.[17] The common fluorescent probes

include organic dyes, quantum dots, and rare-earth dopants. As microscopes have become more advanced, traditional organic fluorophores such as green fluorescent protein (GFP) show disadvantages in their photobleaching, poor stability, and short lifetime.[18] Quantum dots (QDs) are fluorescent semiconductor nanoparticles with spherical shape and < 10 nm in diameter.[19] The emission spectra of QDs can be tuned by changing their size.[20] And their advantage over organic fluorophores is that single excitation wavelength can be used to excite QDs with various colors. But they have shortcomings in toxicity, photo-blinking, susceptible to photooxidation and short circulation half times, which limit their biological applications.[21] Recently, lanthanide doped downconversion (DC) and upconversion (UC) particles have drawn great attention due to their photostability, high contrast and low toxicity.[22, 23]

Materials which can emit fluorescence when excited by UV or blue light are called downconversion (DC) materials.[24] DC is a non-linear optical phenomenon in which a high energy photon is absorbed followed by emitting two low energy photons. In addition to downconversion nanoparticles requiring an ultraviolet or blue excitation, the upconversion nanoparticles (UCNPs) with excitation of near-infrared laser show deep penetration in tissues (Figure 1-2A), multiplexing ability, and avoidance of tissue auto-fluorescence and possible fatal photodamage to cells.[25-28] Cells and tissues may have many fluorescent components of their own, resulting in unwanted background fluorescence known as auto-fluorescence when excited by UV or blue light. The upconversion process was first proposed in 1959,[29] which involves anti-Stokes shifts by upconverting low energy photons into high energy photons. When excited by a 980 nm NIR laser, the sensitizers (Yb^{3+} ions) can transfer energy to the nearby activators (Ho^{3+}, Er^{3+}, and Tm^{3+} ions) to emit short-wavelength luminescence (Figure 1-2B).[30] UCNPs have also advantages as photostable, sharp visible emission bandwidth,[23, 31] and are better for *in vivo* tracking studies over downconversion materials. The UCNPs can be ideal

fluorescent probes for a variety of biological applications, e.g. detection,[32, 33] imaging,[34, 35] cell tracking,[36] and therapy.[37] Most UCNPs have multi-photon (bicolor) emissions which paves the way to increase microscopy resolution.[38] The quantum yields (QYs) of UCNPs are very low, which hardly exceed 1% in water, and bulk materials or dried particles have higher QYs. The poor QYs are still acceptable for UNCPs due to a black background and avoidance of auto-luminescence.[39] Popular host matrixes that can house rare-earth ions to trigger upconverting fluorescence comprise $NaYF_4$,[34] $NaGdF_4$,[40] and $LaPO_4$,[41] whereas their composition is not similar to biological apatite, which may block further *in vivo* biomedical applications. The limitations and merits of various fluorescent probes are summarized in Table 1-1.

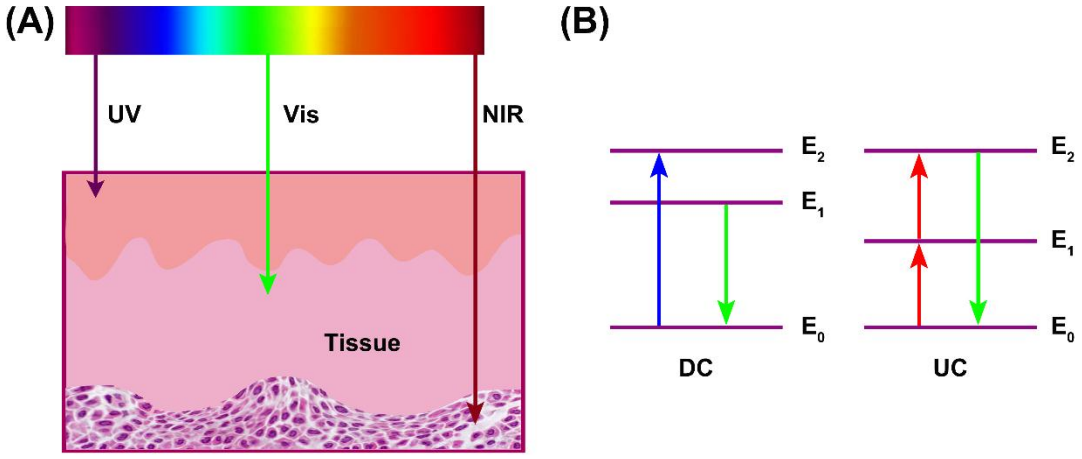

Figure 1-2 (A) Schematic representation of tissue penetration depth of various wavelength of light from UV to NIR. (B) Downconversion (DC) and upconversion (UC) energy transfer models.

Table 1-1 Limitations and merits of various fluorescent probes.

Organic fluorophores	Quantum dots	Rare-earth doping particles	
		Downconversion by UV	Upconversion by NIR
easy to use, photobleaching, poor stability, short lifetime	high brightness, high contrast, potential toxicity, photoblinking, short circulation half-time	high brightness, high contrast, photo-stability, low or no toxicity, conflict with tissue auto-fluorescence, photodamage to cells	high brightness, high contrast, photo-stability, low or no toxicity, deep penetration in tissues, avoidance of tissue auto-fluorescence and photodamage to cells

Selecting right doping matrix and dopants

Apatite crystal structure as the doping matrix

It is highly desirable that the apatite can be replaced by native tissue (bone or dentin); the implant dissolves gradually as the new tissue forms. Nanoparticles with unique size less than ~100 nm (at least one dimension) provide a wide range of biomedical applications such as cell imaging, as cells are much larger (average diameter ~ 10μm) in comparison.[19] Considering size effect, the nanoapatite are more soluble and osteogenic.[42] Despite their same composition to bulk materials, nanoparticles represent new properties, interactions with biological components, and distribution within the body. HA and FA have a similar crystal structure (hexagonal system, space group, $P6_{3/m}$) firstly solved in 1964.[43] Figure 1-3A shows that the unit cell of HA [$Ca_{10}(PO_4)_6(OH)_2$] consists of ten Ca^{2+} ions, six PO_4^{3-} groups, and two OH^- groups closely packed together with the lowest possible energy. The network of PO_4^{3-} groups provides the skeletal framework that gives the apatite structure its stability. The two OH^- groups locate in the corners of the unit cell along the *c*-axis at z =

0.25 and z = 0.75, respectively, and each OH^- is surrounded by three Ca^{2+} ions (called Ca^{2+} triangles) (Figure 1-3B). Successive calcium triangles are rotated through 60°. Comparing to HA, the substitution of higher electro-negative F^- for OH^- may alter the lattice parameters and cause FA a contraction in the *a*-axis dimension and no significant effect on the *c*-axis dimension.[44] And a lack of local polar moment associated with Ca and F in FA may contribute to its chemical stability over HA.[43, 45] In dentistry the fluoride treatment of enamel and dentin leads to the formation of partially F substituted apatite with more resistant to acid dissolution.[46] Fluoride therapy has been used to increase bone density for the management of osteoporosis.[47]

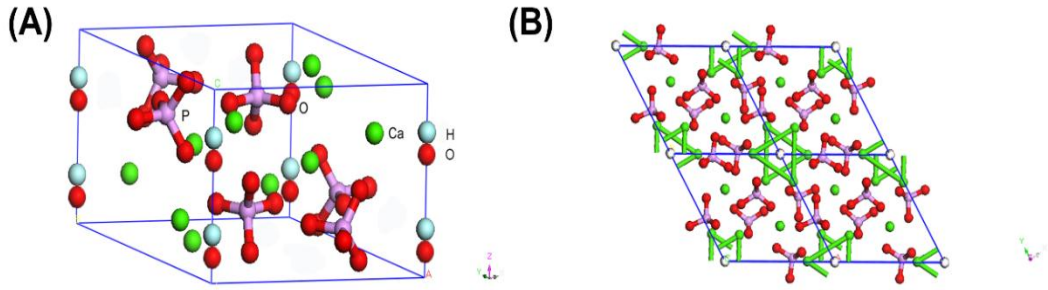

Figure 1-3 Schematic of the unit cell of HA (A), the two calcium triangles and OH channel in the center (B). Calculated simulation with Material Studio software.

Defects and impurities in apatite structure can be identified as either substitutional or extraneous crystalline phases, which can be detected by X-ray diffraction (XRD) and infrared spectroscopy (FT-IR). As shown in the XRD powder patterns (Figure 1-4),[1] bone has broader peaks than highly crystalline HA, while similar to the wet-synthesized apatite. The broadening of the peaks may be caused by the imperfections in the crystal lattice and the small crystal size. The Ca/P molar ratio distinct from the predicted 1.67 by chemical analysis has been confirmed the lack of stoichiometry of bone apatite.

Substitution of foreign ions and vacancies into the apatite crystal structure are common and affect lattice parameters (*a*- and *c*- axis dimensions), morphology, and thermal

stability.[48] The flexibility of the apatite structure allows a great variability of the composition as may be seen from that CO_3^{2-} can substitute for PO_4^{3-} or OH^-, F^- and Cl^- can substitute OH^-, and Ca^{2+} sites are easy to be substituted by many cations for various purposes. The substitution of Si^{4+},[49] Sr^{2+},[50] CO_3^{2-} [51] can increase osteogenesis. The $^{153}Sm/Gd^{3+}$ co-doping HA can serve as a dual-modality probe for SPECT and MR imaging *in vivo*.[52]

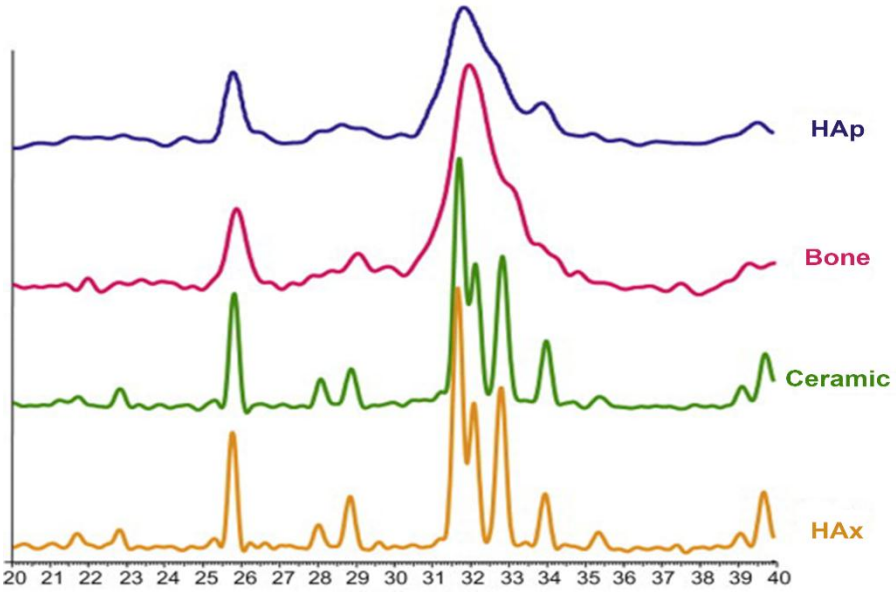

Figure 1-4 X-ray diffraction powder patterns for (top to bottom) - poorly crystalline HA (HAp), bovine cortical bone (Bone), HA ceramic, and highly crystalline HA (HAx). Adapted with permission from Hench.[1] Copyright (2013) Elsevier.

Synthesis

A wide variety of methods have been investigated to produce apatite, including solid-state reactions, hydrolysis and subsequent sintering at high temperatures, among which aqueous precipitation is the most popular route since 1960s.[1] Aqueous precipitation is mainly based on two synthetical routes: a reaction between a calcium salt (e.g., $Ca(NO_3)_2$) and an alkaline phosphate (e.g., Na_3PO_4),[53, 54] or a reaction between calcium hydroxide

and phosphoric acid.[55] Uniform apatite crystals can be prepared using hydrothermal methods.[56] In order to overcome uncontrolled agglomerates of nanoparticles caused by the high surface area, additives are involved to interact with the apatite surface, including polyacrylic acid (PAA), EDTA, sodium dodecyl sulfate (SDS), gelatin, collagen, and various organic acids.[57, 58] Beside size, apatite can be prepared with various shapes, such as spheres,[59] yolk–shell,[60] plates, rods, tubes.[61]

In recent years, some rare-earth doped materials are found to emit fluorescence when excited by ultraviolet (UV) or near-infrared (NIR) light.[62-64] The apatite crystal structure could be employed as a host matrix for lattice-substitution of rare-earth ions, to prepare both downconversion and upconversion fluorescent nanoparticles. The hexagonal structure of apatite crystals may be dominant in rare-earth doping and keeping thermal and fluorescent stability.[65, 66] The doping of Ln has a destabilizing effect, which increase with dopant concentration.[67] The trivalent lanthanide ions are sensitive to the chemical environments involved.[18] The lanthanide fluorescence has advantage over organic luminophores subject to photobleaching,[68] or semiconductor quantum dots (QDs) with potential toxicity of Cd/Se and short circulation half-time.[69]

Lanthanide ions as the fluorescent dopants for apatite

Lanthanide is any of a series of chemically similar metallic elements with atomic numbers ranging from 57 (lanthanum) through 71 (lutetium). The lanthanides, together with yttrium and scandium, constitute the rare-earth elements (Figure 1-5). The emission spectra range from UV, visible and near-infrared (NIR) regions (Figure 1-2A). The optical properties of Ln^{3+} ions are attributed to their electronic energy levels, generated by the electronic configurations $[Xe]4f^n$ (n = 0-14). The 4f-4f transitions are relevant for bioapplications.[18]

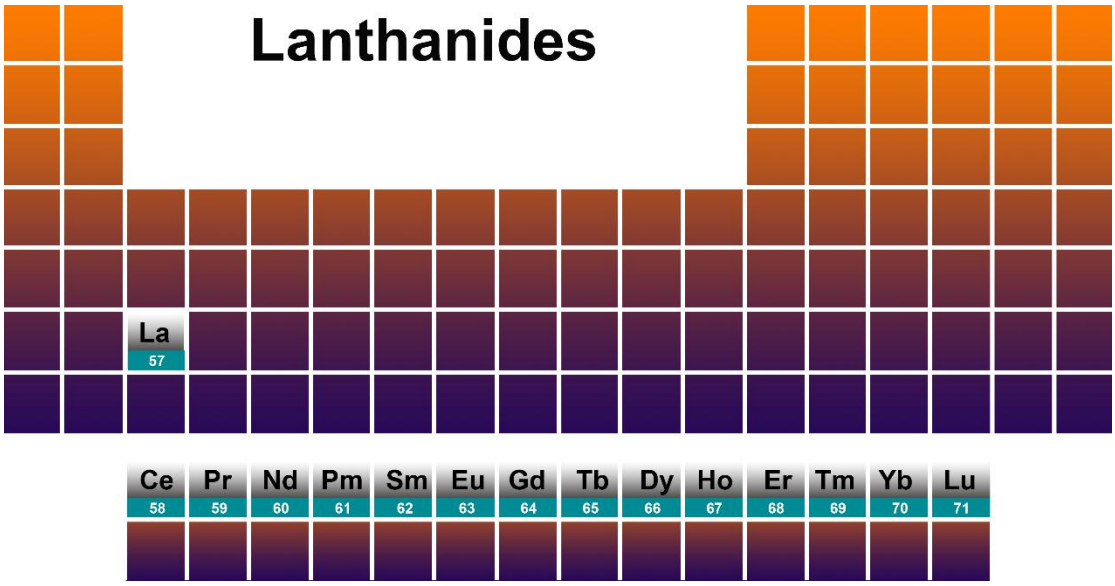

Figure 1-5 Periodic table showing the distribution of lanthanide elements.

Herein we selected apatite matrix that can not only house lanthanide ions but also possess good biocompatibility, and facilitate tissue-material interactions. The lanthanide ions have analogical radius as Ca^{2+} ions and high affinity to PO_4^{3-} ions,[65, 70] which can ensure the success of rare-earth doping.

Though a few kinds of UCNPs have appeared these years,[35, 71, 72] there are few reports on upconversion luminescence based on FA or HA matrix. Combination of the upconversion fluorescent property of Yb/Ho ions, the excellent bone-bonding capacity and typical crystal structure of apatite will afford us to design a promising upconversion biomaterial for biomedical applications. Moreover, near infrared (NIR) light can penetrate deeper in the body and shows less damage to cells than UV and blue light (Figure 1-2A). Upconversion particles as biomarkers are attractive for use in design of new probes and bioimaging applications. Work has been performed on multicolor tuning of upconversion probes and minimizing heating effect of excitation.[35, 73] Additional studies have shown applications in long-term real-time cell imaging[68] and in small-animal imaging.[74] However, there have so far been no reports on the potential of upconversion materials in labelling the implanted scaffold materials and the material-tissue interface.

Research objective

The goal of this thesis is to create new biocompatible fluorescent nano-apatites which can not only form bonding with bone tissue, but also provide stable and clear fluorescence imaging. The novel fluorescence probes are expected to overcome the shortcomings such as instability and photobleaching of organic fluorophores, and the potential toxicity from QDs. Several lanthanides doped apatite nanocrystals are designed for downconversion and upconversion luminescence, and prepared by hydrothermal synthesis Their crystal structure, luminescence properties, cell proliferation and fluorescent imaging are investigated to validate the following unsolved scientific problems:

1) Although the fluorescent properties of some rare-earth doped downconversion materials have been studied, the effects of the lanthanide ions on crystal structure, lattice occupation, cell proliferation and bioimaging are not investigated in detail, and not compared between HA and FA nanocrystals.
2) Despite a few kinds of upconversion particles have appeared these years, there are few reports on upconversion luminescence based on the FA or HA matrix. Combination of the upconversion fluorescent property of Yb/Ho ions with the excellent bone-bonding capacity of apatite will afford us to design a promising upconversion material for biomedical applications.
3) At present, the upconversion particles as biomarkers have exhibited steady developments in design of new probes and application of cell imaging, however, there is no report so far on exploring the potential of upconversion materials in labeling or tracking the implanted material, material-tissue interface and their respective distribution.

Therefore, we started to investigate in detail the effects of lanthanide ions on apatite crystal structure, lattice occupation, luminescence properties, cell proliferation and bioimaging between HA and FA nanocrystals. The lanthanide doped downconversion apatite nanocrystals with stable fluorescence could be fit for long-term cell imaging, and the upconversion nanoapatite might be an ideal option for clearly distinguishing the implanted material from bone tissue and showing their respective distribution. It is also useful for long-term *in vivo* tracking of implanted material or scaffold and their degraded fragments.

In the experiments, lanthanide Tb^{3+}, Eu^{3+} or Yb^{3+}/Ho^{3+} doped fluorapatite (FA:Tb^{3+}, FA:Eu^{3+}, FA:Yb^{3+}/Ho^{3+}) and hydroxyapatite (HA:Tb^{3+}, HA:Eu^{3+}, HA:Yb^{3+}/Ho^{3+}) nanoparticles with varying dopant concentration were prepared by hydrothermal synthesis. Their physico-chemical properties were characterized by XRD, FT-IR, SEM, TEM, EDS and ICP-OES, the upconversion emissions were detected by fluorescence spectrometry. Cell proliferation was evaluated via MTT assay, and animal experiments were performed by using femoral bone defect model of rabbits. The cells penetrated by the lanthanide doped nanoparticles, and the histological sections of the harvested *in vivo* samples treated by Masson's staining, were imaged by fluorescence microscopy and confocal microscopy.

CHAPTER 2 COMPARATIVE INVESTIGATION ON CRYSTAL STRUCTURE AND CELL BEHAVIOR OF RARE-EARTH DOPED DOWNCONVERSION FLUORESCENT APATITE NANOCRYSTALS

Introduction

The mineral phase of human calcified tissues is mainly composed of nano apatite crystals.[2] Synthetic apatite, including hydroxyapatite ($Ca_{10}(PO_4)_6(OH)_2$, HA) and fluorapatite ($Ca_{10}(PO_4)_6F_2$, FA), has a similar hexagonal structure to biological apatite. The flexibility of the apatite structure allows a great variability of the composition as may be seen from that the Ca^{2+} sites are easy to be substituted by many other ions, such as Mg^{2+}, Sr^{2+}, Na^{+} or Al^{3+} etc.[75-77] Due to the similarity of composition or structure, both HA and FA possess good biocompatibility and have been widely used as defect fillers of bones and teeth.[3, 4] In recent years, some rare-earth doped materials are found to emit fluorescence when excited by UV or blue light.[62, 63] The hexagonal structure of apatite crystals may be dominant in rare-earth doping and keeping thermal and fluorescent stability.[65, 66]

The trivalent lanthanide ions are sensitive to the chemical environments involved.[18] The lanthanide fluorescence has advantage over organic luminophores subject to photobleaching,[68] or semiconductor quantum dots with potential toxicity of Cd/Se and short circulation half-time.[69] Terbium (Tb) doped materials have been reported to generate green fluorescence.[78, 79] Although the preparation method and fluorescent properties of these Tb-doped materials were studied broadly, the effects of Tb^{3+} ions on crystal structure, lattice occupation and cell proliferation are not investigated in detail, and not compared between HA and FA nanocrystals. In order to reasonably express the incorporation mechanism of Tb^{3+} ions into the apatite lattice and explore the effect of Tb^{3+} doping on

crystal structure and cell proliferation, a doping molar ratio, 1.7/8.3, of terbium relative to calcium in a unit cell was chosen in this experiment.

Materials and methods

Materials

$Ca(NO_3)_2 \cdot 4H_2O$, $Tb(NO_3)_3 \cdot 6H_2O$, $Eu(NO_3)_3 \cdot 6H_2O$, $Na_3PO_4 \cdot 12H_2O$, NaF, octadecylamine, oleic acid, ethanol, and cyclohexane in AR grade were obtained from Beijing Chemical Reagents Company, China. Dextran 20,000 in AR grade was purchased from Sinopharm Chemical Reagent Company, China. Other chemical agents obtained from commercial routes were of analytical grade and used without further purification.

Preparation of apatite nanocrystals doped with Tb^{3+}

Octadecylamine (0.5 g) was dissolved in oleic acid (4 mL) and ethanol (16 mL) under magnetic stirring in a Teflon-lined autoclave (50 mL). Then aqueous solution of $Ca(NO_3)_2$ (0.28 M, 7 mL), $Tb(NO_3)_3$ (0.05-0.20M, 2 mL), and Na_3PO_4 (0.20 M, 7 mL) was added. For FA:Tb^{3+}, additional NaF (0.24 M, 2 mL) was added. Afterwards, the mixture was agitated for 10 min, and hydrothermally treated at 160 °C for 16 h. After cooling to room temperature naturally, the white precipitate collected by centrifugation (10 min at 2700 × g) was fully washed and freezing-dried.

Preparation of apatite nanocrystals doped with Eu^{3+}

Octadecylamine (0.5 g) was dissolved in oleic acid (4 mL) and ethanol (16 mL) under magnetic stirring in a Teflon-lined autoclave (50 mL). Then aqueous solution of $Ca(NO_3)_2$ (0.28 M, 7 mL), $Eu(NO_3)_3$ (0.05-0.20M, 2 mL), and Na_3PO_4 (0.20 M, 7 mL) was added. For FA:Eu^{3+}, additional NaF (0.24 M, 2 mL) was added. Afterwards, the mixture was

agitated for 10 min, and hydrothermally treated at 160 °C for 16 h. After cooling to room temperature naturally, the white precipitate collected by centrifugation (10 min at 2700 × g) was fully washed and freezing-dried.

Characterization

X-ray diffraction (XRD) powder patterns were acquired with a Philips X' Pert Pro MPD equipment in the 2θ range from 20° to 60° with Cu Kα radiation (λ = 1.5406 Å). Transmission Electron Microscope (TEM) images of the nanocrystals were collected on an FEI TecnaiG2 T20 instrument at 200KV. The binding energy data were measured by XPS spectrum, AXIS Ultra DLD, Kratos, UK. The Tb/Ca molar ratio was tested by ICP-OES, Teledyne Leeman, USA. The photoluminescence was recorded by the Hitachi F-7000 fluorescence spectrophotometer.

Cytotoxicity assay

BMSCs were seeded in a 96-well flat-bottomed microplate at a density of 20, 000 cells per well, and cultured in 5% CO_2 at 37 °C for 48 h. Then FA:Tb^{3+}, FA:Eu^{3+}, HA:Tb^{3+}, and HA:Eu^{3+} nanocrystals with a concentration of 100 μg mL^{-1} were added to the medium. After incubation for 1, 4, 7, and 11 days at 37 °C, these nanocrystals were removed by washing with PBS for three times. 20 μL 3-[4,5-dimethylthiazol-2yl]-2,5- diphenyl-2H-tetrazoliumbromide (MTT) solution (0.8 mg mL^{-1}) was added into each well, and cells were incubated further for 4 h at 37 °C. Subsequently, the media was discarded, and the precipitated formazan was dissolved in dimethyl sulfoxide (DMSO, 150 μL per well), and optical density of the solution was recorded using a microplate reader (PerkinElmer wallac 1420) at a wavelength of 570 nm. Results are presented as mean ± SD from triplicate wells. A value of $p < 0.05$ was considered to be statistically significant.

Coating of dextran on FA:Tb^{3+} nanocrystals

The prepared FA:Tb^{3+} nanocrystals (50mg) were firstly dispersed in cyclohexane (5 mL) and mixed with dextran solution (100 mg, 10 mL) in a 50 mL round-bottom flask. Then 10 mL tetrahydrofuran (THF) was added to form a turbid suspension. The mixture was dispersed by ultrasonication, and then stirred for 2 h at room temperature to obtain a homogeneous phase. Finally, they were isolated by centrifugation (3 min at 6000 rpm) and purified with distilled water and ethanol for three times. The product could be redispersed in aqueous solutions.

Cell Imaging

The BMSCs were seeded onto 35 mm coverglass-bottom dishes and incubated in 2 mL of DMEM at 37 °C for 24h. The culture medium was removed and these cells were incubated in 2 mL DMEM containing the dextran-grafted FA:Ln^{3+} nanocrystals (100 μg mL^{-1}) at 37 °C for 24 h. After rinsing with PBS three times, cells were fixed with 4% paraformaldehyde for 15 min. The fluorescence imaging was conducted under a confocal microscope (Leica LSM780). The green emission was collected at 488 nm.

Statistical analysis

The results were expressed as mean ± standard deviation (SD). Statistical comparisons between groups were analyzed by using one-way ANOVA test. A value of $p < 0.05$ was considered to be statistically significant.

Results and discussion

In order to evaluating the efficiency of the doping system, we started the preliminary investigation to screen the rare-earth elements and validate our hypothesis, that is, apatite

can be used as matrix for rare-earth doping downconversion (DC) luminescence. The hexagonal apatite crystal structure is selected as the doping matrix, including hydroxyapatite ($Ca_{10}(PO_4)_6(OH)_2$, HA), fluorapatite ($Ca_{10}(PO_4)_6F_2$, FA). Various rare-earth elements were tried according to literature and our research needs, we found four lanthanides worked for downconversion (DC) apatite system. As shown in Table 2-1, the emissions for Sm (samarium), Eu (europium), Tb (terbium), Dy (dysprosium) showed orange, red, green, and blue respectively. The luminescence color depends on their unique electron orbitals. Because human eyes are sensitive to red and green colors, we select Eu and Tb for DC dopants. The morphologies of some lanthanides co-doped FA crystals are shown in Figure 2-1, including nanospheres, nanorods, and nanowires. In most cases, apatite NPs show rod-like morphology and have been commonly used for biological applications.

Table 2-1 Screening of the doping lanthanides for DC apatite system.

	Sm^{3+}	Eu^{3+}	Tb^{3+}	Dy^{3+}
DC	Orange	Red	Green	Blue

The crystal structure and morphology of the rare-earth doped apatite were examined using XRD and TEM. In Figure 2-2, the XRD patterns of both Ln^{3+} doped fluorapatite and hydroxyapatite crystals matched well with the classical hexagonal phase of apatite, FA ($Ca_{10}(PO_4)_6F_2$, ICDD 15-0876) or HA ($Ca_{10}(PO_4)_6OH_2$, ICDD 09-0432), respectively. The sharp characteristic peaks around 26°, 32°, 32.3°, 40°, 47°, 50°, and 53° corresponded to (002), (211), (112), (310), (222), (213), and (004) lattice planes, respectively. The Ln^{3+} ions were supposed to be incorporated into the apatite crystal lattice, and there were no impurity

diffraction peaks or phases in the XRD pattern. The measured lattice parameters a = b = 0.939 nm, c = 0.688 nm for FA:Tb^{3+}, and a = b = 0.944 nm, c = 0.688 nm for HA:Tb^{3+} were in good agreement with the data of FA (a = b = 0.937 nm, c = 0.688 nm) and HA (a = b = 0.942 nm, c = 0.688 nm), besides the tiny increase of the *a*-axis. The *a*-axis dimension of FA:Tb^{3+} was smaller than that of HA:Tb^{3+} without change of the *c*-axis. The hexagonal crystal structure of apatite has good stability, which would be helpful for stable fluorescence expression of the embedded rare-earth ions.

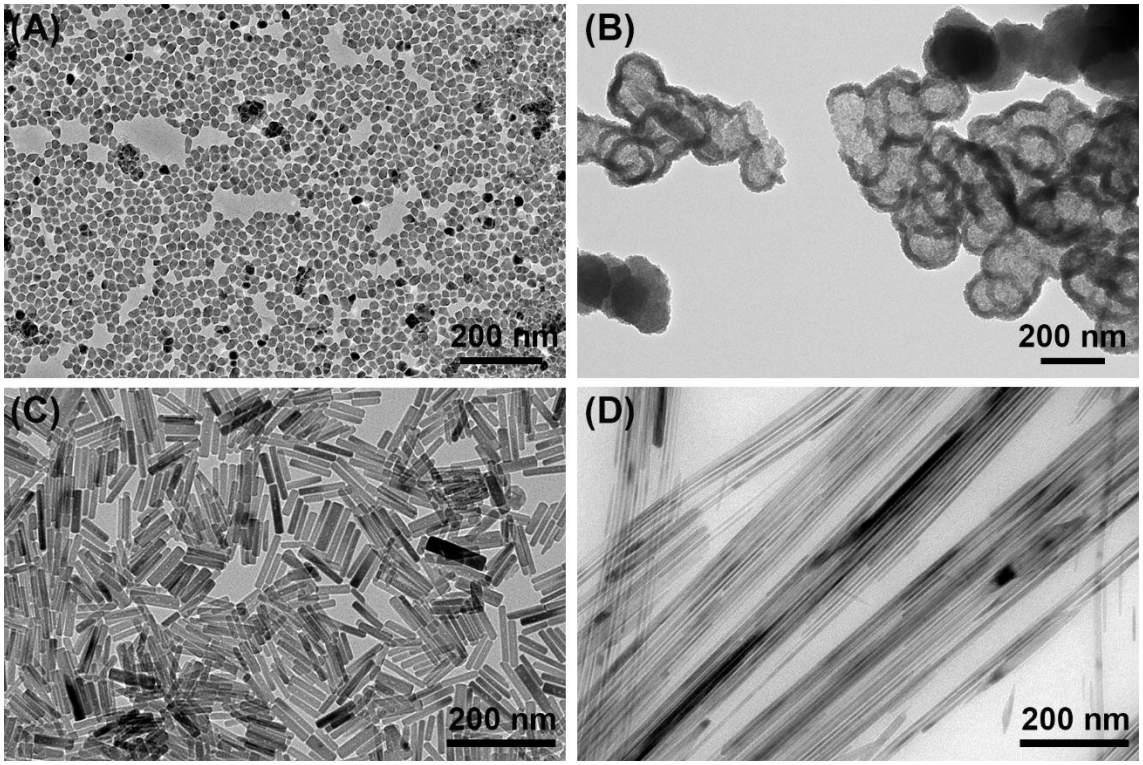

Figure 2-1 The common morphologies of nanoapatite: (A) nanospheres, (B) hollow nanospheres, (C) nanorods, (D) nanowires.

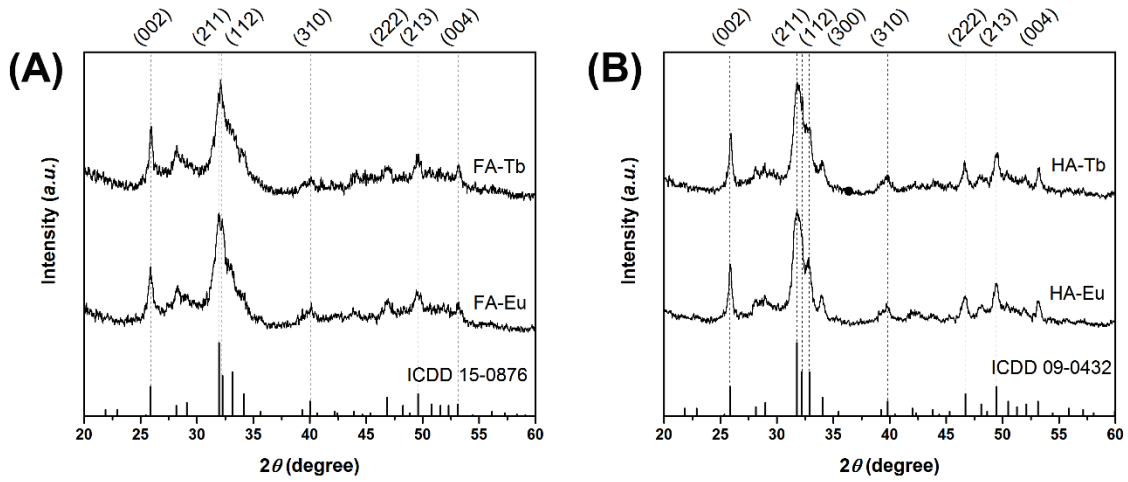

Figure 2-2 XRD patterns of Tb^{3+} or Eu^{3+} doped FA (A) and HA (B) nanocrystals.

It could be seen from the TEM results in Figure 2-3 that both Tb^{3+} doped FA and HA crystals were in nanoscale and showed a uniform rod-like morphology (A, B). The average dimensions of Tb^{3+} doped FA and HA crystals were about 15×140 nm and 12×180 nm, respectively. The crystal sizes were larger than that of FA (13×75 nm) and HA (9×80 nm) before doping. The HRTEM images (C, D) gave the interplanar spacing of (002) lattice plane for FA:Tb^{3+} (0.345 nm) and HA:Tb^{3+} (0.347 nm), which was in accord with the XRD patterns in Figure 2-2. The EDS element mapping (E, F) demonstrated the successful incorporation of Tb^{3+} ions in the apatite crystal structure. The results indicate that the doping of Tb^{3+} ions can promote preferential growth of FA and HA crystals along the *c*-axis (002) direction, and the doped nanocrystals have a typical single crystal structure with uniform morphology. Eu^{3+} doped apatite nanocrystals were in same situation.

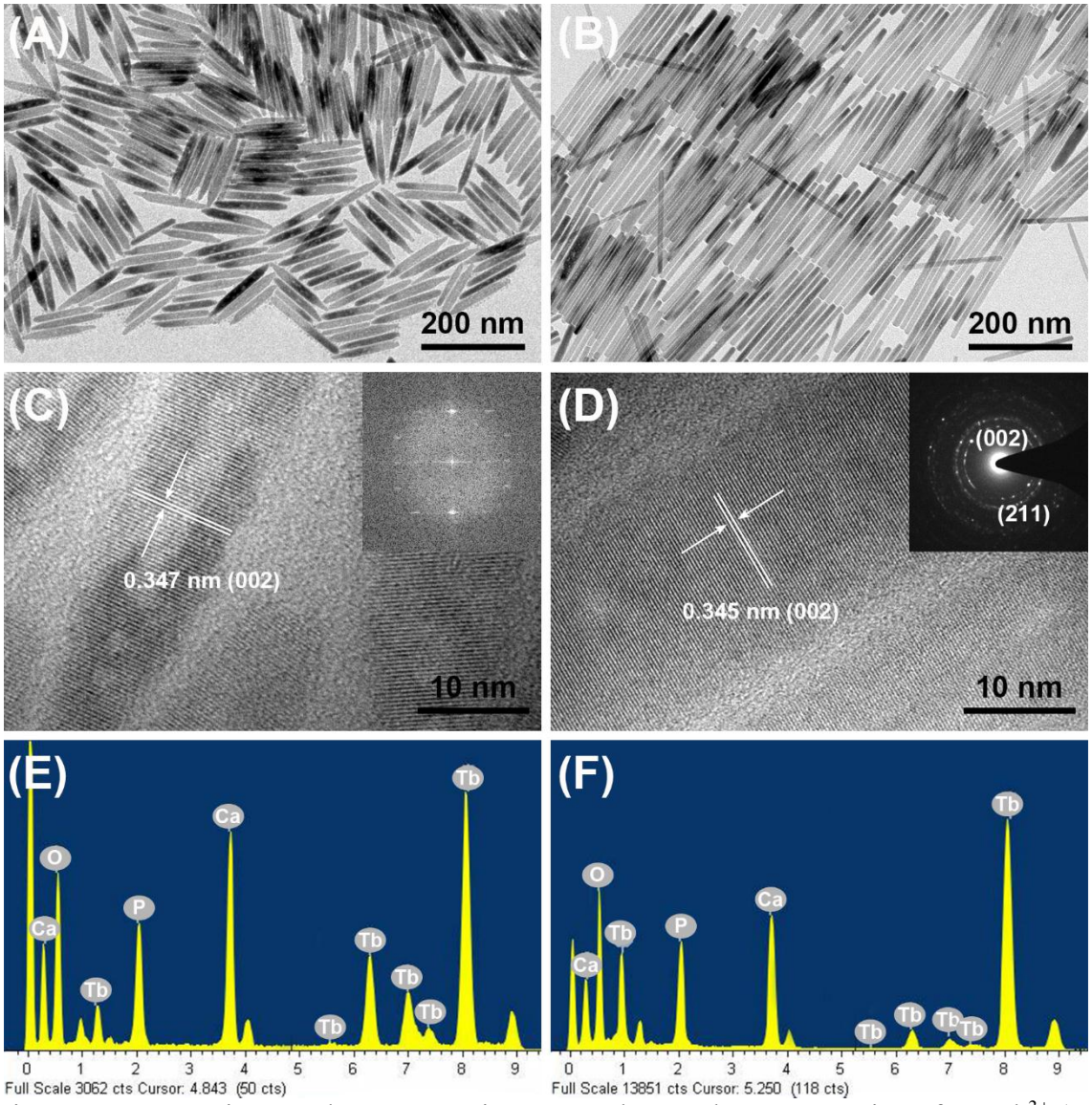

Figure 2-3 TEM micrographs, HRTEM images, and EDS element mapping of FA:Tb^{3+} (A, C, E) and HA:Tb^{3+} (B, D, F) nanocrystals. The inset in C is the FFT pattern of FA:Tb^{3+}, and the inset in D is the SAED pattern of HA:Tb^{3+}.

The XPS spectra in Figure 2-4 showed that the peaks of Tb and Eu could be clearly observed in both apatite crystals, indicating the successful incorporation of Tb^{3+} and Eu^{3+} ions into the crystal lattice of FA and HA. The binding energy data of different ions for Tb^{3+} and Eu^{3+} doped apatite were listed in Table 2-2. After doping of Tb^{3+} or Eu^{3+} ions in FA and HA matrix, the binding energy of Ca, P and O showed slightly increase for FA:Ln^{3+} and slightly decrease for HA:Ln^{3+}. This indicates that the Ln^{3+} ions can really enhance the

ion interaction in FA structure, and weaken the ion interaction in HA structure.

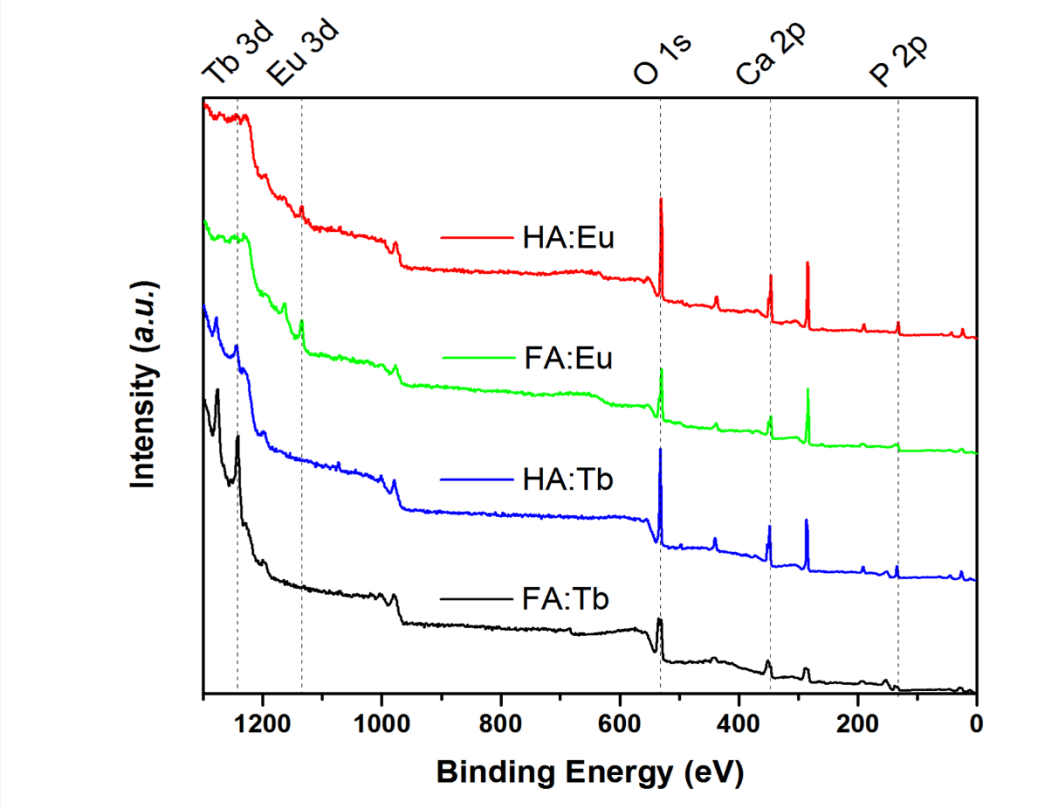

Figure 2-4 XPS spectra of Tb^{3+} or Eu^{3+} doped apatite nanocrystals.

Table 2-2 Binding energy of Ca, P, and O in Tb^{3+} or Eu^{3+} doped apatite nanocrystals.

	FA (eV)	FA:Tb^{3+} (eV)	FA:Eu^{3+} (eV)	HA (eV)	HA:Tb^{3+} (eV)	HA:Eu^{3+} (eV)
Ca (2p)	346.8	347.1	347.1	347.0	346.8	347.1
P (2p)	132.8	133.0	132.8	133.0	132.9	132.9
O (1s)	530.7	530.8	530.9	531.0	530.8	531.1

The emission spectra in Figure 2-5 showed luminescent peaks of apatite doped with various concentrations of Ln^{3+} ions. For Tb^{3+} doped apatite (A, B), when excited at 265 nm, there were two strong green peaks at about 490 and 545 nm, which could be respectively ascribed to $^5D_4$-$^7F_6$ and $^5D_4$-$^7F_5$ transitions of Tb energy levels. In FA and HA

matrixes, the emission intensity of 10% and 20% samples were similar, and much higher than the 5% sample in FA matrix. For Eu^{3+} doped apatite, while excited at 395 nm, they emit red emission (C, D) with peaks at 600 ($^5D_0$-$^7F_1$) and 623 nm ($^5D_0$-$^7F_2$). And higher peak intensity was observed with 10% and 20% Eu^{3+} concentration in FA matrix. In HA matrix, the strongest intensity was for the 20% Eu^{3+} concentration. Figure 2-5E, F illustrated that FA:Ln^{3+} crystals had stronger fluorescence than that of HA:Ln^{3+} crystals. It may result from the more compact crystal structure of FA:Ln^{3+} crystals caused by F^- ions and the increase of binding energy mentioned in Table 2-2. In addition, the F^- ions have a low phonon energy which can reduce the quenching of the excited state of the rare-earth ions.[80, 81] The bright green and red emission can repeatedly sustain for a long time, implying a stable coordination between apatite crystal structure and Ln^{3+} ions. FA:20%Ln^{3+} crystals were used for further *in vitro* studies.

Theoretically, the rare-earth doped FA:Ln^{3+} and HA:Ln^{3+} nanocrystals were synthesized according to the molar ratio, setting at 5, 10, and 20%, respectively. The analytical data by ICP-OES in Table 2-3 illustrated that the measured molar ratios of Ln/Ca in both FA:Ln^{3+} and HA:Ln^{3+} crystals were lower than the theoretical value; while the measured molar ratios of Ln/Ca in HA:Ln^{3+} crystals were slightly higher than that in FA:Ln^{3+}. Such phenomenon should be mainly related to the difference of F^- ions from OH groups. Both FA and HA have similar hexagonal structures, but the F^- ions in FA structure occupy smaller space, resulting in a contracting crystal structure.

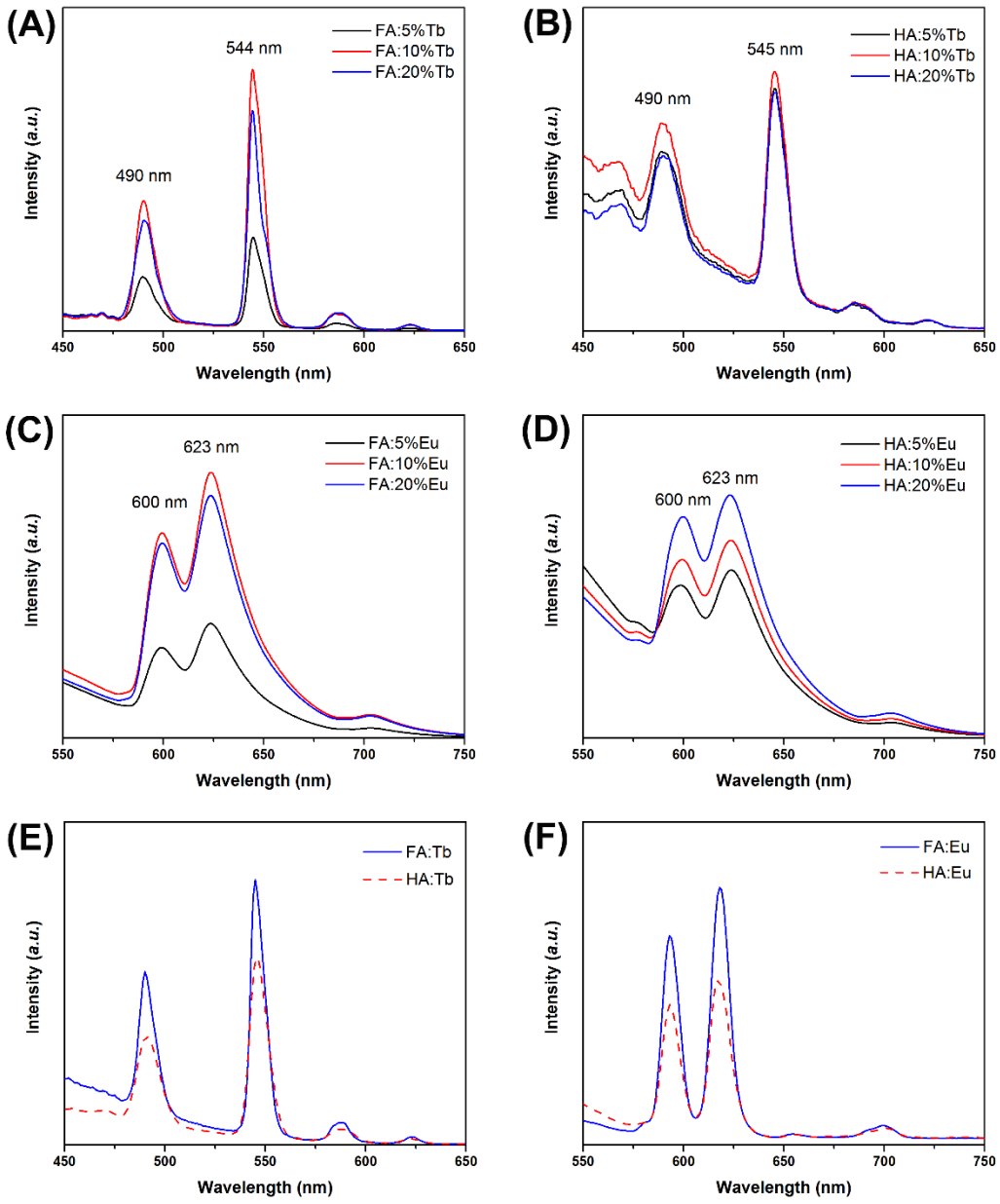

Figure 2-5 Emission spectra of apatite nanocrystals doped with various concentrations of Tb^{3+} (A, B) or Eu^{3+} ions (C, D), and comparation of Tb^{3+} (E) or Eu^{3+} (F) in different matrixes.

Table 2-3 Measured molar ratio of Ln^{3+}/Ca^{2+} in Tb^{3+} or Eu^{3+} doped apatite nanocrystals.

	5%	10%	20%
FA-Tb (%)	3.436 ± 0.013	7.639 ± 0.023	16.070 ± 0.062
HA-Tb (%)	3.732 ± 0.005	8.797 ± 0.059	20.728 ± 0.014
FA-Eu (%)	3.042 ± 0.009	6.624 ± 0.001	13.681 ± 0.093
HA-Eu (%)	3.012 ± 0.007	7.167 ± 0.037	14.821 ± 0.073

In order to explain the substitution mechanism of Ln^{3+} ions in apatite crystal structure, the HA:Tb^{3+} crystals are chosen as a presentative of the Ln-doped apatite. According to the XRD pattern (Figure 2-2) and measured lattice parameters, the structure is retained when Tb^{3+} ion is placed for Ca^{2+} ion. As the measured Tb/Ca molar ratio is 1.6/8.4, a formula of $(Ca_{8.4}Tb_{1.6})(PO_4)_6(OH)_2$ can be obtained. However, to maintain the charge valence, some Ca^{2+} vacancy or substitution of O^{2-} for –OH should be present. Thus, we propose four reasonable valence-balanced Tb-doped lattice models along the hydroxyl channel of HA hexagonal structure for HA:Tb^{3+} crystal (Figure 2-6). In Figure 2-6B, two Tb^{3+} ions replace two Ca^{2+} ions in a Ca triangle, leaving a vacancy (©) of Ca site, the molecular formula can be expressed as $(Ca_7Tb_2©)(PO_4)_6(OH)_2$; In Figure 2-6C, two Tb^{3+} ions and two Na^+ ions substitute for four Ca^{2+} ions in two Ca triangles, forming the formula of $(Ca_6Tb_2Na_2)(PO_4)_6(OH)_2$. In Figure 2-6D, one Tb^{3+} ion replaces one Ca^{2+} ion in a Ca triangle, and one O^{2-} ion replaces one –OH group, leading to a cation defect compound $(Ca_9Tb)(PO_4)_6(OH)O$. In Figure 2-6E, one Tb^{3+} ion and one Na^+ ion substitute for two Ca^{2+} ions in a Ca triangle, forming a formula of $(Ca_8TbNa)(PO_4)_6(OH)_2$. In fact, the molecular formula of the doped apatite is very complicated to precisely replicate, however, such

emulation is an effective and reasonable approach， because the total valence is balanced and the ionic radii of Tb^{3+} (92.3 pm) , Ca^{2+} (99 pm) and Na^{+}(98 pm) are similar. The Tb/Ca molar ratios in a unit cell are about 2.2/7.8 (B), 2.5/7.5 (C), 1/9 (D) and 1.1/8.9 (E), respectively. The measured Tb/Ca ratio in HA:Tb^{3+} is 1.6/8.4, that is to say, the substitution of Tb^{3+} ions for Ca^{2+} ions in apatite crystals has many coexistent situations, which can be identical or different in each unit cell.

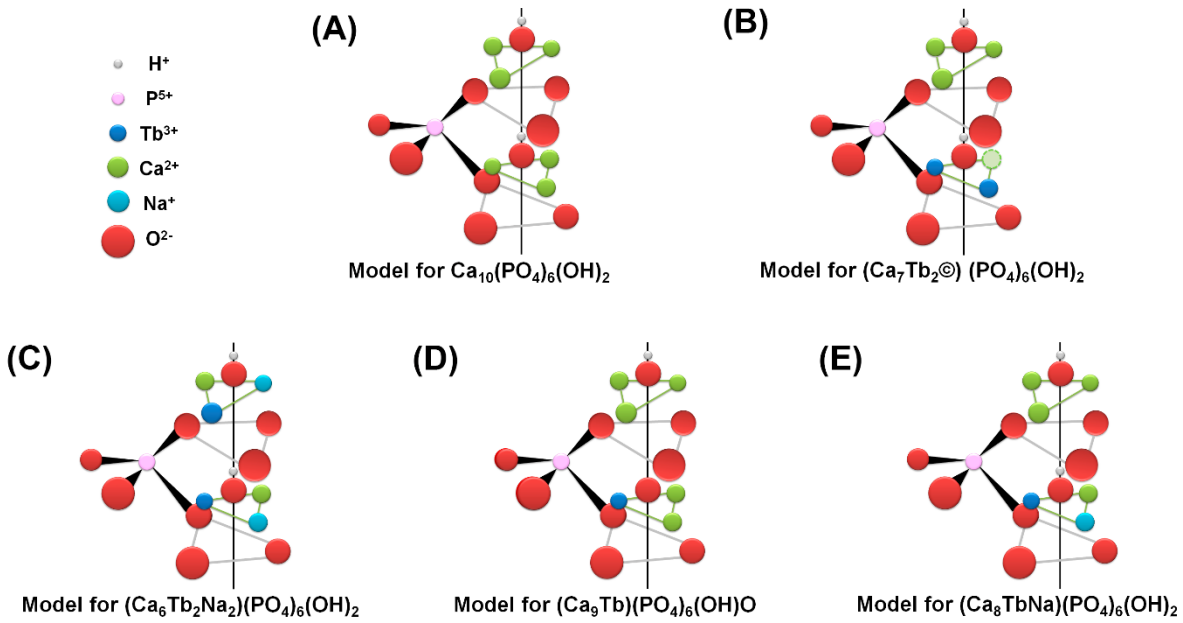

Figure 2-6 Schematic diagram of Tb-doping lattice models along the hydroxyl channel of the HA hexagonal structure.

To explore the potential of FA:Ln^{3+} crystals for future biomedical applications, we used hydrophilic dextran to graft the surface of these crystals for cell imaging (Figure 2-7A). Previous studies[82] showed that apatite nanocrystals entered BMSCs via endocytosis; the crystals were entrapped within endosomes and then released to cytoplasm.[83, 84] Dextran is a cationic polymer that binds to early endosomes.[85] When grafted by dextran, the hydrophobic crystals become hydrophilic, which facilitates dispersity in water and endocytosis process. Figure 2-7B showed the FT-IR spectra of the FA:Tb^{3+} crystals coated

with or without dextran. The absorption peaks at 3458 and 1666 cm^{-1} attributed to typical stretching vibration and bending vibration of the -OH groups, and the absorption peak at 2929 cm^{-1} is the typical stretching vibration of C-H in dextran. The result showed evidence of successful grafting of hydrophilic dextran on the crystals. The dextran-grafted FA:Tb^{3+} crystals are small in size and exhibit distinct fluorescence, good dispersity in water, good cytocompatibility, and crystal stability, making them suitable for bioimaging investigation. Figure 2-7C showed that the cell proliferation of different groups with a dosage of 100 μg mL^{-1} increased continuously with time, indicating a normal growth trend and good cytocompatibility. The cell proliferation of reported experiments was usually evaluated only for 24 hours,[86, 87] which could be not sufficient to support a statement of good cytocompatibility. In contrast, all the samples in this experiment were carried out for a period of 11 days, demonstrating a good cytocompatibility of the Ln-doped nanocrystals.

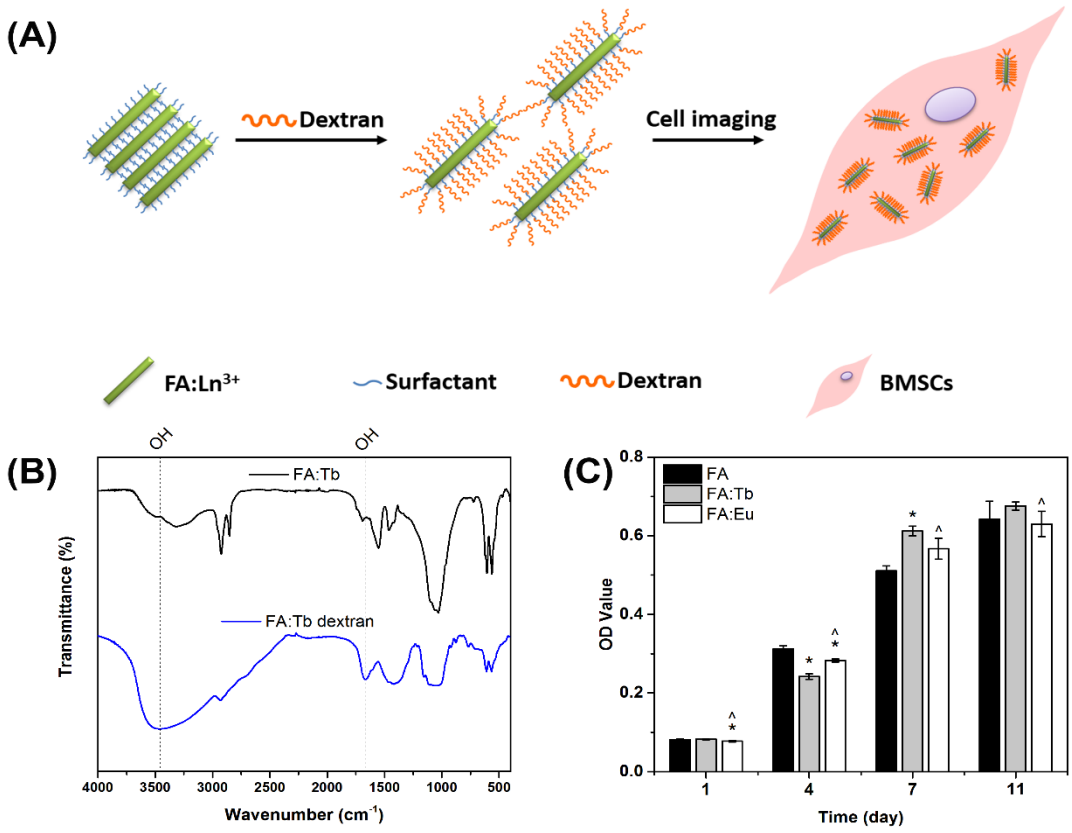

Figure 2-7 Schematic diagram showing dextran-coated fluorapatite nanorods doped with lanthanides in BMSCs (A). FT-IR spectra of dextran-coated FA:Tb^{3+} crystals (B). BMSCs proliferation after cultured with 100 μg mL^{-1} dosages of FA:Ln^{3+} nanocrystals for 1, 4, 7, 11 days (C), error bars represent mean ± SD from triplicate experiments, $p < 0.05$ (* vs. FA, ^ vs. FA:Tb).

The entering of the fluorescent FA:Tb^{3+} nanocrystals into the cytoplasm of cells (BMSCs) was demonstrated under a confocal microscope, as shown in Figure 2-8. The cells showed distinct and uniform green or red fluorescence, which was better than the HA nanoparticles surface modified with small amount of Tb^{3+}.[88] The cell morphology and cytoplasm could be clearly observed or distinguished. The fluorescent images (A, D, G, J) of cells matched well with the light image of the cells (B, E, H, K), which gave a clear overlap image (C, F, I, L). Moreover, the luminescence intensity of the FA:Ln^{3+} nanocrystals could maintain repeatable even after 7 days, indicating that there was no apparent photobleaching occurring in the cell imaging process. This provides feasibility

for imaging and tracking of cells with multilineage differentiation.

The mRNA levels of alkaline phosphatase (ALP), the alpha l chain of type I collagen (COL1α1), and osteonectin (ON) mRNA were analyzed via real-time PCR assay on days 14 and 21 of differentiation. Figure 2-9 showed the mRNA change of the relative gene expressions. According to the real-time PCR results of ALP, COL1α1 and ON, the increased expression of the mRNA from the FA group clearly demonstrates that fluorapatite nanorods doped with lanthanides (Tb^{3+} or Eu^{3+}) can influence the differentiation of BMSCs.

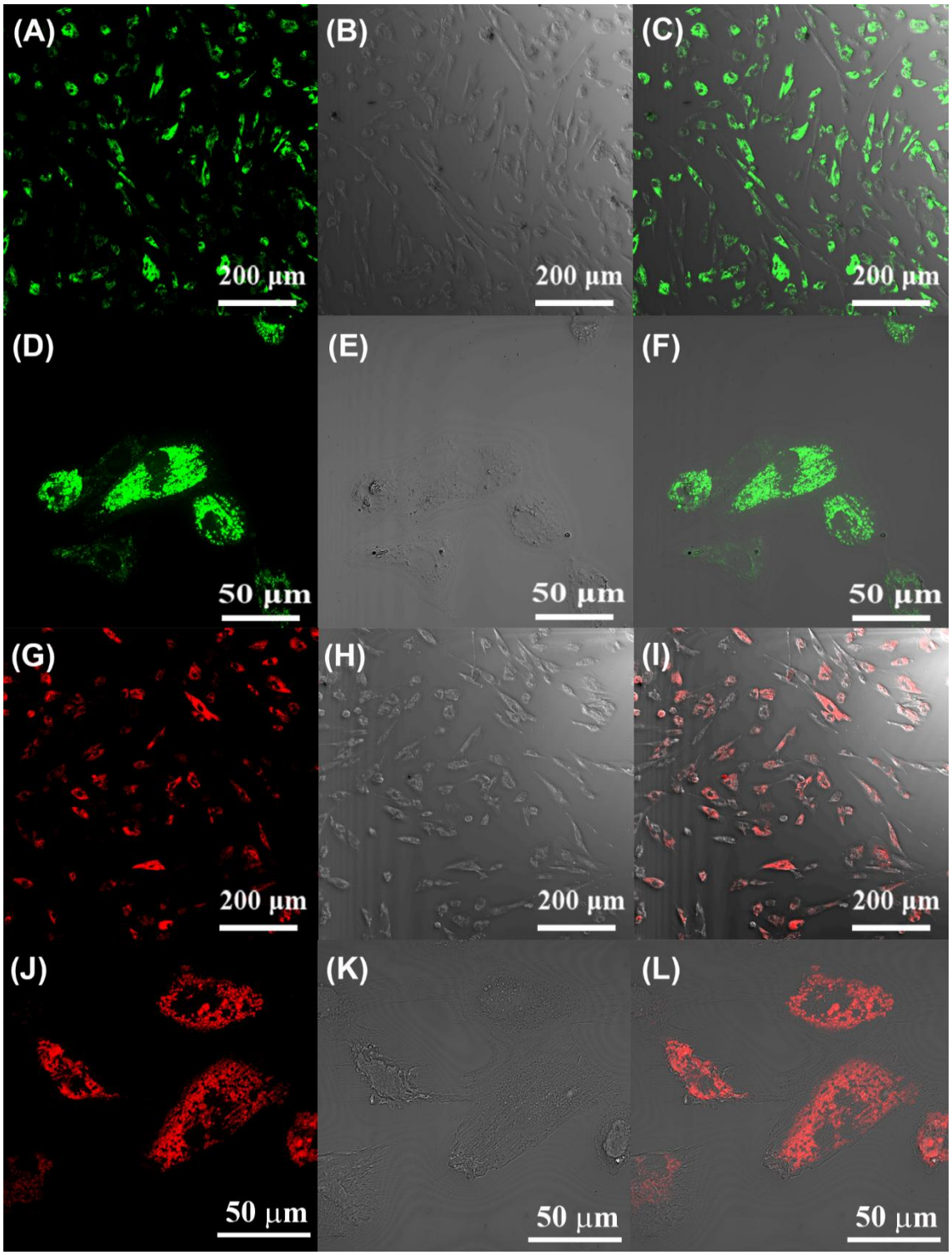

Figure 2-8 Confocal microscope luminescent images (A, D), light images (B, E) and overlap images (C, F) of BMSCs treated with 100 μg mL^{-1} FA:Tb^{3+} nanocrystals. Confocal microscope luminescent images (G, J), light images (H, K) and overlap images (I, L) of BMSCs treated with 100 μg mL^{-1} FA:Eu^{3+} nanocrystals.

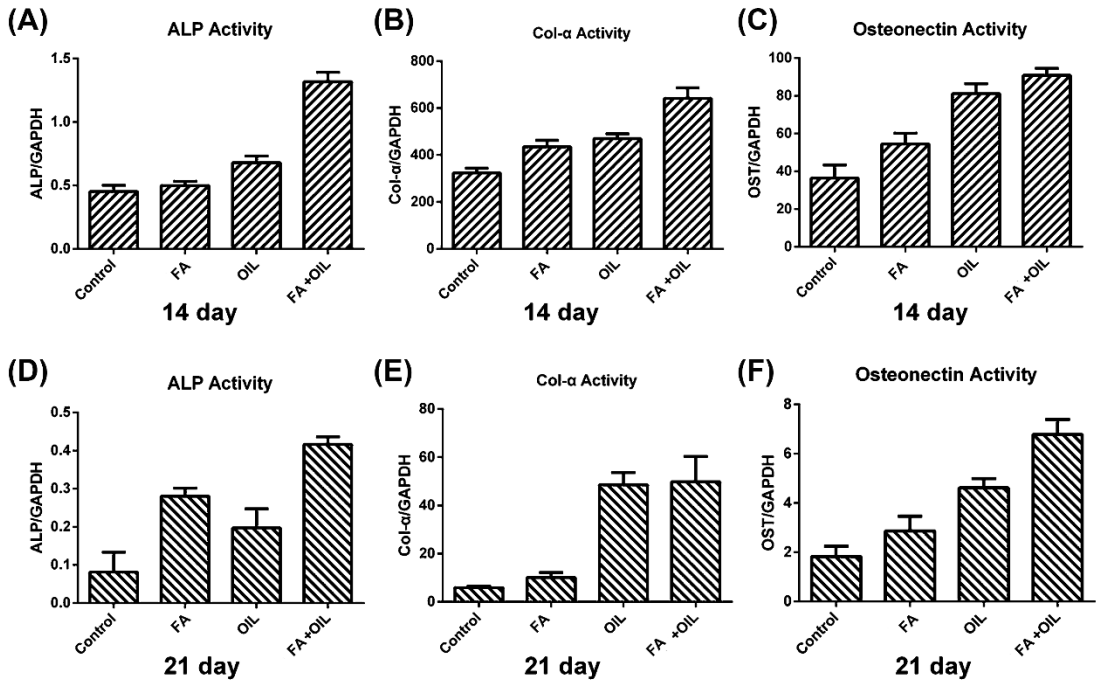

Figure 2-9 Effects of the Tb–FA nanorods on the osteoblast-related gene expressions of BMSCs. Image analysis of (A and D) ALP, (B and E) COL-α and (C and F) gene expressions. The control group was treated with regular complete medium, the FA group was treated with 100 mg mL^{-1} Tb–FA with complete medium, the oil group was treated with the osteogenesis induced liquid, and the FA + oil group was treated with both. Adapted with permission from Zeng.[82] Copyright (2014) The Royal Society of Chemistry.

Figure 2-10 showed the effect of the Tb–FA nanorods on the osteoblast-related protein expression of BMSCs. The ALP activity was detected via ALP spectrophotometry on days 14 (A) and 21 (B) of differentiation. The following ELISA test also confirmed that rare earth elements do not influence fluorapatite nanorods in promoting the osteogenic differentiation of BMSCs. There is a synergistic effect of osteogenic differentiation between biochemical regents and fluorapatite nanorods.

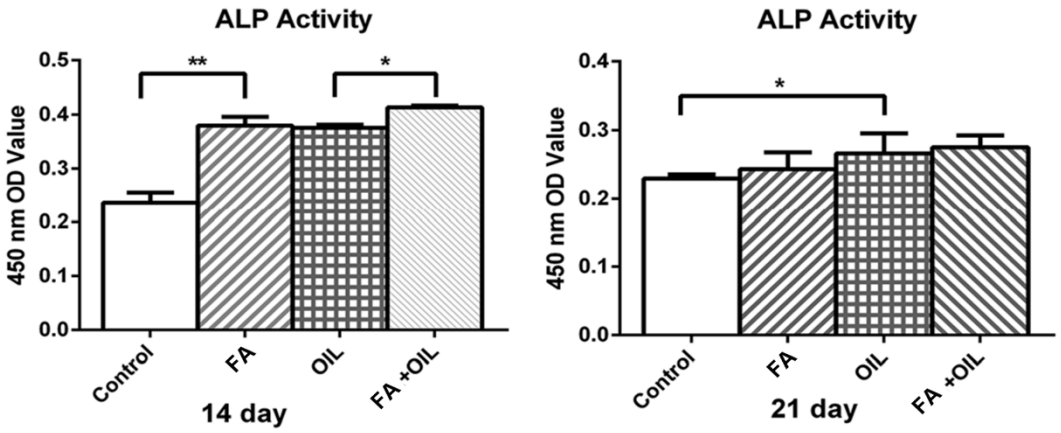

Figure 2-10 Osteoblast-related protein expressions of Tb–FA nanorods on BMSCs. * indicates $P < 0.05$ and ** indicates $P < 0.01$. Adapted with permission from Zeng.[82] Copyright (2014) The Royal Society of Chemistry.

Labelled BMSCs were seeded on the sterilized PCL scaffold that was subcutaneously implanted in nude mice. Samples were harvested one month (Figure 2-11A and B) and three months (C and D) later, respectively. Fluorescent images of the rapidly frozen sections were obtained via an inverted fluorescence microscope; (B) shows image staining using haematoxylin and eosin (HE) merged with DAPI (D).

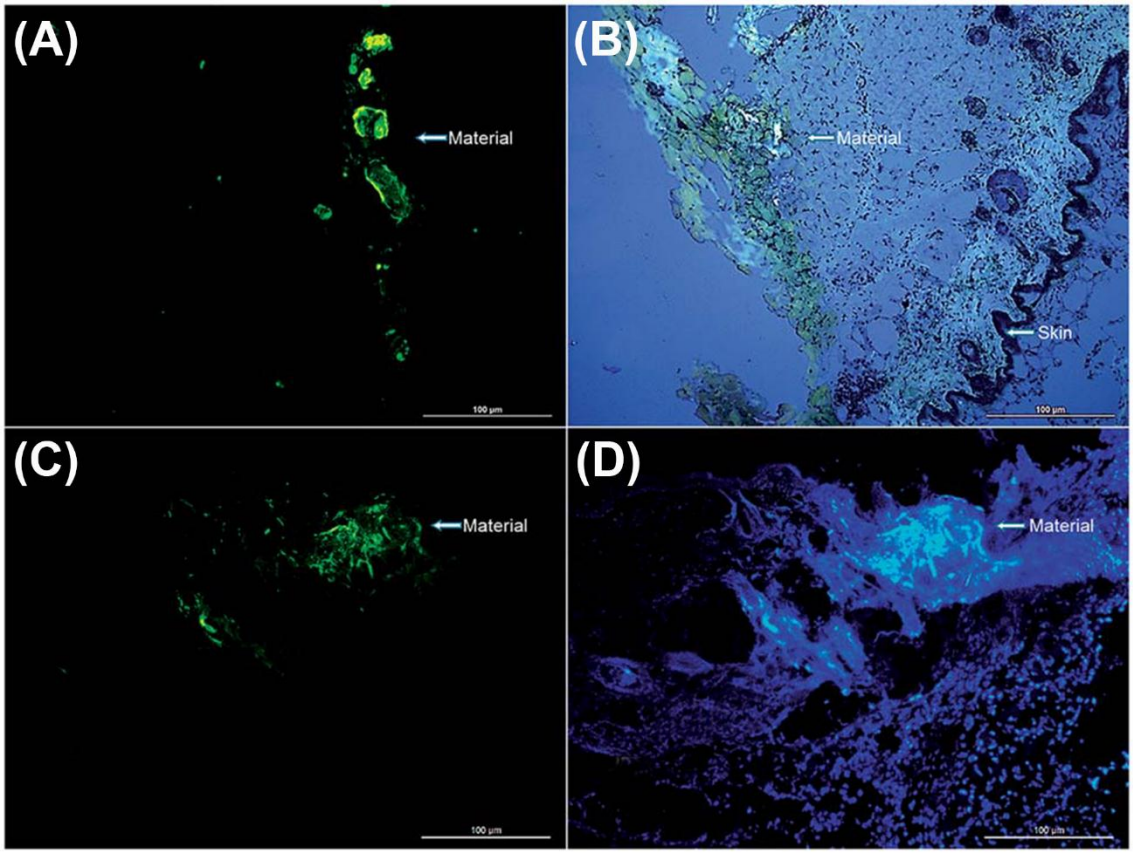

Figure 2-11 Fluorescent images of rapidly frozen sections were gathered via inverted fluorescence microscopy. (B) Shows image staining via haematoxylin and eosin (HE) merged with DAPI (D). The samples were harvested after one (A and B) and three months (C and D) of incubation. Adapted with permission from Zeng.[82] Copyright (2014) The Royal Society of Chemistry.

Conclusion

The doping of Tb^{3+} or Eu^{3+} ions will influence the crystal growth and morphology of apatite nanocrystals, and slightly change the binding energy or ion interaction. The proposed lattice models express reasonably the incorporation mechanism of Tb^{3+} ions into the apatite lattice, which would be important for understanding the mechanism of fluorescence emission. The hydrophobic surfaces of the nanorods were converted into hydrophilic surfaces with the surfactant of dextran. The rod-like nanoparticles showed excellent biocompatibility and strong luminescence and could be utilized for labelling and

tracking BMSCs *in vitro* and *in vivo* by our collaborator Dr. Haifeng Zeng from Plastic Surgery Hospital of Peking Union Medical College and Chinese Academy of Medical Sciences. Labelled BMSCs were shown to reproducibly exhibit osteogenic differentiation potential in real-time PCR and ELISA assays. Long-term *in vivo* cell-tracking experiments confirmed the stability of dextran-coated Tb-FA nanorods.

CHAPTER 3 INVESTIGATION ON STRUCTURE AND UPCONVERSION FLUORESCENCE OF YB^{3+}/HO^{3+} CO-DOPED FLUORAPATITE CRYSTALS FOR POTENTIAL BIOMEDICAL APPLICATION

Introduction

Some lanthanide ions-doped materials can emit visible fluorescence when exited by near-infrared (NIR) laser.[23, 89] Typically, the sensitizers (usually Yb^{3+}) successively absorb NIR excitations at a range of 700-1000 nm and transfer them to the activators (Ho^{3+}, Er^{3+}, or Tm^{3+} etc.), followed with short-wavelength emissions.[74, 90-92] Compared to organic luminophores and semiconductor quantum dots (QDs),[18, 21] these upconversion particles (UCPs) have such advantages as photostable, sharp visible emission bandwidth, and nontoxicity.[17, 31] UCPs are better for long-term bioimaging and cell tracking studies over organic luminophores which are subject to photobleaching and short excited state lifetimes, or QDs that show potential toxicity of cadmium and selenium, photoblinking, and short circulation half-time.[68, 72] In addition, different from conventional downconversion fluorescent labels requiring an ultraviolet or blue excitation wavelength, UCPs show deep penetration in tissues, multiplexing ability, and avoidance of tissue auto-fluorescence and possible fatal photodamage to cells.[21, 93] The UCPs are ideal fluorescent probes for a variety of biological applications, e.g. detection,[32, 94] imaging,[34, 35] cell tracking,[36] and therapy.[37] Popular host matrixes that can house rare-earth ions to trigger upconverting fluorescence comprise $NaYF_4$,[34] $NaGdF_4$,[40] and $LaPO_4$,[88] whereas their composition is not similar to biological apatite, which may block further *in vivo* biomedical applications. Herein we selected an apatite matrix that can not only house lanthanide ions but also possess good biocompatibility, and facilitate tissue-material interactions. Apatite crystals,

including hydroxyapatite [$Ca_{10}(PO_4)_6(OH)_2$, HA] and fluorapatite [$Ca_{10}(PO_4)_6F_2$, FA], are often used as substitutes of the inorganic component of bones and teeth,[4, 95] due to their structural similarity to bone mineral, excellent biocompatibility and bone-bonding bioactivity. Besides, HA and FA can act as good host materials for rare-earth doping as downconversion luminescent probes, such as FA-Eu[96] and HA-Tb[66]. Lanthanide ions have analogical radius as Ca^{2+} ions and high affinity to PO_4^{3-} ions,[65, 70] which can ensure the success of rare-earth doping. We chose FA as the doping matrix, because F^- ions can contribute materials with low phonon energies, which increase the number and probability of rare-earth luminescence transitions.[4] Though a few kinds of UCPs have appeared these years,[35, 71, 72] there are few reports on upconversion luminescence based on FA matrix. Combination of the upconversion fluorescent property of Yb/Ho ions, the excellent biocompatibility and typical crystal structure of FA will afford us to design a promising material for biomedical applications. The FA-based crystals have good crystal stability endowed by its hexagonal structure and F^- ions. Thus, FA matrix and Yb^{3+}/Ho^{3+} doping ions were chosen to synthesize FA:Yb^{3+}/Ho^{3+} crystals and investigate the possibility of upconversion fluorescence. In addition, bone marrow mesenchymal stem cells (BMSCs) have shown great potential in tissue engineering,[37, 72, 97] which should be beneficial for future biomedical application and investigation on cell imaging and tracking of the FA:Yb^{3+}/Ho^{3+} crystals.

In this work, we reported the exploration for preparation and characterization of FA:Yb^{3+}/Ho^{3+} upconversion crystals. The rare-earth co-doped crystals were synthesized by a modified hydrothermal method,[87, 98] followed by activating treatment at 700 °C. When excited under 980 nm NIR light, these crystals emitted bright green (543 nm) and red (654

nm) light, in a possible mechanism of excited state absorption (ESA) and energy transfer (ET). After surface coating with hydrophilic dextran, the crystals could exhibit distinct cell fluorescent imaging.

Materials and methods

Materials

$Ca(NO_3)_2 \cdot 4H_2O$, $Yb(NO_3)_3 \cdot 6H_2O$, $Ho(NO_3)_3 \cdot 6H_2O$, $Na_3PO_4 \cdot 12H_2O$, NaF, octadecylamine, oleic acid, ethanol, and cyclohexane in AR grade were obtained from Beijing Chemical Reagents Company, China. Dextran 20,000 in AR grade was purchased from Sinopharm Chemical Reagent Company, China. Other chemical agents obtained from commercial routes were of analytical grade and used without further purification.

Preparation of upconversion apatite nanocrystals co-doped with Yb^{3+} and Ho^{3+}

Octadecylamine (0.5 g) was dissolved in oleic acid (4 mL) and ethanol (16 mL) under magnetic stirring in a Teflon-lined autoclave (50 mL). Then aqueous solution of $Ca(NO_3)_2$ (0.28 M, 7 mL), $Ln(NO_3)_3$ (Ln: 0.20M Yb^{3+} + 0.02 M Ho^{3+}, 2 mL), Na_3PO_4 (0.20 M, 7 mL) was added. For FA: Yb^{3+}/Ho^{3+}, additional NaF (0.24 M, 2 mL) was added. Afterwards, the mixture was agitated for 10 min, and hydrothermally treated at 160 °C for 16 h. After cooling to room temperature naturally, the white precipitate collected by centrifugation (10 min at 2700 × g) was washed and activated at 700 °C in air for 2 h with a heating rate of 1 °C /min.

Coating of dextran on apatite nanocrystals

The prepared rare-earth doped crystals (0.5 g) were added into a dextran solution (1g, 7 mL) in a 10 mL round-bottom flask. The mixture was dispersed by ultrasonication, and

stirred for 2 h at room temperature to obtain a homogeneous phase. Then they were isolated by centrifugation (3 min at 2700 × g) and purified with distilled water and ethanol for three times separately. The product could be re-dispersed in aqueous solution.

Characterization

X-ray diffraction (XRD) powder patterns were acquired with a Philips X' Pert Pro MPD equipment in the 2θ range from 10º to 80º with Cu Kα radiation (λ = 1.5406 Å). TEM images of the crystals were collected on an FEI TecnaiG2 T20 instrument at 200KV. EDS data were obtained by both TEM and SEM (JEOL, JSM-5900LV). ICP-OES measurement was conducted on a Prodigy ICP-OES (Teledyne Leeman Labs), and every data point was expressed as a mean ± SD from triplicate dishes. The binding energy data were measured by XPS spectrum, AXIS Ultra DLD, Kratos, UK. FT-IR was recorded on a Perkin-Elmer 6000 Fourier transformation spectrometer, with a wavenumber range of 400-4000 cm^{-1}. The photoluminescence was recorded by the Hitachi F-7000 fluorescence spectrophotometer with an external 0-2 W adjustable diode laser integrated with an optical fibre (Beijing Hi-Tech Optoelectronic Co., China).

Cytotoxicity assay

Hela cells provided by Plastic Surgery Hospital of Peking Union Medical College, China were sued for the cytotoxicity assay. The cells were seeded in a 96-well flat-bottomed microplate (5000 cells/well) and cultured in 100 μL growth medium at 37 °C and 5% CO_2 for 24 h. Cell culture medium in each well was then replaced by 100 μL cell growth medium, containing FA:Yb^{3+}/Ho^{3+} crystals with concentrations of 100, 200, 400 and 800 μg mL^{-1}. After incubation for 1, 2, and 3 days at 37 °C, the crystals were washed with PBS for three times. 10 μL of CCK-8 dye and 100 μL of α-MEM cell culture medium

were added to each well, and cells were incubated further for 3 h at 37 °C. The absorbance at the wavelength of 450 nm was measured by a Varioskan Flash (Thermo Scientific).

Upconversion bioimaging

Bone marrow mesenchymal stem cells (BMSCs) were provided by Institute of Sports Medicine, Peking University Third Hospital, China. BMSCs were grown in α-MEM (Minimum Essential Medium, Alpha Modified) supplemented with 10% FBS (fetal bovine serum), and cultured at 37 °C under 5% CO_2. BMSCs were seeded onto 35 mm coverglass-bottom dishes and incubated in 2 mL of α-MEM at 37 °C for 24h. The culture medium was removed and the cells were incubated in 2 mL α-MEM containing FA:Yb^{3+}/Ho^{3+} crystals (100 μg mL^{-1}) at 37 °C for 24 h. After rinsing with PBS three times, cells were fixed with 4% paraformaldehyde for 15 min. Upconversion fluorescence imaging was conducted under a multiphoton confocal microscope (Leica TCS SP8) at 980 nm. The green and red upconversion luminescence emission was collected at 540 ± 40 nm and 650 ± 40 nm, respectively.

Statistical analysis

The results were expressed as mean ± standard deviation (SD). Statistical comparisons between groups were analyzed by using one-way ANOVA test. A value of $p < 0.05$ was considered to be statistically significant.

Results and discussion

In order to evaluating the efficiency of the doping system, we started the preliminary investigation to screen the rare-earth elements and validate our hypothesis, that is, apatite can be used as matrix for rare-earth doping upconversion luminescence. The hexagonal

apatite crystal structure is selected as the doping matrix, including hydroxyapatite ($Ca_{10}(PO_4)_6(OH)_2$, HA), fluorapatite ($Ca_{10}(PO_4)_6F_2$, FA). Various rare-earth elements were tried according to literature and our research needs, we found that several co-doped lanthanides worked for upconversion (UC) apatite system, with red, green, and blue emissions for respective lanthanide, as shown in Table 3-1. The luminescence color depends on their unique electron orbitals. Because human eyes are sensitive to red and green colors, we select Yb/Ho (ytterbium/holmium) for upconversion co-dopants. The morphologies of some lanthanides co-doped FA crystals are shown in Figure 3-1. We also studied tri-doping apatite (Table 3-2), but here we will mainly focus on single doping and co-doping. As a result, apatite (HA and FA) can be used as matrix for rare-earth doping of down- and up-conversion luminescence.

Table 3-1 Screening of the doping lanthanides for UC apatite system.

	Ho^{3+}/Yb^{3+}	Er^{3+}/Yb^{3+}	Tm^{3+}/Yb^{3+}
UC	Red, Green	Green	Blue

Table 3-2 Fluorescence of tri-lanthanides doping apatite system.

	UV	NIR
FA-Yb-Ho, Eu	red	green + red
FA-Yb-Ho, Tb	green	green
FA-Yb-Er, Eu	red	green
FA-Yb-Er, Tb	green	green
FA-Yb-Tm, Eu	red	-
FA-Yb-Tm, Tb	green	green

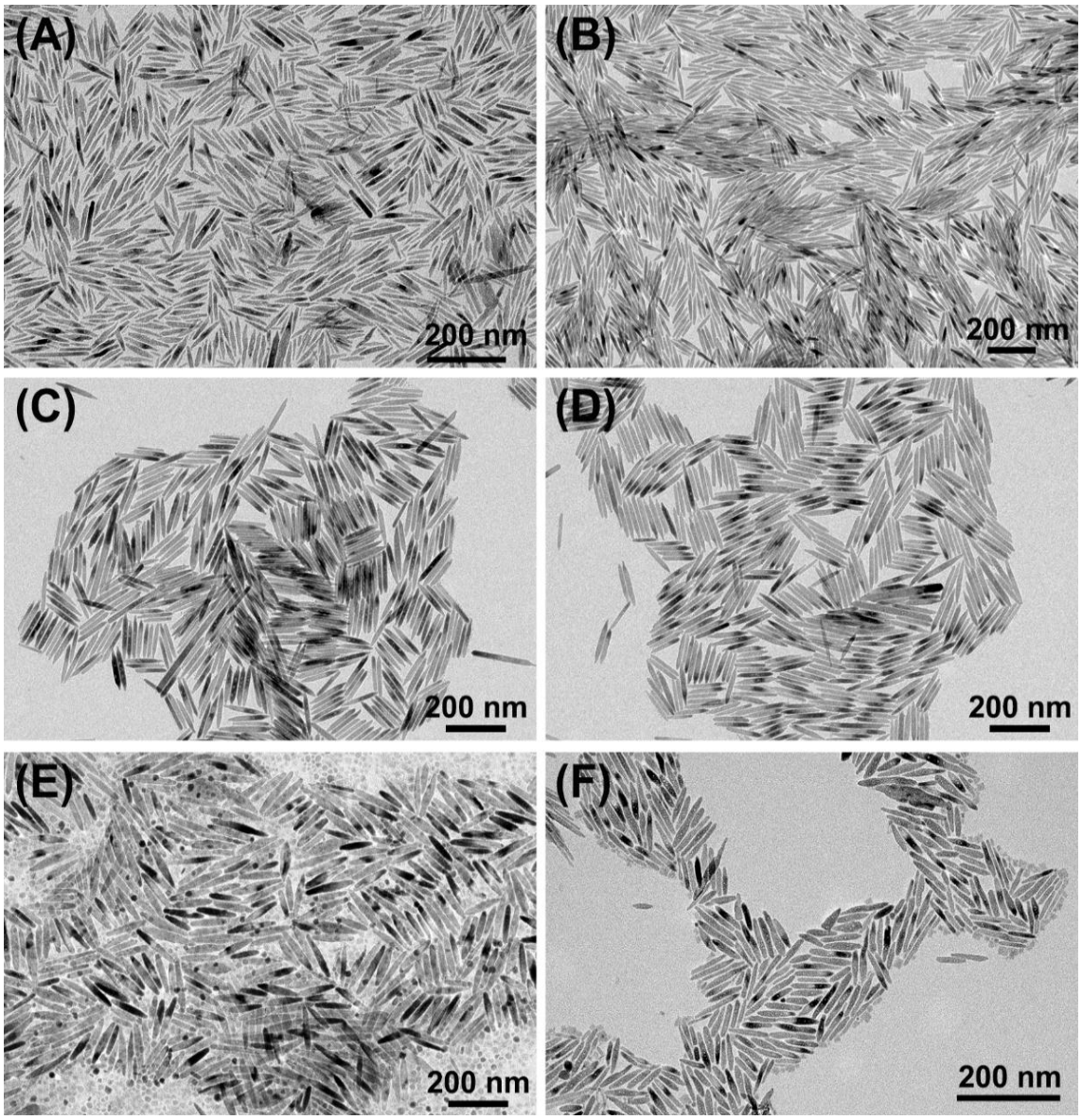

Figure 3-1 TEM morphologies of some lanthanides co-doped FA crystals. (A) FA-Yb-Er; (B) FA-Yb-Tm; (C) FA-Ce-Tb; (D) FA-Ce-Er; (E) FA-Yb-Tb; (F) FA-Yb-Nd.

Figure 3-2 showed the XRD patterns of the FA:Yb^{3+}/Ho^{3+} crystals after hydrothermal synthesis at 160 °C (A) and activation at 700 °C (B). It was noted that Figure 3-2A showed only an envelope curve, indicating a poorly crystallized apatite structure. Figure 3-2B showed a much higher crystallinity than Figure 3-2A, with sharp characteristic peaks at 25.9° (002), 32° (211), 33.1° (300), 40.1° (212), and 46.7° (222), which matched well with the classic hexagonal phase of $Ca_{10}(PO_4)_6F_2$ (JCPDS No. 77-0120) belonging to the $P6_3/m$

space group (176). The interplanar spacing of the [002] lattice plane was 3.42 Å or 0.342 nm. There were no impurity diffraction peaks or phases, such as those corresponding to rare-earth oxides, hydroxide, or fluoride, in the XRD patterns of the FA:Yb^{3+}/Ho^{3+} crystals, implying that the doping rare-earth ions were incorporated into the lattice of the fluorapatite crystals. The lattice parameters were determined by a least squares refinement using JADE software, with a = b = 0.938 nm, c = 0.688 nm for crystals synthesized at 160 °C and a = b = 0.936 nm, c = 0.687 nm for crystals treated at 700 °C, which both were in accord with the FA standard card (a = b = 0.937, c = 0.688 nm). However, the lattice parameters (a and c) of the crystals treated at 700 °C were slightly smaller than those of the crystals synthesized at 160 °C. This result indicates that the treatment at 700 °C makes the crystal structure denser due to recrystallization. The hexagonal crystal structure of fluorapatite has good crystal stability, which would be helpful for stable fluorescence expression of the embedded rare-earth ions.

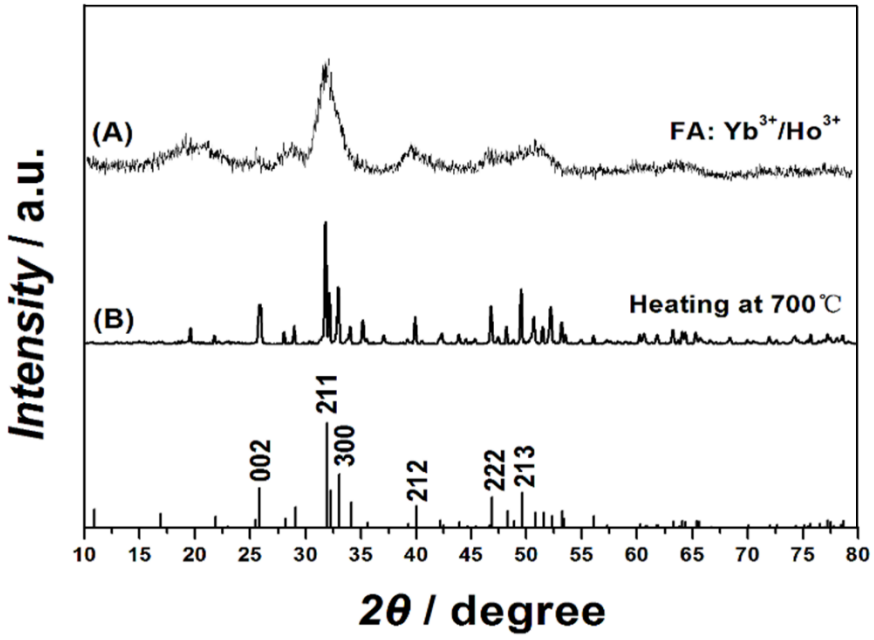

Figure 3-2 XRD patterns of FA:Yb^{3+}/Ho^{3+} crystals after hydrothermal synthesis at 160 °C for 16 h (A) and activation at 700 °C for 2 h (B).

Theoretically, we synthesized the rare-earth doped FA:Yb^{3+}/Ho^{3+} crystals according to a molar ratio of $X_{Ca}/Y_{Yb}/Z_{Ho}$ = 100/20/2 in the design formula of $(Ca_xYb_yHo_z)(PO_4)_6F_2$, through the reactions of $Ca(NO_3)_2$, $Yb(NO_3)_3$, $Ho(NO_3)_3$, Na_3PO_4, and NaF. Analytical data from the ICP-OES and SEM-EDS analyses (Table 3-3) illustrated that both Yb^{3+} and Ho^{3+} ions were incorporated into the FA crystals, and the measured molar ratio of $X_{Ca}/Y_{Yb}/Z_{Ho}$ in the synthesized FA:Yb^{3+}/Ho^{3+} crystals was found to be 100/16/2.1 by ICP-OES or 100/17/2.2 by EDS. The molar content of Yb^{3+} ions was slight lower than the theoretical value, while the content of Ho^{3+} ions was close to the theoretical value. Basically, the molar ratio of Ca/Yb/Ho is in accord with the theoretical ratio.

Table 3-3 The molar ratio of Ca, Yb, and Ho in FA:Yb^{3+}/Ho^{3+} crystals via ICP-OES and SEM-EDS.

	SEM-EDS (mol %)	ICP-OES (mol %)	Theoretical Value (mol %)
Ca/Yb/Ho	100/17/2.2	100/16/2.1	100/20/2

After doping with Yb^{3+} and Ho^{3+} ions, the binding energies of Ca, P, and O in the doped FA crystals displayed a slight increase, as shown in the XPS data in Table 3-4. This trend indicates that the substitution of Yb^{3+} and Ho^{3+} ions for Ca^{2+} ions changes both the lattice parameters and the binding energy. This increase in binding energy suggests a stronger ion interaction in the doped apatite crystal structure.

Table 3-4 The binding energy of ions in FA:Yb^{3+}/Ho^{3+} crystals.

	FA (eV)	FA:Yb^{3+}/Ho^{3+} (eV)
Ca (2p)	346.8	346.9
P(2p)	132.8	132.9
O(1s)	530.7	530.8

It is known that the molecular formula of apatite or doped apatite is difficult to precisely replicate, especially when trivalent rare-earth ions replace divalent calcium ions. Figure 3-3 displays a schematic diagram for the three situations of Yb/Ho-embedding lattice models along the fluorine channel of an FA crystal cell. If the molar ratio of Ca/Yb/Ho = 100/16/2.1 is used to calculate the molecular formula of the FA:Yb^{3+}/Ho^{3+} crystals, we obtain $(Ca_{8.5}Yb_{1.3}Ho_{0.2})(PO_4)_6F_2$; namely, in 10 crystal cells of FA:Yb^{3+}/Ho^{3+}, there are approximately 13 Yb^{3+} ions and 2 Ho^{3+} ions. Hence, each unit cell contains at least one Yb^{3+} ion, but only two unit cells contain both Yb^{3+} and Ho^{3+} ions. However, we will find a mismatch in the total valence in the formula $(Ca_{8.5}Yb_{1.3}Ho_{0.2})(PO_4)_6F_2$ when compared to $(Ca_{10})(PO_4)_6F_2$ of FA. For the balance of positive and negative valence, some Ca^{2+} vacancies or substitutions of O^{2-} for F^- should be present.[62] Moreover, a small number of monovalent sodium ions may exist to compensate for the valence mismatch. Indeed, Na^+ ions (Na 1s, 1070.8 eV) were found by the XPS analysis. Therefore, the substitution of Yb^{3+} or Ho^{3+} ions for Ca^{2+} ions in fluorapatite crystals should result in several different situations. The lattice occupation of Yb^{3+} and Ho^{3+} ions in 10 crystal cells can be divided into three situations: 1) one Yb^{3+} ion replaces one Ca^{2+} ion in each of five unit cells; 2) two Yb^{3+} ions replace two Ca^{2+} ions in each of three unit cells; and 3) one Yb^{3+} ion and one Ho^{3+} ion replace two Ca^{2+} ions in each of two unit cells. For the first situation, a reasonable valence-balanced formula is $(Ca_9Yb)(PO_4)_6FO$, or $(Ca_8YbNa)(PO_4)_6F_2$; for the second situation, the balanced formula could be $(Ca_7Yb_2©)(PO_4)_6F_2$ (©-Ca vacancy) or $(Ca_6Yb_2Na_2)(PO_4)_6F_2$; for the third situation, a reasonable balanced formula is $(Ca_7YbHo©)(PO_4)_6F_2$ (©-Ca vacancy) or $(Ca_6YbHoNa_2)(PO_4)_6F_2$.

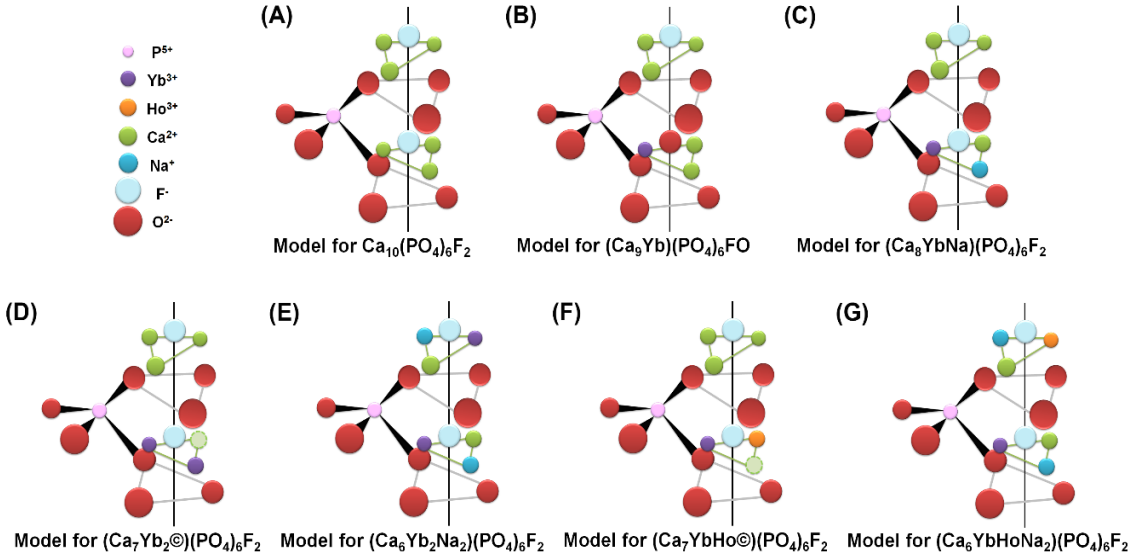

Figure 3-3 Schematic diagram of an Yb/Ho-embedding lattice model along the fluorine channel of FA crystal cell.

We further investigated the crystal morphology and structure by TEM combined with EDS, HRTEM imaging, and SAED (Figure 3-4). As shown in Figure 3-4A, the FA:Yb^{3+}/Ho^{3+} crystals after hydrothermal synthesis at 160 °C exhibited a fusiform morphology, with an average crystal size of approximately 26 nm by 250 nm. After activation treatment at 700 °C, these crystals still showed a slender shape with an average size of 16 nm by 286 nm (Figure 3-4B). The average center diameter of the nanocrystals decreased to 16 nm from 26 nm (a decrease of approximately 38%) while the average length increased to 286 nm from 250 nm (an increase of approximately 14%). This behavior indicates that recrystallization occurs during the heating process, which agrees well with the enhanced crystallinity shown in Figure 3-2B. Figure 3-4C provided a TEM-EDS element mapping of the crystals, demonstrating the successful incorporation of Yb^{3+} and Ho^{3+} ions in the crystal structure. Figure 3-4D displayed a HRTEM image showing the presence of 2D lattice fringes for a single slender FA:Yb^{3+}/Ho^{3+} crystal. The crystal showed preferential growth along the [002] direction, and the interplanar spacing of the [002]

lattice plane was 0.346 nm, in accord with the results (0.342 nm) from XRD analysis. Figure 3-4D also showed an inset of SAED pattern for the (002), (212), and (211) planes, which were in good agreement with the XRD pattern. The results confirm that the slender crystals exhibit a typical single crystal structure with uniform morphology and good crystallinity. The good dispersity and narrow size distribution of these crystals are expected to arise from the surfactant intervention during hydrothermal synthesis, the freeze-drying process, and the relatively lower activation temperature compared to previous studies conducted at 900 °C.

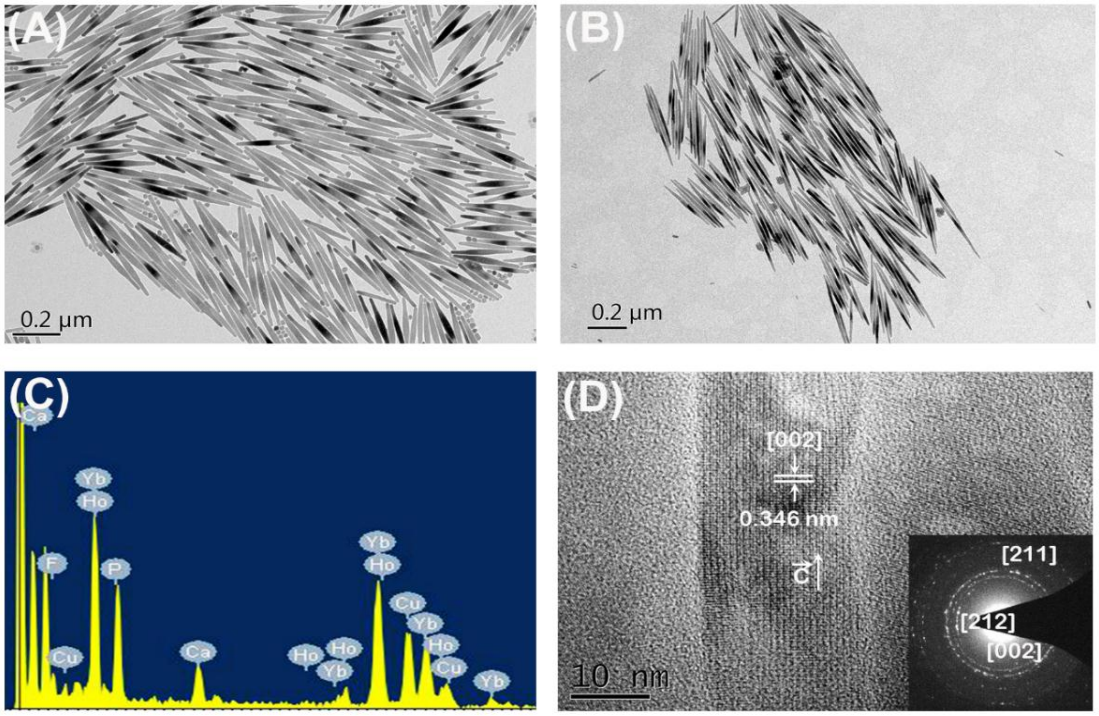

Figure 3-4 TEM micrographs of FA:Yb^{3+}/Ho^{3+} crystals after hydrothermal synthesis at 160 °C (A) and activation at 700 °C (B); Element mapping by EDS (C), and HRTEM image of FA:Yb^{3+}/Ho^{3+} single crystal with inset of SAED pattern (D).

The activating treatment of rare-earth co-doped material is important for acquiring stable upconversion emission. We chose 700 °C for our treatment of Yb^{3+}/Ho^{3+} co-doped apatite nanocrystals because it was found that at these temperature, the FA:Yb^{3+}/Ho^{3+}

nanocrystals exhibited an obvious upconversion emission while maintaining good dispersity. For treatment at temperatures under 650 °C, almost no apparent upconversion emission was present. Above 750 °C, the nanocrystals melted and fused together to form a ceramic state. Thus, treatment at 700 °C enhances the crystallinity and structure stability of the FA:Yb^{3+}/Ho^{3+} crystals, which especially promotes the upconversion effect. When excited by 980-nm NIR light, the Yb^{3+}/Ho^{3+} co-doped crystals chiefly displayed two fluorescence emission bands, namely, a green band centered at 543 nm and a red band near 654 nm, while the crystals that were not activated at 700 °C did not exhibit any obvious emission (Figure 3-5A). The 491-nm emission should be attributed to the 980-nm laser. To determine the number of photons (n) involved in the upconversion process, the pump power dependence of the luminescence intensity was investigated, as shown in Figure 3-5B. The slope (n) values were 2.0 for both the green and red emission bands, demonstrating that a two-photon absorption process is involved in the upconversion emission.

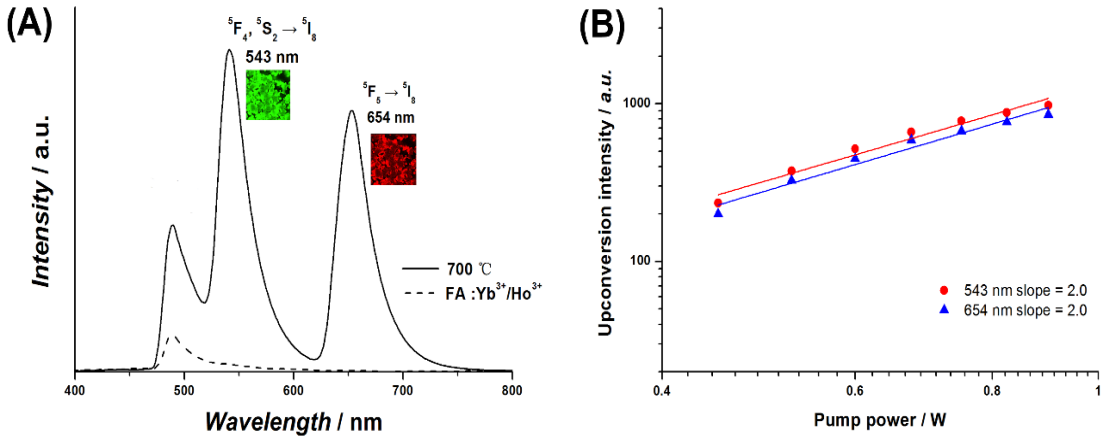

Figure 3-5 Upconversion emission spectra (A) of FA:Yb^{3+}/Ho^{3+} crystals with (solid curve) and without (dashed curve) activation at 700 °C, and insets of laser confocal images; dependence of upconversion emission intensities on NIR pump power (B).

Although a few Yb^{3+}/Ho^{3+} co-doped upconversion materials have been reported,[99, 100] biocompatible fluorapatite used in this experiment solely acts as a matrix for UCPs,

and thus, the upconversion mechanism needs further exploration. Here, we speculate a mechanism for the upconversion process of the FA:Yb^{3+}/Ho^{3+} crystals upon NIR excitation at 980 nm (Figure 3-6). In the crystal lattice of FA, some Ca^{2+} sites are occupied by Yb^{3+} and Ho^{3+} ions. Because the content of Yb^{3+} ions is much higher than that of Ho^{3+} ions, each Ho^{3+} ion is surrounded by several Yb^{3+} ions in the FA crystal. First, the sensitizer Yb^{3+} ions are excited from the $^2F_{7/2}$ to $^2F_{5/2}$ level upon the absorption of NIR photons (980 nm). The ions then transfer energy to the adjacent activator Ho^{3+} ions, exciting the ground Ho^{3+} ions to the $^5I_6$ level. For green emission, Ho^{3+} ions at the $^5I_6$ level can be directly excited to the $^5F_4$, $^5S_2$ level by absorbing energy from the laser photons (excited state absorption, ESA).[71] For red emission, the Ho^{3+} ions at the $^5I_6$ level can drop to the $^5I_7$ level via nonradioactive phonon-assisted relaxation; they can then be excited to the $^5F_5$ level by absorbing energy from the laser photons. The radioactive transfer of the Ho^{3+} ($^5F_4$, $^5S_2$) and Ho^{3+} ($^5F_5$) ions to the ground state results in green emission centered at 543 nm and red emission centered at 654 nm, respectively. The Yb^{3+} ions surrounding the Ho^{3+} ions are helpful for facilitating excitation energy transfer and are also separated by a considerable number of optically inactive Ca^{2+} ions to avoid energy migration to capture traps.

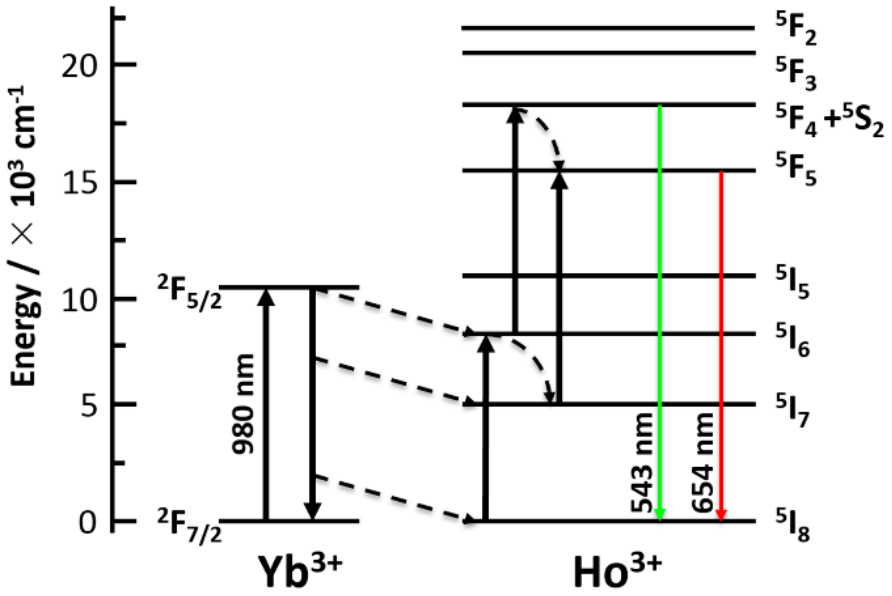

Figure 3-6 Schematic energy-level diagram of Ho^{3+} and Yb^{3+} ions and upconversion luminescence mechanism for FA:Yb^{3+}/Ho^{3+} crystals.

The proliferation of cells cultured with different dosages of FA:Yb^{3+}/Ho^{3+} crystals was evaluated using a cell counting kit-8 (CCK-8) assay. Figure 3-7 showed that the cell proliferation for different dosage groups increased markedly and continuously with time, showing a normal growth trend, even at a high dosage of 400 μg mL^{-1}. On Day 1, all experimental groups showed proliferation comparable to the control ($p > 0.05$). On Day 3, although the cell proliferation for the 100 and 200 μg mL^{-1} dosage groups were lower than that of the control and the 400 and 800 μg mL^{-1} dosage groups ($p < 0.05$), they still exhibited a normal growth status. This result indicates that the cytotoxicity of the rare-earth doped crystals is tolerable, allowing for further studies of live-cell imaging.

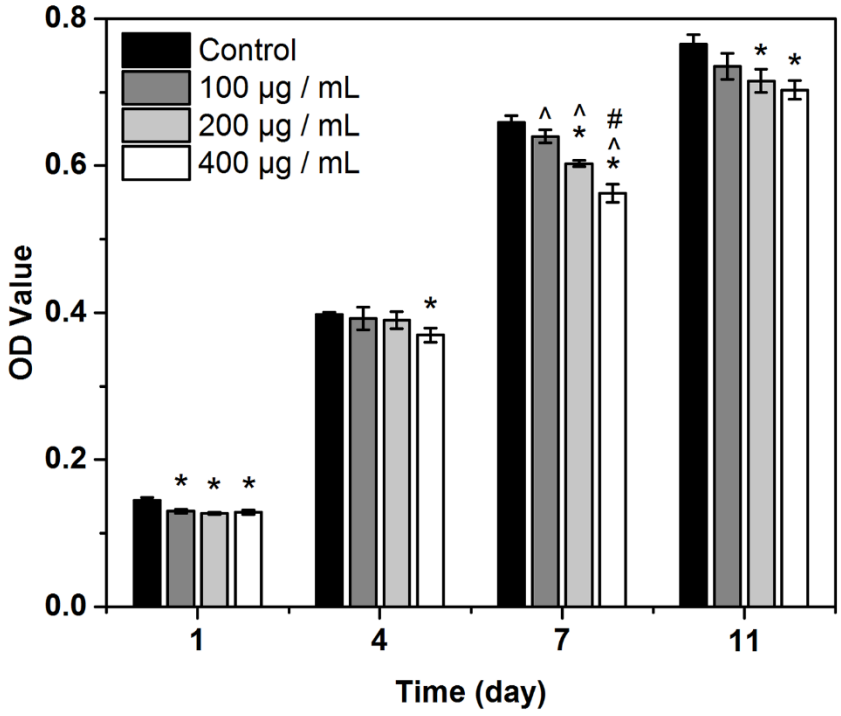

Figure 3-7 CCK-8 assay of cell proliferation after cultured with different dosages of FA:Yb^{3+}/Ho^{3+} crystals for 1, 2, and 3 days, error bars represent mean ± SD from triplicate experiments, $p < 0.05$ (* vs. control, ^ vs. 100 μg/mL, # vs. 200 μg/mL).

To explore the potential of FA:Yb^{3+}/Ho^{3+} crystals for future biomedical applications, we used hydrophilic dextran to graft the surface of these crystals for cell imaging. Figure 3-8 showed the FT-IR spectra of the FA:Yb^{3+}/Ho^{3+} crystals treated at 700 °C, the dextran and dextran-grafted FA:Yb^{3+}/Ho^{3+} crystals. The absorption peaks at 3411 and 1652 cm^{-1} in Figure 3-7C attribute to the typical stretching vibration and bending vibration of the -OH groups, and the absorption peak at 2930 cm^{-1} is the typical stretching vibration of C-H in dextran. By comparing Figure 3-8C with Figure 3-8B, the presence of $-CH_2$ and -OH peaks and the peak shift (e.g., from 2926 to 2930 cm^{-1} for $-CH_2$ groups) provide evidence of successful grafting of hydrophilic dextran on the crystals. The peak shift should be caused by the bonding or interaction between the crystals and dextran. Other peaks at 1043 and 960 cm^{-1} (asymmetrical stretching vibration) and 606 and 575 cm^{-1} (bending vibration)

correspond to the PO_4^{3-} groups, similar to the FA:Yb^{3+}/Ho^{3+} crystals without a grafting (Figure 3-8A). The dextran-grafted FA:Yb^{3+}/Ho^{3+} crystals are small in size and exhibit distinct upconversion fluorescence, good cytocompatibility, and crystal stability, making them suitable for bioimaging investigation.

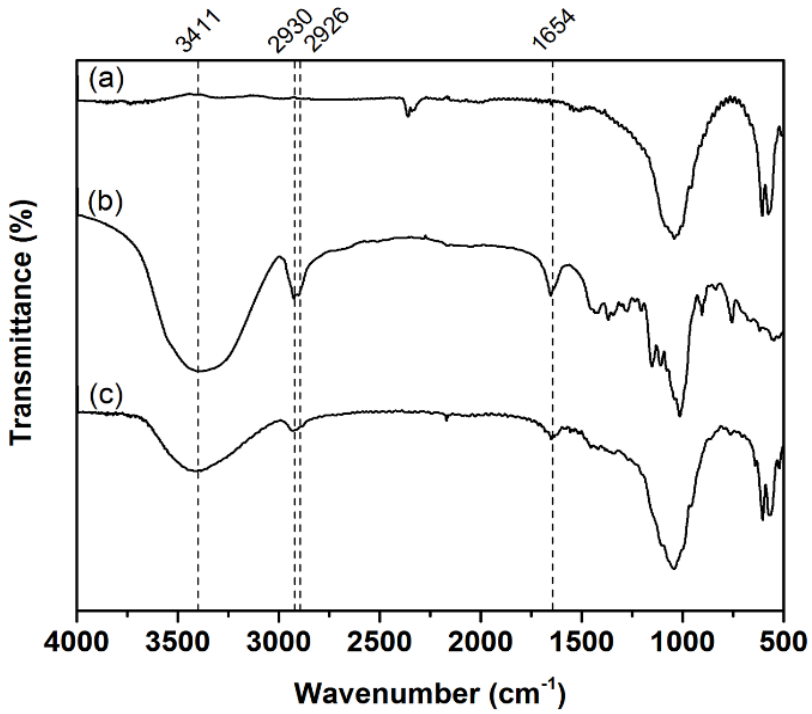

Figure 3-8 FTIR spectra of the FA:Yb^{3+}/Ho^{3+} crystals treated at 700 °C (a), dextran (b) and dextran-grafted FA:Yb^{3+}/Ho^{3+} crystals (c).

A combination of 100 μg mL^{-1} dextran-grafted FA:Yb^{3+}/Ho^{3+} crystals and BMSCs was used to investigate the possibility of cell imaging. The results of *in vitro* cell imaging demonstrated the cellular uptake of the crystals, as shown in Figure 3-9. When BMSCs treated with these crystals were exposed to 980-nm excitation, the cells showed strong cellular upconversion fluorescence. The cell morphology and cytoplasm could be clearly observed. The green (A) and red (B) fluorescent images of the cells matched well with the bright-field image of the cells (C) and provided clear overlap images (D). Moreover, the

upconversion luminescence of the FA:Yb^{3+}/Ho^{3+} crystals was stable and reproducible; the samples maintained reproducibility after 7 days. This result indicates the feasibility of using these upconversion crystals for cell imaging and tracking via their easy translocation into the cytoplasm of cells. Furthermore, the optical absorption of cellular components under NIR excitation is much lower than that for UV or visible light, which is helpful for reducing photodamage and for improving the sensitivity due to the absence of auto-fluorescence.[97] These features can also pave the way for imaging and tracking cells with multilineage differentiation.

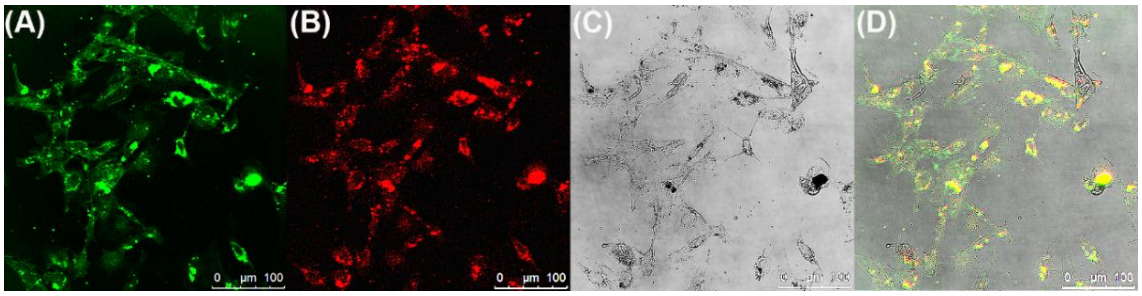

Figure 3-9 Multiphoton confocal luminescence images (excited by 980 nm light) of BMSCs incubated with 100 μg mL^{-1} dextran-grafted FA:Yb^{3+}/Ho^{3+} crystals for 24 h at 37 °C. The photos showed green (A) and red (B) upconversion luminescence images of BMSCs, bright-field of the cells (C) and overlay image (D) of green plus red. The green and red upconversion luminescence emission was collected at 540 ± 40 nm and 650 ± 40 nm, respectively.

In addition to cell imaging, the Yb^{3+}/Ho^{3+} co-doped apatite nanocrystals will have broad applications in biomedical fields. Using the good biocompatibility, bone-bonding bioactivity, and upconversion fluorescence of these rare-earth doped apatite nanocrystals, we can produce porous composite scaffolds with biodegradable polymers to investigate the process of bone repair and regeneration, determine whether synthetic apatite nanocrystals can incorporate into newly formed bone, reveal the bone-biomaterial interface via fluorescent imaging, trace the degradation of scaffolds, distinguish the scaffold material from bone tissue in histological sections, etc. Therefore, investigations on the upconversion

properties of such Yb^{3+}/Ho^{3+} co-doped apatite nanocrystals have significance in scientific studies and biomedical applications.

To identify the uptake of FA: Yb^{3+}/Ho^{3+} crystals into $BMSCs^{GFP}$, we performed TEM and two-photon confocal microscopy imaging. TEM imaging was obtained after $BMSCs^{GFP}$ were incubated for 24 h in 50 mg mL^{-1} FA: Yb^{3+}/Ho^{3+} modified medium and, as shown in Figure 3-10A, confirmed a strong uptake of crystals in the cytoplasm of the $BMSCs^{GFP}$, where strong-dark electron-dense nanoparticles are easily observed (indicated by red arrows). The emission spectrum of GFP (Em 503 ± 40 nm) is partly overlapped with the upconversion luminescence of FA: Yb^{3+}/Ho^{3+} crystals at 543 ± 20 nm (B). Therefore, in the following experiments, we chose GFP and upconversion luminescence of FA: Yb^{3+}/Ho^{3+} crystals at 654 ± 60 nm to track the $BMSCs^{GFP}$. As shown in Figure 3-9C, $BMSCs^{GFP}$ treated with 50 mg mL^{-1} FA: Yb^{3+}/Ho^{3+} crystals, demonstrated strong cellular upconversion fluorescence and GFP when excited at 980 nm. Meanwhile, two-photon confocal microscopy scanning of $BMSCs^{GFP}$ after treatment with 50 mg/mL FA: Yb^{3+}/Ho^{3+} demonstrated successful uptake of crystals in the $BMSCs^{GFP}$ (C, D).

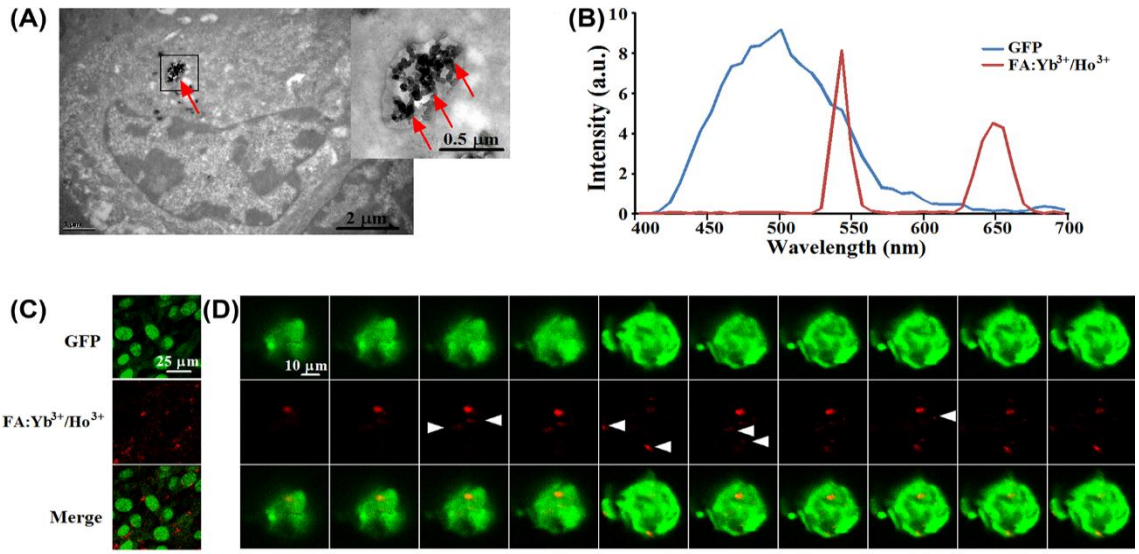

Figure 3-10 Uptake of FA:Yb^{3+}/Ho^{3+} crystals into $BMSCs^{GFP}$. (A) TEM images of $BMSCs^{GFP}$ after incubation with 50 mg mL^{-1} FA:Yb^{3+}/Ho^{3+} crystals for 24 h at 37 °C. (Red arrows) (B) Fluorescence spectra of GFP and FA:Yb^{3+}/Ho^{3+} crystals. (C) Two-photon confocal luminescence images (excited by 980 nm light) of $BMSCs^{GFP}$ treated as in (A). (D) Two-photon confocal microscope scanning of $BMSCs^{GFP}$ after treatment with 50 mg mL^{-1} FA:Yb^{3+}/Ho^{3+} (excited by 980 nm light). (White triangle). Adapted with permission from Hu.[101] Copyright (2015) Elsevier.

After four weeks' implantation, newly formed tissues displayed a translucent and cartilage-like appearance [Figure 3-11A (a)]. We observed no obvious difference in the gross appearance between the control group and the FA: Yb^{3+}/Ho^{3+} treated group [A (b)]. H&E staining [B (a and b)] revealed a well-defined construct of transplanted cells in the DCCBM scaffold *in vivo*. After staining with toluidine blue [B (c and d)], the BMSCsGFP from the control group and the FA: Yb^{3+}/Ho^{3+} treated group displayed uniform, positive staining for cartilaginous ECM. In order to determine cartilaginous differentiation, we used immunohistochemical staining to detect cartilage-related protein Col2A (B (e and f). The results were consistent with toluidine blue staining, indicating that $BMSCs^{GFP}$ treated with 50 mg mL^{-1} FA: Yb^{3+}/Ho^{3+} also differentiated into chondrocytes *in vivo*.

Further, we detected GFP fluorescence and upconversion fluorescence of $BMSCs^{GFP}$

using two-photon confocal microscopy (excited at 980 nm). As shown in Figure 3-12A and B, the upconversion fluorescence of FA: Yb^{3+}/Ho^{3+} crystals was observed at both 4 weeks and 12 weeks post transplantation; while GFP fluorescence was significantly decreased at 12 weeks post $BMSCs^{GFP}$ transplantation, compared with that of 4 weeks. These results imply that FA: Yb^{3+}/Ho^{3+} crystals have high biocompatibility and stability and can be utilized for tracking and monitoring BMSCs *in vitro* and *in vivo*.

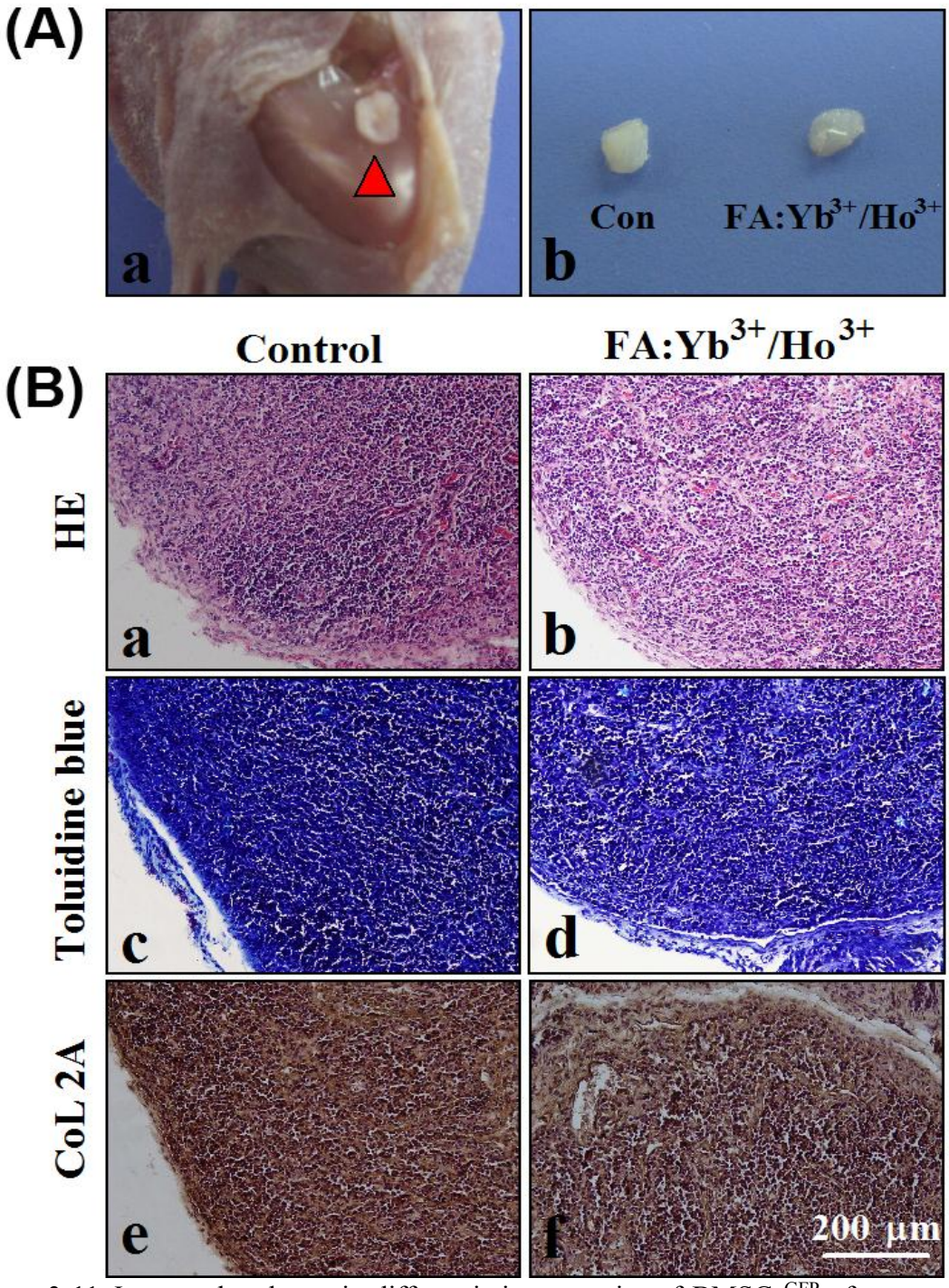

Figure 3-11 *In vivo* chondrogenic differentiation capacity of $BMSCs^{GFP}$ after treatment with 50 mg mL^{-1} $FA:Yb^{3+}/Ho^{3+}$ crystals. (A) Mass growth of cartilage constructs after four weeks *in vivo*. (B) (a, b) HE staining showing cell morphology and distribution. (c, d) Toluidine blue staining. (e, f) Immunohistological staining for type II collagen. Adapted with permission from Hu.[101] Copyright (2015) Elsevier.

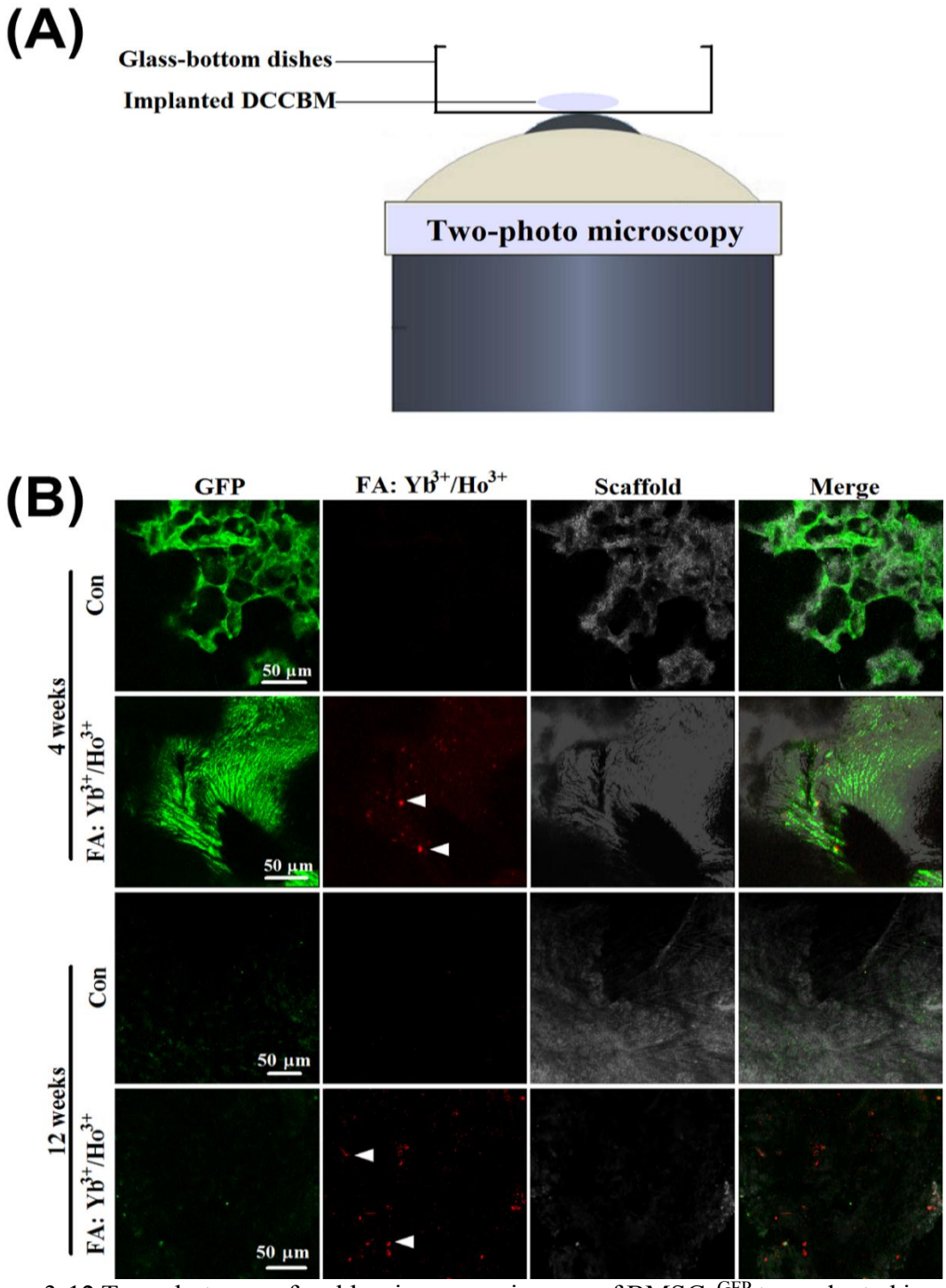

Figure 3-12 Two-photon confocal luminescence images of $BMSCs^{GFP}$ transplanted in nude mouse. (A and B) $BMSCs^{GFP}$ treated with or without 50 mg mL^{-1} FA:Yb^{3+}/Ho^{3+} for two days were seeded on the perforated DCCBM scaffold and induced in the chondrogenic differentiation medium for five days, before DCCBM was subcutaneously implanted in nude mice. $BMSCs^{GFP}$ were observed by two-photon confocal microscope (excited at 980 nm) at 4 and 12 weeks after transplantation, respectively. Adapted with permission from Hu.[101] Copyright (2015) Elsevier.

Conclusion

Fluorapatite crystal matrix was chosen for doping of Yb^{3+} and Ho^{3+} ions for the first time, which have successfully realized the upconversion luminescence. The substitution of Yb^{3+} and Ho^{3+} ions for Ca^{2+} ions results in the change of both lattice parameters and binding energy. The proposed lattice models demonstrate the importance of coexistence of different lattice substitution of Yb^{3+} and Ho^{3+} ions in the FA crystal structure. When excited by 980 nm near-infrared light, the FA:Yb^{3+}/Ho^{3+} crystals display bright green and red emission with narrow emission bands at 543 and 654 nm, respectively. After surface coating with hydrophilic dextran, the crystals exhibit distinct cell fluorescent imaging by entering the cytoplasm of cells. Our collaborator Dr. Xiaoqing Hu from Peking University Third Hospital determined the chondrogenic differentiation potential of the labeled $BMSCs^{GFP}$ using real-time RT-PCR analysis, histological assessment and immunohistochemistry. The continuous luminescence was detected after 12 weeks post transplantation from the FA: Yb^{3+}/Ho^{3+} upconversion crystals, while the GFP signal was significantly decreased after this time. The rare-earth doped crystals with good cytocompatibility, stable crystal structure, fluorescent repeatability and bioactivity have good prospect for biomedical applications.

CHAPTER 4 LANTHANIDES DOPED UPCONVERSION NANOAPATITE FOR SMART BIOIMAGING DURING BONE REGENERATION

Introduction

Over the past decade, considerable interest has been given to the design of scaffolds for bone tissue engineering, which is essential as a guiding structure for bone in-growth.[102] In principle, apatite scaffolds or apatite/polymer composite scaffolds can bond with bone tissues and are expected to degrade while the newly formed bone tissue infiltrates.[83] Hematoxylin and eosin (H&E) or Masson's staining are usually adopted to distinguish the newly formed bone tissue on the histological section of scaffolds implanted *in vivo*.[3] However, it is still difficult to clearly distinguish the scaffold material and material-tissue interface on these histological sections. Previous studies have used environmental scanning electron microscopy (ESEM) to distinguish the newly mineralized bone from the biphasic calcium phosphate (BCP) scaffold during osteogenesis based on the image grey values.[8] However, this method only provides a limited field of view, hardly allowing a full correlative investigation on changes in the ultrastructure over a macroscopic sample. Small-angle X-ray scattering (SAXS) remains constrained to isotropically oriented ultrastructures.[9] Therefore, novel methods are needed to distinguish the scaffold from the newly formed bone tissue on histological sections. Incorporating fluorescence into scaffolds is one prospective strategy for achieving this purpose.

Fluorescent probes play a key role in bioimaging to label the target and amplify fluorescent signal. The fluorophore can absorb light and jump to an excited state and then return to the ground state by emitting lower energy light. This energy difference between

excitation and emission is called the Stokes shift.[17] As microscopes have become more advanced, traditional organic fluorophores such as green fluorescent protein (GFP) have become disadvantaged in their probe brightness and stability.[18] Besides, cells may have many fluorescent components of their own, resulting in unwanted background fluorescence known as auto-fluorescence. Newly developed semiconductor quantum dots (QDs) have also shortcomings in toxicity, photo-blinking, and short circulation half times.[21] Recently, lanthanide doped upconversion particles have drawn great attention due to their photostability, high contrast and low toxicity.[22, 23] The upconversion process was first proposed in 1959,[29] which involves anti-Stokes shifts by upconverting low energy photons into high energy photons. When excited by a 980 nm NIR laser, the sensitizers (Yb^{3+} ions) can transfer energy to the nearby activators (Ho^{3+}, Er^{3+}, and Tm^{3+} ions) to emit short-wavelength luminescence. Lanthanide ions are good candidates for upconversion luminescence because of their multiple metastable electron states. Moreover, near infrared (NIR) light can penetrate deeper in the body and shows less damage to cells than UV and blue light. Upconversion particles as biomarkers are attractive for use in design of new probes and bioimaging applications. Work has been performed on multicolor tuning of upconversion probes and minimizing heating effect of excitation.[35, 73] Additional studies have shown applications in long-term real-time cell imaging[68] and in small-animal imaging.[74] However, there have so far been no reports on the potential of upconversion materials in labeling scaffold materials and the material-tissue interface.

The inorganic mineral of human hard tissues is mainly composed of nanoapatite.[2] Synthetic nanoapatite including hydroxyapatite [$Ca_{10}(PO_4)_6(OH)_2$, HA] and fluorapatite [$Ca_{10}(PO_4)_6F_2$, FA] are good candidates for repair of bone and teeth due to their structural

similarity to the mineral, excellent biocompatibility, and high osteogenicity.[103-105] Both HA and FA crystals have a hexagonal structure in which the Ca^{2+} sites can be easily substituted by other metal ions, such as Mg^{2+}, Sr^{2+}, Ln^{3+}, etc.[77, 106, 107] The apatite structure has been employed as a stable host matrix for lanthanide doping in previous studies on both downconversion[82, 108] and upconversion nanoparticles.[101, 109] The successful doping of lanthanides result from their high affinity to PO_4^{3-} ions and a similar ionic radius to calcium.[65] We hypothesize that lanthanide-doped apatites with stable upconversion luminescence and bone-bonding capacity will provide a novel method for distinguishing implanted bone scaffold materials from host tissue, as well as show their respective distribution. This method can also be useful for long-term *in vivo* tracking of implanted material or scaffolds and their degraded fragments.

In this study, lanthanide Yb^{3+} and Ho^{3+} co-doped fluorapatite (FA:Yb^{3+}/Ho^{3+}) and hydroxyapatite (HA:Yb^{3+}/Ho^{3+}) nanoparticles with varying dopant concentration were prepared by hydrothermal synthesis at 180 °C for 16 h, and activated at 700 °C for 2 h. The upconversion emissions of these nanoparticles were detected by fluorescence spectrometry. Cell proliferation was analyzed before performing animal experiment. Histological sections of the harvested *in vivo* samples treated by Masson's staining were imaged by inverted fluorescence microscopy and laser confocal microscopy, to distinguish the implanted material from newly formed bone tissue and track the material's distributions during osteogenesis *in vivo*.

Materials and methods

Materials

$Ca(NO_3)_2 \cdot 4H_2O$, $Yb(NO_3)_3 \cdot 6H_2O$, $Ho(NO_3)_3 \cdot 6H_2O$, $Na_3PO_4 \cdot 12H_2O$, NaF, and

ethanol at AR grade were obtained from Beijing Chemical Reagents Company, China. All other chemical agents obtained from commercial routes were of analytical grade and used without further purification.

Preparation of FA:Yb^{3+}/Ho^{3+} and HA:Yb^{3+}/Ho^{3+} nanoparticles

The Yb^{3+}/Ho^{3+} co-doped apatite precipitates were hydrothermally synthesized referring to previous method.[109] Briefly, an aqueous solution of Na_3PO_4 (0.20 M, 7 mL) and NaF (0.24 M, 2 mL, for FA only) was slowly dripped into a solution of $Ca(NO_3)_2$ (0.28 M, 7 mL), $Yb(NO_3)_3$ (0.10 M, 2 mL), and $Ho(NO_3)_3$ (0.005~0.03 M, 2 mL). Surfactant like octadecylamine, oleic acid or ricinoleic acid was selectively added during synthesis according to experimental needs. The molar concentration of Yb^{3+} and Ho^{3+} ions relative to Ca^{2+} ions was set as 10:0.5 to 10:3 (Table 4-1). Afterwards, the mixture was agitated for 10 min and hydrothermally treated at 180 °C for 16 h. After cooling to room temperature, a white precipitate was collected by centrifugation (10 min at 2700 × g), and rinsed in DI water and ethanol, respectively. Samples were freeze-dried and activated at 700 °C for 2 h at a heating rate of 1 °C /min.

Table 4-1 Concentrations of the co-doped Yb^{3+} and Ho^{3+} ions relative to Ca^{2+} ions in FA:Yb^{3+}/Ho^{3+} and HA: Yb^{3+}/Ho^{3+} materials.

Sample	Yb^{3+} (mol%)	Ho^{3+} (mol%)
1	10	0.5
2	10	1
3	10	2
4	10	3

Characterization

X-ray diffraction (XRD) powder patterns were acquired with a Philips X' Pert Pro MPD (Netherland) apparatus over a 2θ range of 10º to 80º using Cu Kα radiation (λ = 1.5406 Å). TEM images of the particles were measured by an FEI TecnaiG2 T20 instrument (USA) at 200 kV along with EDS, HRTEM image and SAED pattern. FT-IR spectra were recorded on a Perkin-Elmer 6000 Fourier transformation spectrometer (USA), with a wavenumber range of 500-3500 cm^{-1}. The photoluminescence behavior was recorded using a Hitachi F-7000 fluorescence spectrophotometer (Japan) attached with an external 2W adjustable diode laser (Beijing Hi-Tech Optoelectronic Co., China).

Cell culture

MG63 osteoblast-like cells were used to evaluate the biological properties of FA:Yb^{3+}/Ho^{3+} powder. MG63 cells were provided by the West China Hospital. The cells were cultured in F12 medium (Cell culture grade, Biowhittaker, Walkersville, MD) supplemented with 10% (v/v) calf serum (Cell culture grade, Gibco, Rockville, MD), 1% penicillin/streptomycin and 1% L-glutamine. Cells were subcultured once a week using Trypsin/PBS and maintained at 37 °C in a humidified atmosphere of 5% CO_2 in air. The medium was changed every three days.

Cell viability

A serial dilution was performed from an 800 μg/mL stock solution of FA:Yb^{3+}/Ho^{3+}. F12 medium was added in a 1:1 ratio, resulting in a final FA:Yb^{3+}/Ho^{3+} concentration range of 100-400 μg/mL. MG63 cells with the FA:Yb^{3+}/Ho^{3+} solution were seeded onto 96-well tissue culture plates (Corning, USA) with a density of 2×10^4 cells/well). Afterwards, the seeded samples were cultured in a humidified incubator (37 °C, 5% CO_2) for 11 days, and

the medium was changed every two days. MG63 cells cultured in F12 served as the control.

Cell viability was measured as a function of mitochondrial nicotinamide adenine dinucleotide (NADH)/nicotinamide adenine dinucleotide phosphate (NADPH)-dependent dehydrogenase activity. The activity was measured by the conversion of 3-(4,5-dimethylthiazol-2-gl)-5-(3-carboxymethoxylphenyl)-2-(4-sulphophenyl-2H) tetrazolium salt (MTT) into a soluble formazan dye with the CellTiter 96 Aqueous non-radioactive cell proliferation assay (Promega, USA). After 1, 4, 7, and11 days following cell seeding, the culture medium was removed and 200 μL of MTT-F12 solution was added to each well. Following incubation at 37 °C for 4 h in a fully humidified atmosphere at 5% CO_2 in air, MTT was taken up by active cells and reduced in the mitochondria to an insoluble purple formazan granule. Subsequently, the media was discarded and the precipitated formazan was dissolved in DMSO (150 μL/well). Optical density of the solution was evaluated using a microplate spectrophotometer (PerkinElmer wallac 1420, USA) at a wavelength of 570 nm. The results are presented as mean ± SD from triplicate wells.

***In vivo* experiment**

Six adult New Zealand white rabbits were randomly divided into three groups (2, 4, and 6 months; n=2 in each group). Anesthesia was induced by ear vein injection. After shaving and disinfection of the hind limbs, a cylindrical bone defect (diameter 6 mm, depth 10 mm) was drilled on the left distal femoral condyle (Figure 4-1). FA:Yb^{3+}/Ho^{3+} powder was implanted into the defects and harvested with surrounding tissue at 2, 4, and 6 months after implantation. The harvested samples were fixed in 10 % formalin, dehydrated through gradient ethanol, then embedded with PMMA and cut into sections of 3 μm in thickness, subsequently stained with Masson's staining and observed under a light microscope

(TE2000-U, Nikon, Japan). The fluorescent images were collected via inverted fluorescence microscope (Ti-U, Nikon, Japan) and two-photo confocal microscope (LSM 780 NLO, ZEISS, Germany).

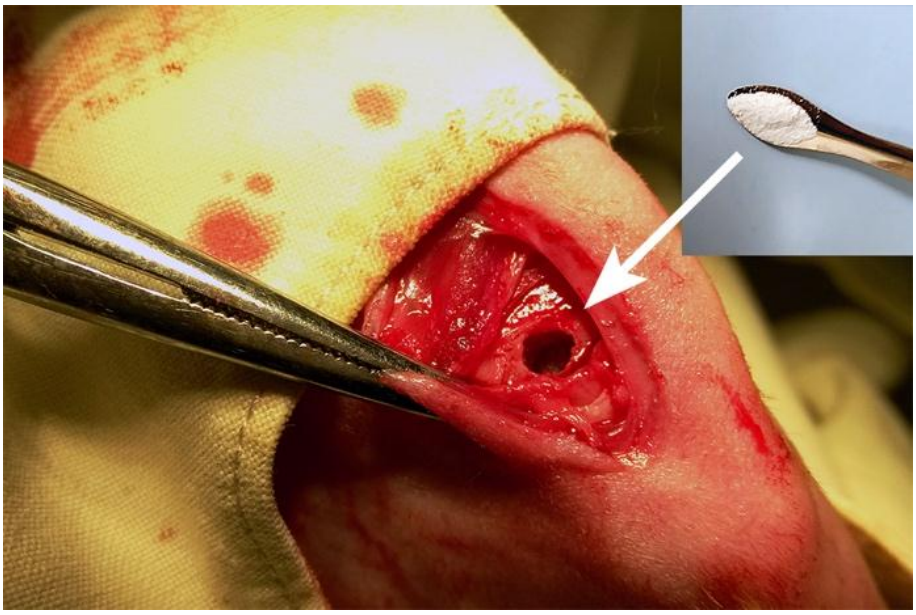

Figure 4-1 The created bone defect of rabbit distal femoral condyle, and implantation of FA:Yb^{3+}/Ho^{3+} powder into the defect.

Statistical analysis

All results are expressed as mean ± standard deviation (SD). Statistical comparisons between groups were analyzed by using one-way ANOVA test. A value of $p < 0.05$ was considered to be statistically significant.

Results and discussion

The morphologies of hydrothermally synthesized Yb^{3+}/Ho^{3+} co-doped FA and HA particles were shown in Figure 4-2. After hydrothermal synthesis, the precipitates presented rod-like morphology when surfactant was used in the synthesis [Figure 4-2 (A, B)]. By adjusting the content of NaOH or pH, nanospheres (Figure 4-2C) or nanowire (Figure 4-2D) could be obtained. After activation at 700 °C for 2 h, the rod nanoparticles

showed slight shrinkage than the as-prepared ones, like the insets in Figure 4-2 (A, B). It has been found that fluorapatite has a more stable crystal structure than hydroxyapatite. Different nano-morphology may adapt to different applications. The elaborate nanorods may suit for cell imaging, the nanospheres could be microcarrier of drug or protein molecules, the nanowire could be used to make biocomposite. The nanorods may be also suitable for *in vivo* animal experiments as tracking fillers of bone defect or composite scaffolds, besides for possible detection and diagnostic kit. We found that these apatite nanoparticles could present both green and red upconversion fluorescence when excited by 980 nm NIR light, which may provide more choice in biomedical applications.

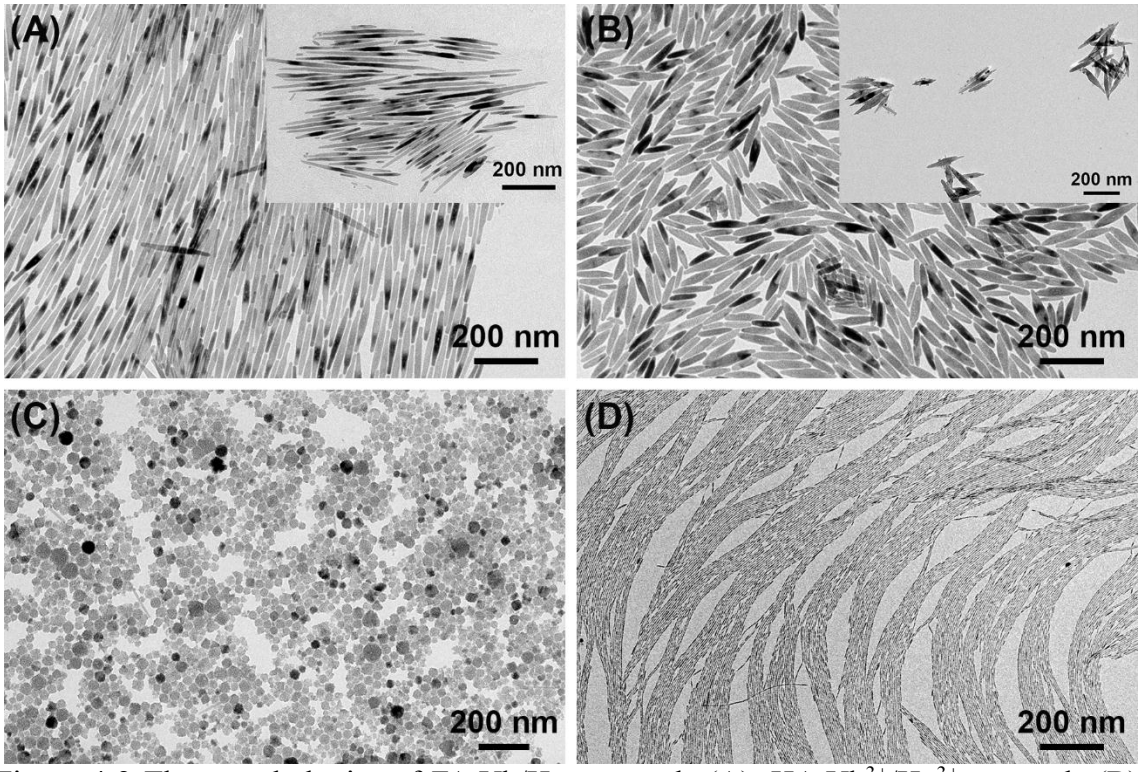

Figure 4-2 The morphologies of FA:Yb/Ho nanorods (A), HA:Yb^{3+}/Ho^{3+} nanorods (B), FA:Yb/Ho nanospheres (C) and FA:Yb/Ho nanowire (D) after hydrothermal synthesis. Insets in (A) and (B) are the images after thermal activation.

To detect and compare upconversion signals, the upconversion emissions of activated Yb^{3+}/Ho^{3+} co-doped FA and HA particles with varying dopant concentrations were

investigated under 980 nm excitation with 400 mW pump power. Figure 4-3 showed the upconversion luminescence spectra of FA:Yb^{3+}/Ho^{3+} and HA:Yb^{3+}/Ho^{3+} with a fixed Yb^{3+} concentration at 10 mol% and varying Ho^{3+} concentrations from 0.5 to 3 mol%. The green and red emissions centered at 543 and 654 nm originated from the transitions of Ho^{3+}: $^5F_4$, $^5S_2$ - $^5I_8$ and $^5F_5$ - $^5I_8$, respectively. By altering the doping concentration of Ho^{3+} ions, we observed different upconversion emission behaviors. For the Yb^{3+}/Ho^{3+} co-doped FA matrix, the green emission had a much higher intensity than the red emission, and the peak width of green emission was relatively narrower (Figure 4-3A). The FA:10Yb^{3+}/0.5Ho^{3+} sample showed the strongest emission intensity, with both the green and red emissions decreasing with increasing Ho^{3+} ion concentration from 0.5 to 3 mol%. This may have been a result of the concentration-dependent quenching. Others have also reported a similar phenomenon.[110, 111] Figure 4-3B showed the upconversion emission spectra of HA:Yb^{3+}/Ho^{3+}, in which the peak intensity of red emission was dominant and the HA:10Yb^{3+}/1Ho^{3+} sample had the highest emission intensity. Both red and green emissions had the same variation trend when the concentration of Ho^{3+} ions was increased. The intensity first increased with Ho^{3+} ion concentration from 0.5 to 1 mol%, and then decreased with Ho^{3+} ion concentration from 2 to 3 mol%. Ho^{3+} upconversion emission was attributed to the energy transfer upconversion (ETU) process. Under 980 nm near-infrared excitation, the Yb^{3+} ions (sensitizer) absorbed energy from the 980 nm laser and transferred it to adjacent Ho^{3+} ions (activator) that emitted two-photon upconversion luminescence[109, 112] (Figure 4-3C). Figure 4-3D illustrated the upconversion emission under 980 nm excitation with varying pump power from 300 to 1,500 mW for the FA:10Yb^{3+}/0.5Ho^{3+} sample. The intensities of green and red emissions were enhanced by increasing pump

power. These changes were more rapid and evident during the initial period of increasing pump power.

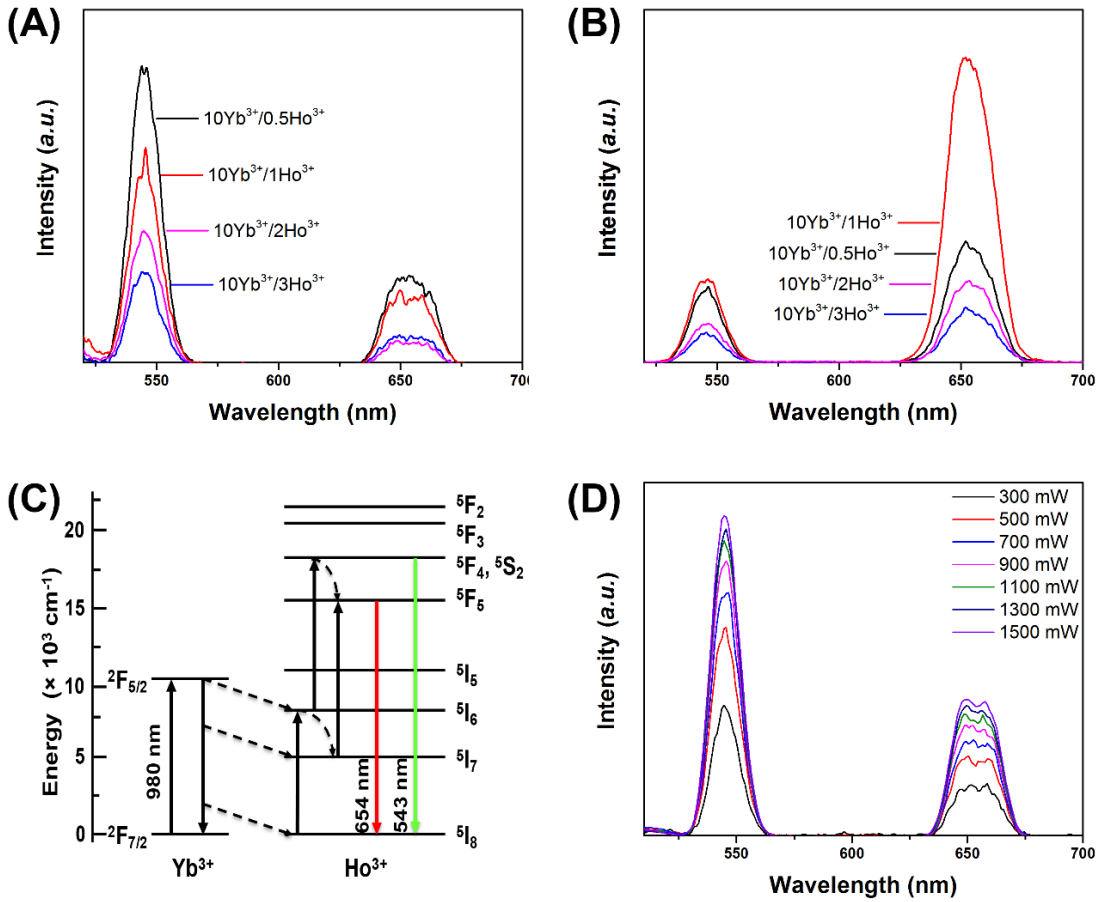

Figure 4-3 Upconversion luminescence spectra of (A) FA:Yb^{3+}/Ho^{3+} and (B) HA:Yb^{3+}/Ho^{3+} with various dopant concentrations. (C) Upconversion energy transfer diagram of Yb^{3+} and Ho^{3+} ions under 980 nm excitation. (D) Upconversion spectra of the FA:10Yb^{3+}/0.5Ho^{3+} with varying pump power.

The difference in green and red emission behavior between FA:Yb^{3+}/Ho^{3+} and HA:Yb^{3+}/Ho^{3+} should be dependent on their lattice structure and composition,[113] as well as the distance-related efficiency of energy transfer from Yb^{3+} to Ho^{3+} ions.[113] For upconversion materials, doping usually involves an insulating host matrix embedded with trace amount of lanthanides in its lattice. FA and HA have the same hexagonal crystal structure belonging to the $P6_3/m$ (176) space group, so the difference in dominant emissions

between the FA (green) and HA (red) matrix may have been caused by the difference of F^- ions and OH^- ions. When the F^- ion substitutes for the OH^- ion with smaller ionic radius and stronger electronegativity, the hexagonal apatite crystal structure becomes more compact and binding energy increases.[108] In addition, F^- ions have a much lower photon energy compared to OH^- ions, which are able to quench fluorescence due to their high vibration frequency.[80, 81] The stronger red upconversion is often reported by other researchers with a relatively high concentration of Ho^{3+} ions and is attributed to cross-relaxation among different levels of Ho^{3+} ions, which may inhibit green upconversion.[114, 115] Small changes in crystal structure can also affect the efficiency of Yb^{3+} to Ho^{3+} energy transfer and result in the alteration of green and red emissions. Figure 4-4 showed a lattice model for Yb^{3+}/Ho^{3+} co-doped FA and HA crystal cells along the fluorine channel and hydroxyl channel of the hexagonal apatite structure. In the hexagonal apatite structure, there are two calcium triangles surrounding the two F^- ions or two OH^- ions. When one Yb^{3+} ion and one Ho^{3+} ion substitute for two Ca^{2+} ions in a calcium triangle, a Ca^{2+} vacancy occurs for the charge balance, and the ion substitutions will change the lattice parameters. Compared to the lattice parameters of the pure FA sample (a = b = 9.449 Å, c = 6.883 Å), the FA:10Yb^{3+}/0.5Ho^{3+} sample showed smaller lattice parameters of a = b = 9.382 Å, c = 6.882 Å. After activation at 700 °C, the parameters further reduce to 9.361 Å and 6.868 Å. The decrease in unit cell dimension suggests more stable crystal structure and stronger ion interaction in the co-doped apatite lattice, which can enhance the distance-related efficiency of energy transfer from Yb^{3+} to Ho^{3+}. Without thermal activation, the Yb^{3+}/Ho^{3+} co-doped apatite samples appeared unstable and demonstrated weak upconversion luminescence under 980 nm excitation.

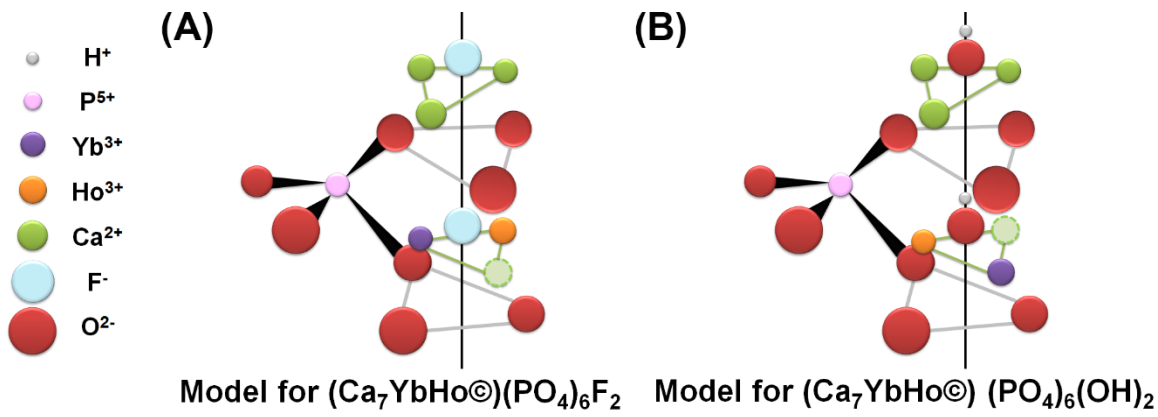

Figure 4-4 Lattice model for FA:Yb^{3+}/Ho^{3+} (A) and HA:Yb^{3+}/Ho^{3+} (B) crystal cells along the fluorine channel and hydroxyl channel of hexagonal apatite structure; the broken circle represents the Ca^{2+} vacancy.

Fluorescent images of FA:10Yb^{3+}/0.5Ho^{3+} and HA:10Yb^{3+}/1Ho^{3+} were obtained by inverted fluorescence microscope (Ti-U, Nikon, Japan) under 980 nm near-infrared excitation (Figure 4-5). The green image looked more clear and distinguishable, but the red image was blurrier, although the brightness of green and red glows was both strong. Therefore, we selected and concentrated on the FA:10Yb^{3+}/0.5Ho^{3+} sample for further animal experiments due to its dominant green emission and optimal image resolution, and nanorod morphology. In addition, a dominant upconversion green emission could avoid the auto-fluorescence of tissues and green fluorescence of some biomedical polymer matrix under excitation of UV and blue lights, as well as distinguish itself from the red color of stained bone tissue on histological sections when comparing superimposed upconversion and light microscopy images.

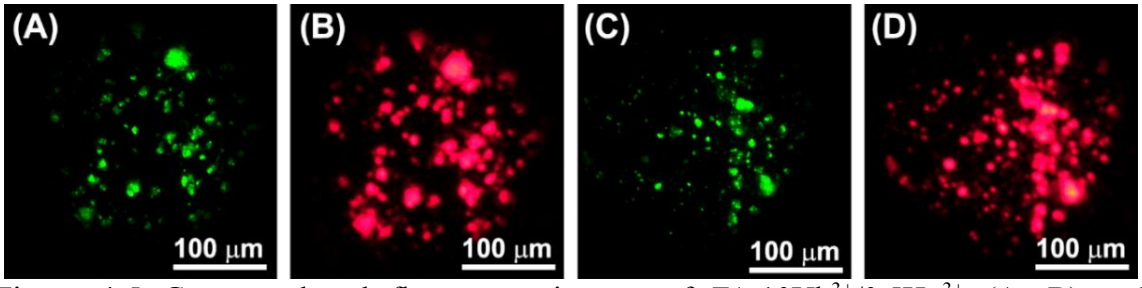

Figure 4-5 Green and red fluorescent images of FA:10Yb^{3+}/0.5Ho^{3+} (A, B) and HA:10Yb^{3+}/1Ho^{3+} (C, D).

The crystal structure and morphology of the FA:10Yb^{3+}/0.5Ho^{3+} sample were examined using XRD, FT-IR, HRTEM and EDS. Figure 4-6A showed the XRD pattern of the FA:10Yb^{3+}/0.5Ho^{3+} sample, in which the diffraction peaks match well with the classical hexagonal phase of FA ($Ca_{10}(PO_4)_6F_2$, ICDD 77-0120). The sharp characteristic peaks at 25.9°, 32°, 33.1°, 40.1°, 46.7°, and 49.7° corresponded directly to the (002), (211), (300), (212), (222), and (213) lattice planes, respectively. There were no impurity diffraction peaks or phases in the XRD pattern, indicating that the Yb^{3+} and Ho^{3+} ions had been successfully incorporated into the FA crystal lattice. The FT-IR spectrum in Figure 4-6B illustrated the asymmetrical stretching vibration peak at 1042 cm^{-1} and the bending vibration peaks at 606 and 576 cm^{-1} corresponding to PO_4^{3-} groups of the FA crystal structure. Figure 4-6C displayed a HRTEM image with presence of 2D lattice fringes on single rod-like FA:Yb^{3+}/Ho^{3+} crystal, the interplanar spacing of (002) lattice plane is 0.347 nm, which refers the crystal prefers to grow along the (002) direction. The inset SAED pattern shows (002) and (211) planes, which is in well agreement with that observed in XRD pattern. Both Yb^{3+} and Ho^{3+} ions were present in the EDS element mapping (Figure 4-6D) of the crystal, demonstrating the successful incorporation of Yb^{3+} and Ho^{3+} ions into the FA crystal structure.

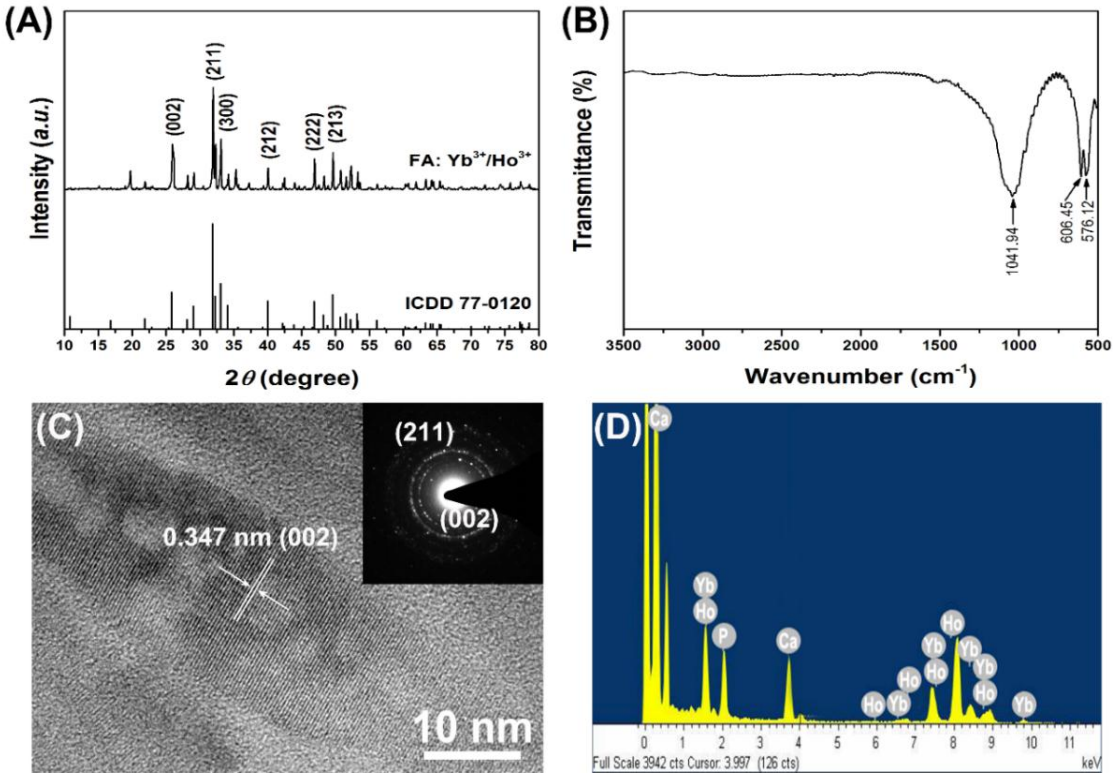

Figure 4-6 XRD pattern (A), FT-IR spectrum (B), HRTEM image (C, inset is the SAED pattern), and EDS element mapping (D) of the FA:10Yb^{3+}/0.5Ho^{3+} sample.

To evaluate the cytocompatibility of FA:10Yb^{3+}/0.5Ho^{3+}, we used the MTT assay to investigate cell viability of MG63 cells cultured with various concentrations of FA:10Yb^{3+}/0.5Ho^{3+} nanoparticles for 1, 4, 7, and 11 days. As shown in Figure 4-7A, the Yb^{3+}/Ho^{3+} co-doped FA nanoparticles had no negative influence on the viability of MG63 cells at concentrations of 100, 200, and 400 μg/mL. The cells proliferated with culture time; on day 1 and day 4, all experimental groups and the control showed similar optical density (OD) values. On days 7 and 11, the experimental groups still exhibited normal growth status with OD values slightly lower than the control ($^*p < 0.05$). We also demonstrated that the upconversion nanoparticles could penetrate into cells after grafting dextran onto the surface of the nanoparticles.[101] Figure 4-7B illustrated the green luminescence of cells incubated with 100 μg/mL of FA:Yb^{3+}/Ho^{3+} nanoparticles obtained by a two-photon

confocal microscopy under 980 nm excitation. The cell morphology and cytoplasm could be clearly observed through the stable upconversion luminescence. The low absorption of cell components and tissues under NIR excitation indicated additional advantages in avoiding photodamage and auto-fluorescence for the *in vivo* study.[116]

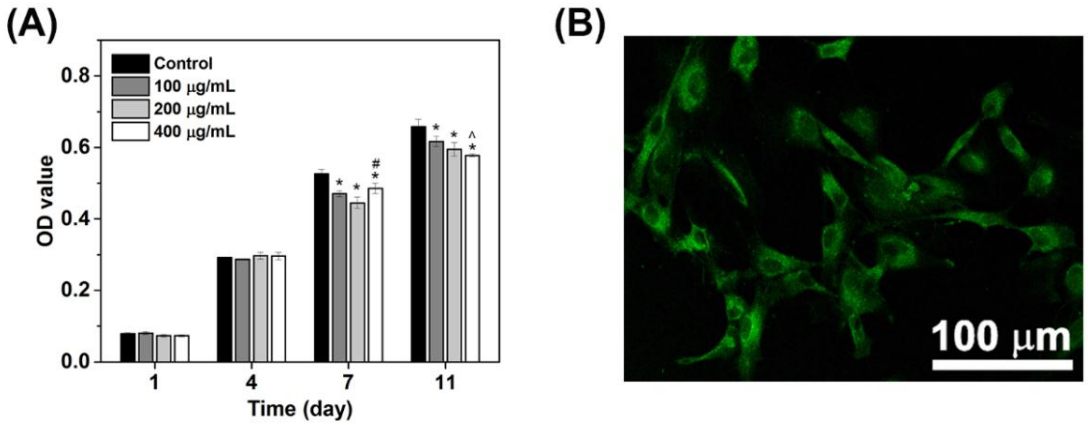

Figure 4-7 Cell viability of MG63 cells cultured with different dosages of FA:10Yb^{3+}/0.5Ho^{3+} nanoparticles for 1, 4, 7, and 11 days (A), error bars represent mean ± SD from triplicate experiments, $p < 0.05$ (* vs. control, ^ vs. 100 μg/mL, # vs. 200 μg/mL). Two-photon confocal luminescence images of MG63 cells treated with 100 μg/mL FA:Yb^{3+}/Ho^{3+} nanoparticles (B), with green luminescence collected at 500-550 nm.

Figure 4-8 showed a light microscopy image of bone tissue without staining (A), and the corresponding fluorescent images under various excitations. The bone tissue presented weak blue, green, and red (B-D) auto-fluorescence under excitation of UV, blue, and green lights, respectively. There was no luminescence or auto-fluorescence under the excitation of 980 nm near-infrared laser light (E).

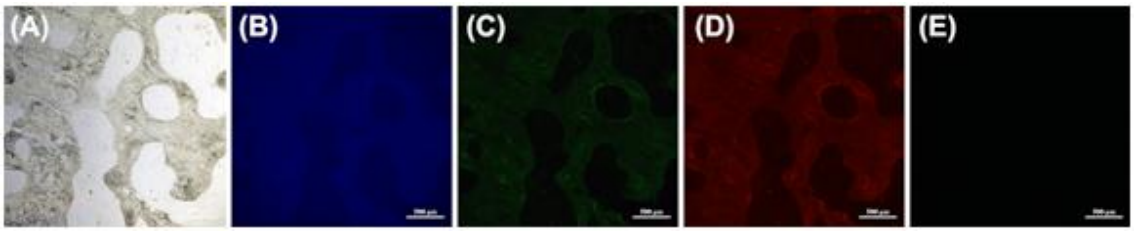

Figure 4-8 The light microscopy image (A) of bone tissue without staining and corresponding fluorescent images under excitation of UV (B), blue (C), green (D), and 980 nm near-infrared (E) lights, scale bar = 500 μm.

After Masson's staining, matured bone tissue and growing bone tissue on histological sections were indicated in blue color and red color, respectively, under observation of light microscopy (Figure 4-9A). From the stained section, it is hard to distinguish clearly the implanted material, the material distribution, and the material-tissue interrelation. Figure 4-9B was the overlap image of the tissue light image and the upconversion green fluorescent image of the implanted FA:10Yb^{3+}/0.5Ho^{3+} particles under 980 nm NIR excitation, which clearly showed the particles' distribution. In the experiment, we found by accident that the Masson's stained bone tissue could also emit red fluorescence under 561 nm laser excitation of the confocal microscope (red image in Figure 4-9C). This allows for simultaneous viewing with the upconversion fluorescent image (green in Figure 4-9(B, C)) of the FA:10Yb^{3+}/0.5Ho^{3+} particles under 980 nm NIR laser excitation on the same confocal microscope. The superposition of the two fluorescent images endows us with an alternative mode to show distinctly the material-tissue interrelation. It lets us to know the detailed distribution and their interrelation of implanted material and bone tissue. Especially, the image superposition can clearly distinguish the difference of region 'a' and 'c' in Figure 4-9A. It could be seen from Figure 4-9 (B, C) that the bone tissue could bond with the FA:10Yb^{3+}/0.5Ho^{3+} particles and grew into the interval space between these particles; in other words, the apatite particles have interspersed and integrated in the interpenetrating network of new bone. The black area in Figure 4-9C corresponded to the empty region (or glass substrate) in the region 'c' of Figure 4-9A.

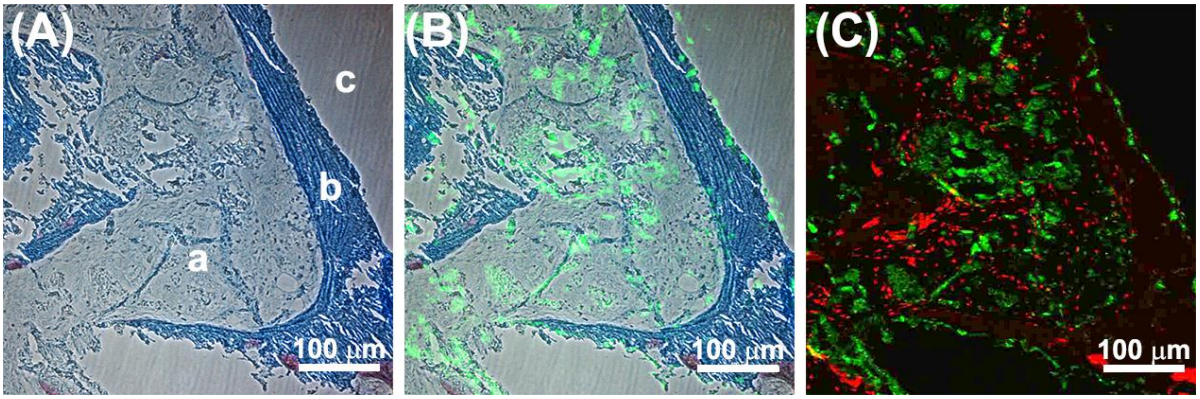

Figure 4-9 (A) light image of Masson's stained new bone tissue by light microscope after 6-month implantation; (B) the overlap image of the tissue light image and the upconversion green fluorescent image of implanted FA:10Yb^{3+}/0.5Ho^{3+} particles; (C) the superposition of red fluorescent image of new bone tissue under 561 nm laser excitation and the green fluorescent image of FA:10Yb^{3+}/0.5Ho^{3+} particles under 980 nm NIR laser excitation.

By using both red and green fluorescence, we investigated bone growth with the implantation time. Figure 4-10 showed the superposition of red (new bone tissue) and green (FA:10Yb^{3+}/0.5Ho^{3+} particles) fluorescent images on histological sections of samples harvested at 2, 4, and 6 months. The green upconversion fluorescence was excited at 980 nm and collected at 500-550 nm, while the red luminescence was excited at 561 nm and collected at 570-695 nm. At 2 months, most of the implanted FA: 10Yb^{3+}/0.5Ho^{3+} particles were still in agglomerated states and surrounded by newly formed bone tissue, leading to green bulk with surrounding red tissue, as shown by the white arrow in Figure 4-10A. At 4 months, the particles started to spread out, and new bone tissue had formed in between particles (Figure 4-10B). At 6 months, the implanted FA:10Yb^{3+}/0.5Ho^{3+} particles had fully integrated with the new bone (Figure 4-10C).

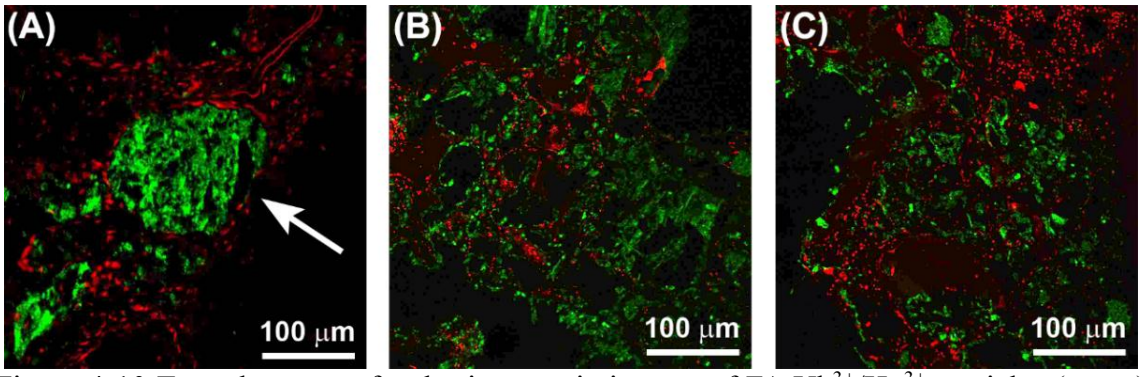

Figure 4-10 Two-photon confocal microscopic images of FA:Yb^{3+}/Ho^{3+} particles (green) and new bone tissue (red) for samples harvested at 2 (A), 4 (B), and 6 (C) months after implantation.

It is difficult to clearly differentiate newly formed bone tissue from the implanted biomaterial by traditional Masson's or H.E. staining. Our results show that the introduction of FA:Yb^{3+}/Ho^{3+} particles with upconversion luminescence allowed for observation and tracking of the distribution of both the new bone tissue and the implanted material during the osteogenesis (Figure 4-9B and Figure 4-10). This could previously not be observed by traditional optical microscopy (such as region 'c' in Figure 4-9A). In addition, upconversion luminescence could label the implanted material and scaffold, avoiding interference from auto-fluorescence of tissues. It is known that apatite particles that possess the capacity of bonding to bone tissue have been incorporated into degradable polymer matrices such as PLGA and PCL, to construct composite scaffolds for bone regeneration. This study suggests that FA:Yb^{3+}/Ho^{3+} particles with stable, bright, and long-lasting upconversion luminescence can be incorporated into these degradable polymers to track the scaffolds, the scaffold-tissue interface and respective distribution, and the degraded scaffold fragments *in vivo*. Thus, lanthanide Yb^{3+} and Ho^{3+} co-doped apatite materials and the superposition method of fluorescence imaging have many potential applications in biomedical tracking.

Conclusion

FA:Yb^{3+}/Ho^{3+} and HA:Yb^{3+}/Ho^{3+} upconversion particles with various dopant concentrations were successfully fabricated by hydrothermal synthesis and thermal activation. These particles can emit both green and red upconversion luminescence when excited by 980 nm near-infrared laser. The upconversion luminescence ascribes to the energy transfer from Yb^{3+} ions (sensitizers) to adjacent Ho^{3+} ions (activators), which emit two-photon upconversion luminescence: $^5F_4$, $^5S_2$ - $^5I_8$ and $^5F_5$ - $^5I_8$ transitions. We show for the first time that it is possible to simultaneously distinguish the implanted material from the newly formed bone tissue, and track their respective distribution and integration during osteogenesis *in vivo* by using the prepared Yb^{3+}/Ho^{3+} co-doped apatite particles as a novel bioactive labeling agent. *In vitro* and *in vivo* experiments demonstrate that the upconversion particles have good biocompatibility, bone-bonding capacity, and superiority in fluorescent tracking. Both the materials and methods presented in this research pave a new way for long term tracking and monitoring of implanted biomaterials during osteogenesis *in vivo*.

CHAPTER 5 CONCLUSION AND OUTLOOK

In this thesis we design and prepare new fluorescent probes based on rare earth doped apatite nanoparticles with DC or UC fluorescence to track the differentiation and osteogenic processes of BMSCs and bony tissues, including selecting right doping matrix and dopants, evaluating the system and tracking the cells and implanted biomaterials.

In chapter 2, Terbium (Tb) doped fluorapatite (FA:Tb) and hydroxyapatite (HA:Tb) crystals are hydrothermally synthesized. Their composition, crystal structure, fluorescent and biological properties are investigated. The Tb-doped crystals are in nanoscale and present a uniform slender morphology. The doping of Tb^{3+} ions can promote the preferential growth of apatite nanocrystals along the *c*-axis (002) direction, and cause the binding energy to increase for FA:Tb^{3+} crystals or decrease for HA:Tb^{3+} crystals. The FA crystal structure tends to combine more Tb^{3+} ions than HA crystal structure, and shows a stronger green fluorescence. Four Tb-doping lattice models along apatite hexagonal structure are proposed, revealing a necessity for coexistent substitution mechanism of $(Ca_7Tb_2©)(PO_4)_6(OH)_2$, $(Ca_6Tb_2Na_2)(PO_4)_6(OH)_2$, $(Ca_9Tb)(PO_4)_6(OH)O$, and $(Ca_8TbNa)(PO_4)_6(OH)_2$. Labelled BMSCs were shown to reproducibly exhibit osteogenic differentiation potential in real-time PCR and ELISA assays. Long-term *in vivo* cell-tracking experiments confirmed the stability of dextran-coated Tb-FA nanorods. The Tb-doped apatite nanocrystals exhibit bright fluorescence, good cytocompatibility and excellent cell imaging capacity, providing feasibility for imaging and tracking of cells with multilineage differentiation.

In chapter 3, rare-earth Yb^{3+} and Ho^{3+} co-doped fluorapatite (FA:Yb^{3+}/Ho^{3+}) crystals

were prepared by hydrothermal synthesis, and their structure, upconversion property and cell behavior were investigated. The crystals with a size of 16 by 286 nm have a hexagonal crystal structure of classic FA and a Ca/Yb/Ho molar ratio of 100/16/2.1. Several reasonable Yb^{3+}/Ho^{3+} embedding lattice models along the fluorine channel of FA crystal cell were proposed for the first time, such as models for $(Ca_7YbHo©)(PO_4)_6F_2$, or $(Ca_6YbHoNa_2)(PO_4)_6F_2$. The activated FA:$Yb^{3+}/Ho^{3+}$ crystals were found to exhibit distinct upconversion fluorescence. The 543 and 654 nm signals in emission spectrum could be assigned, respectively, to $^5F_4$ ($^5S_2$) - $^5I_8$ and $^5F_5$ - $^5I_8$ transitions of holmium, via 980 nm near-infrared excitation and energy transfer of ytterbium. After surface coating with hydrophilic dextran, the crystals displayed clear fluorescent cell imaging. We determined the chondrogenic differentiation potential of the labeled $BMSCs^{GFP}$ using real-time RT-PCR analysis, histological assessment and immunohistochemistry. The continuous luminescence was detected after 12 weeks post transplantation from the FA: Yb^{3+}/Ho^{3+} upconversion crystals, while the GFP signal was significantly decreased after this time. The prepared novel FA:Yb^{3+}/Ho^{3+} upconversion fluorescent crystals have a good prospect for biomedical applications.

In chapter 4, lanthanide Yb^{3+} and Ho^{3+} co-doped fluorapatite (FA:Yb^{3+}/Ho^{3+}) and hydroxyapatite (HA:Yb^{3+}/Ho^{3+}) nanoparticles with varying dopant concentrations were prepared by hydrothermal synthesis and thermal activation. Their upconversion emissions were investigated via fluorescence spectrometer. Histological sections of the harvested *in vivo* samples were treated with Masson's staining and imaged by inverted fluorescence microscopy and laser confocal microscopy. The results showed that controllable green and red upconversion emissions could be generated under 980 nm near-infrared excitation; the

FA:Yb^{3+}/Ho^{3+} nanoparticles resulted in a superior green luminescence, while HA:Yb^{3+}/Ho^{3+} dominated in red emission. The difference in green and red emission behavior between FA:Yb^{3+}/Ho^{3+} and HA:Yb^{3+}/Ho^{3+} was dependent on their lattice structure and composition. Two possible lattice models were proposed by us for Yb^{3+}/Ho^{3+} co-doped HA and FA along the hydroxyl channel and fluorine channel of the apatite crystal structure. The upconversion apatite nanoparticles were used for the first time to clearly distinguish the implanted material from bone tissue, showing their distribution and integration. The superposition of images endows us with a better mode to show distinctly the material-tissue interrelation. The overlap of stained bone tissue light image and apatite upconversion fluorescent image, and the superposition of their fluorescent images indicated that new bone tissue could grow into the interval space between the apatite particles and fully integrate with these particles. Without the upconversion fluorescent image, it is almost impossible to observe many details only from the light image of the stained histological section. The upconversion apatite particles and image superposition method provide a novel strategy for long-term discriminable fluorescence tracking of implanted materials or scaffolds.

Although these rare-earth doped apatite nanoparticles have been prepared and investigated by us for cell imaging and biomaterial tracking, it is still a pioneering research. A lot of further works have to be done to expand its biomedical applications. For example, the uniform downconversion apatite nanocrystals should be suitable for study on their morphology change during *in vitro* cytophagy and *in vivo* degradation. The upconversion apatite nanoparticles should be used for real-time *in vivo* tracking. Moreover, we can coat the surface of these nanoapatites with different functional groups for different targeting

purpose. A problem for upconversion real-time *in vivo* tracking might be that the emitting distance of the upconversion fluorescence is still limited in the body, though the NIR excitation light can penetrate deeper in the tissues. At the moment, engineers have tried their best to overcome this shortcoming by developing higher sensitive CCD detector to receive the weak fluorescence from deeper tissues. In addition to the progress mentioned in the thesis, the long term *in vivo* effect of the rare-earth doped apatite nanoparticles also needs more systematic investigation.

APPENDIX AN AMORPHOUS SILICA-COATED PCL ELECTROSPUN FIBERS WITH A CORE-SHEATH STRUCTURE FOR BIOACTIVE AND BIODEGRADABLE SCAFFOLDS

This work was done during May, 2014 – May, 2015 at Atlanta under the guidance of Prof. Younan Xia, the Wallace H. Coulter Department of Biomedical Engineering, Georgia Institute of Technology and Emory University; and cooperated with Justin Lipner and Dr. Stavros Thomopoulos, Department of Biomedical Engineering, Washington University, St. Louis, USA.

Introduction

Bone has the capacity for regeneration and self-healing in response to small bony injury via continuous remodeling.[117, 118] However, skeletal reconstruction of large bone defects created by trauma, infection, tumor resection and skeletal abnormalities is beyond the normal potential for self-healing,[119] and presents a difficult challenge to cure effectively.[120] Usually porous scaffolds are required to assist the reconstruction of these irreversible tissue defects. In recent years, the concept of bone tissue engineering has gained great importance as a promising strategy for bone regeneration, of which scaffolds become one of the three crucial factors besides cells and growth factors.[121] Among metallic, ceramic and polymeric scaffolds, the polymeric matrix attracts more attention in mimicking the extracellular matrix (ECM), endowing biodegradability, and providing low modulus comparable to living tissues. A considerable number of natural and synthetic degradable polymers are currently used as scaffolds, involving collagen,[122] cellulose,[123] elastin,[124] silk fibroin,[125] poly(lactic-co-glycolic acid) (PLGA), and poly (ε-caprolactone)

(PCL) etc.,[126] in which PLGA and PCL play an active role in mechanical properties, biodegradability, and matrix shaping.[127, 128]

The design of scaffold architecture using different fabrication techniques also plays an important role in determining scaffold properties. For polymer scaffolds, the usual fabrication methods include gas forming, freeze-drying, salt leaching and replica methods.[129, 130] Electrospinning is a notably simple and versatile technique to generate continuous fibers or fiber mat with controllable fiber diameter, mat porosity, and surface morphology,[128, 131] which can serve as an ideal candidate scaffold for tissue regeneration. To construct ECM-like scaffolds with large surface area and high porosity, both PLGA and PCL microfibers have been fabricated by electrospinning. PLGA copolymer is a kind of hydrophobic and brittle polyester with high mechanical strength. Although its degradation rate can be adjusted by the ratio of lactic acid to glycolic acid, the degradation of PLGA is still too fast or come too sudden to control, due to its amorphous structure and high hydrolysis rate.[132] The *in vivo* degradation by-products are lactic acid and glycolic acid, which often cause stimulation to cells and tissues, and result in aseptic inflammation.[133] PCL is a hydrophobic and semi-crystalline polyester with high mechanical strength and high toughness.[127, 132] The degradation products are H_2O and CO_2, which enable PCL polymer to have better biocompatibility. However, the *in vivo* degradation process of PCL matrix is usually much slower than that of PLGA matrix.[130]

Ceramic or inorganic coatings on implants can provide surface bioactivity to bond with bone tissue.[134, 135] A polymer scaffold for bone repair or reconstruction is also required to possess surface bone-bonding bioactivity in addition to providing a porous structure for bone ingrowth. Hydroxyapatite (HA)[136] and silica-based bioglass[137] have

been used as surface bioactive coatings. Bone tissue can form a strong link with the HA surface or the Si-rich layer. It may be an ideal scaffold that owns a 3D meshy structure constructed with degradable microfibers and degradable surface bioactive coatings. With the progress of bone regeneration and reconstruction, the degradable fibers and coatings can be gradually absorbed by living body and finally substituted by newly formed bone tissue. An amorphous coating should degrade more quickly than a crystalline coating during bone reconstruction.

Comparing PCL with PLGA, both the surface of pure PCL fibers and the surface of pure PLGA fibers are hydrophobic, lack of high affinity to cell adhesion and attachment, and short of the capacity for bonding with bone tissue. PCL and its degradation products show better biocompatibility, but the degradation of PCL matrix is relatively slow, and requires longer time than that of PLGA. The aim of this research is to form a nanoscale silica coating on the PCL microfiber scaffolds to provide a capacity for bonding with bone tissue, and to adjust the mechanical properties. The effect of coating time and round (cycle index) on the thickness of silica coating, and the effect of coating time on the toughness, yield strength and elastic modulus of the coated fiber scaffolds were investigated. The cytocompatibility of the scaffolds was also evaluated via culture with cells.

Materials and methods

Materials.

Poly (ε-caprolactone) (PCL, Mw ≈ 70, 000-90, 000), hexafluoroisopropanol (HFP), ethanol, tetraethyl orthosilicate (TEOS), ammonium hydroxide (NH_4OH), and dichloromethane (DCM) were obtained from Sigma-Aldrich, USA. All of the chemicals were used as received.

Fabrication of the PCL electrospun fibers and fiber mat.

PCL was dissolved in HFP at a concentration of 10%. The solution was loaded in a syringe attached with a 22-gauge needle and electrospun onto a rotating mandrel collector at a speed of 2 m/s. The injection rate was 0.5 mL/h, the working distance was about 20 cm, and a voltage of 18 KV was applied. The fiber mat (fiber scaffold) was formed and collected from rotating mandrel collector after continuous uniaxially aligned stacking of the PCL electrospun fibers (Figure A1).

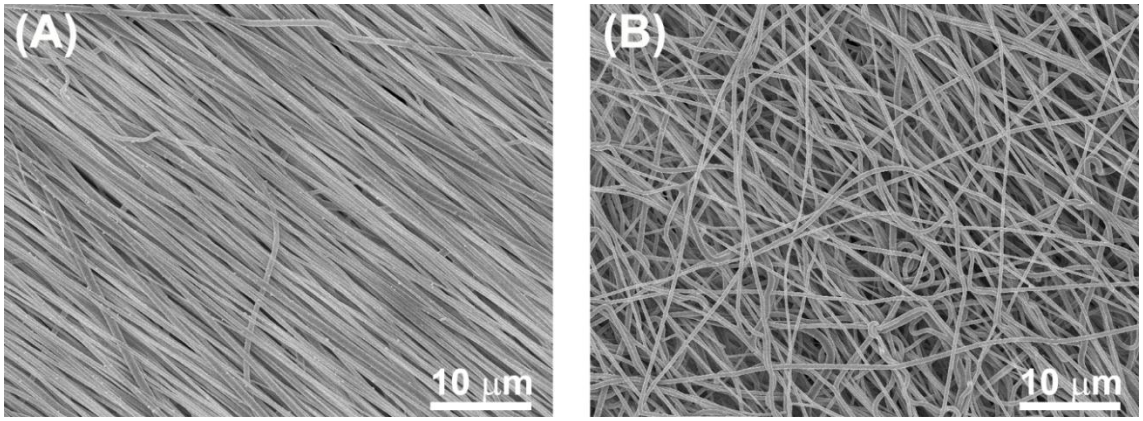

Figure A1 Appearance of the uniaxially aligned fiber mat (A) compared with the random oriented fiber mat (B).

Silica coating on the PCL fiber scaffolds.

The electrospun PCL fiber scaffold supported on a wire frame was firstly plasma treated (PE50, Unitronics, NV) for 2 min for both sides to make the fiber scaffold hydrophilic according to our previous work.[138] Then the fiber scaffold was soaked into the solvent mixture of water (5 mL) and ethanol (30 mL) followed by the addition of TEOS (0.05 mL) and ammonium hydroxide (1 mL). The resulting solution was stirred at 300 rpm at 21 °C for 4, 6, and 10 h, respectively. The product was washed with water three times and then freezing dried. The 4 h process was repeated for two and four rounds (cycle index)

to fabricate the 2x and 4x samples.

Characterization.

Scanning Electron Microscopy (SEM, Hitachi SU8230) was used to visualize the fibers and the coating morphologies. The samples were sputter coated with Au-Pd for 60 s, and an accelerating voltage of 2 kV was used. The energy dispersive spectroscopy (EDS) was also used for analyses of coating elements. Thickness of the coating was measured by a Transmission Electron Microscopy (TEM, Hitachi HT7700) with an accelerating voltage of 120 kV. Some TEM samples were prepared by dissolving the PCL core with DCM and then dispersed in ethanol. X-ray diffraction (XRD, X' Pert PRO Alpha-1) was used to investigate the crystal structure of PCL matrix and the coating mineral phase after dissolving the PCL core, over a 2θ degree range of 10 to 60 degree using Cu Kα radiation (λ = 1.5406 Å). Fourier transform infrared spectra (FT-IR, Varian 640-IR) were conducted using KBr as the sample holder. The resolution in the spectrum collection was set at 1 cm^{-1}, and the scanning range was set from 4000 cm^{-1} to 400 cm^{-1}.

Mechanical testing of the fiber scaffolds.

Samples coated for 0, 4, 6 and 10 h and 2x, 4x rounds were tested under tension to determine their mechanical properties. The fiber scaffold was cut into strips of about 14 x 3 x 0.08 mm^3 in size for uniaxial tensile mechanical testing (n = 5 per group). The scaffold thickness was measured using a laser micrometer (LK-081, Keyence), and the width was measured from calibrated digital images. The cross-sectional area was calculated as the width multiplied by the thickness. A texture-rich pattern of alizarin red dye was sprayed onto the test strip for optical deformation tracking. Mechanical testing was then performed under uniaxial tension at a strain rate of ~0.5% per second using a materials testing system

(ElectoPuls, Instron). Testing was recorded by video at 1360 x 1024 resolution at 2.5 fps using a CCD camera (DP70, Olympus). The engineering stress was calculated as the load divided by the initial cross-sectional area, and the finite strain was determined from image data using custom Matlab (Mathworks, Natick MA) routines. The modulus was calculated as the slope of the linear region of the stress-strain curve. The toughness was calculated as the area under the stress-strain curve, reflecting the energy absorption of the material.

Cell culture on the scaffolds.

Mouse embryo-derived, fibroblastic cells (NIH/3T3; ATCC CRL-1658) were cultured in Dulbecco's Modified Eagle's Medium (DMEM, Invitrogen, Grand Island, NY), supplemented with 10% fetal bovine serum (FBS, Invitrogen), and 1% antibiotics (containing penicillin and streptomycin, Invitrogen). The medium was changed every other day, and the cultures were incubated at 37 °C in a humidified atmosphere containing 5% CO_2.

Cell viability assay.

The cell proliferation was measured by the 3-(4,5-dimethylthiazol-2-yl)-2,5-diphenyltetrazolium bromide (MTT) assay (Invitrogen). MTT is a tetrazole that is metabolized and reduced to purple formazan in live cells. Coated PCL scaffolds (8 × 10 mm^2 area per piece, n = 3) were fixed onto microscope cover glass, and placed in wells of a 24-well plate (Corning). The samples were sterilized in 70% ethanol overnight, and then washed with phosphate buffer saline (PBS) three times. Cells were seeded in each well and cultured in 1 mL culture medium (DMEM). After culturing for 1, 2, and 3 days, 40 μL of MTT solution in PBS (5 mg/mL) was added to each well and incubated at 37 °C for 4 h. The scaffolds were then detached from the glass and transferred to a 96-well plate

(Corning), and 300 μL of DMSO was added to each well to completely dissolve formazan crystals throughout the scaffolds. The scaffolds were finally removed. Absorbance was measured at 570 nm using a spectrophotometer (Infinite F200 Pro, TECAN, Morrisville, NC). All final data were normalized to the actual area of each scaffold.

Statistical analysis

The data are presented in the form of mean ± standard deviation. Statistical comparisons were made using Student's t-test and statistically significant was attained at $p < 0.05$.

Results and Discussion

In our hypothesis, both the coating time and the coating cycle may affect the thickness of the mineralized coating on scaffold fibers, which could further affect the mechanical properties and surface bioactivity. Figure A2 shows SEM images and TEM insets of the uniform nano-coating on PCL microfibers. The average diameter of the uniaxially aligned PCL microfibers is about 0.45 μm (Figure A2A). Figure A2B-D and upper right TEM insets exhibit the morphology and thickness of coatings formed in ethanol-TEOS solution for 4, 6, and 10 h, respectively. The thickness rises rapidly from 28 nm (4h) to 40 nm (6h), then gradually to 50 nm at 10 h, and the coatings attach tightly on the surface of PCL microfibers without interface gap. It can be seen that the coating thickness can be controlled not only by adjusting the coating time but also by the cycle index. Figure A2E-F show that the thickness also grows with rounds (2x and 4x, 4 h per round), giving a value of about 60 nm and 90 nm, respectively. Both the coating time and cycle index are proportional to the thickness of the surface coating. And we find that the silica coating grows faster at first two rounds than extending time; the coating of two rounds (2x, 8 h in total) group is 10 nm

thicker than that of 10 h group (Figure A3), however the coating thickness at second two rounds (from 8 h to 16 h) increases only 30 nm, much slower than the first two rounds. It should be noted that the fiber diameter also shows a slight increase with the coating time (see TEM insets in Figure A2B-D), swelling of PCL fibers may occur in the ethanol-TEOS solution during the coating process.

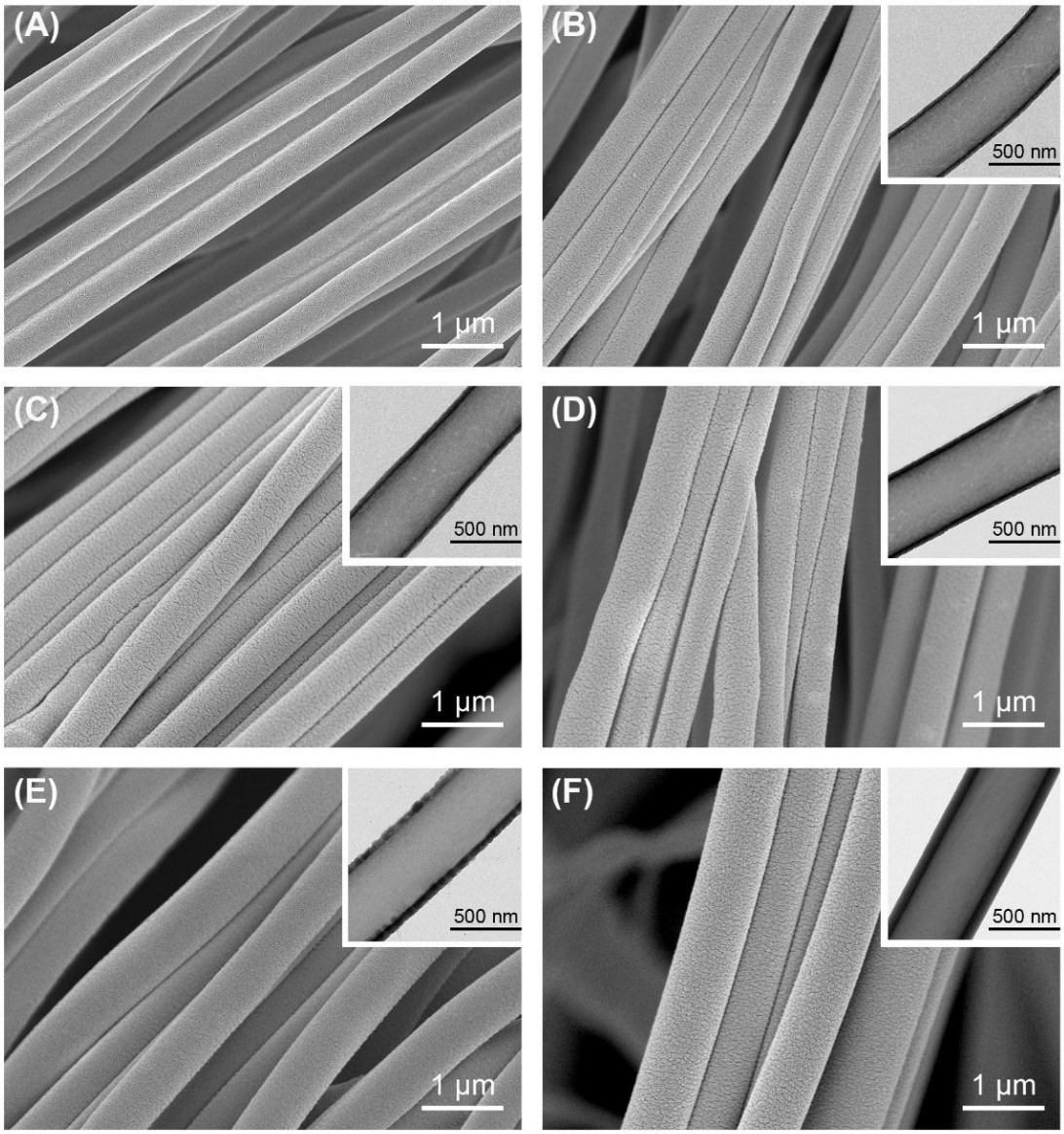

Figure A2 SEM images of PCL electrospun microfibers coated for (A) 0 h, (B) 4 h, (C) 6 h, (D) 10 h, (E) 2 rounds (8 h), and (F) 4 rounds (16h). Insets are the corresponding TEM images of the coating.

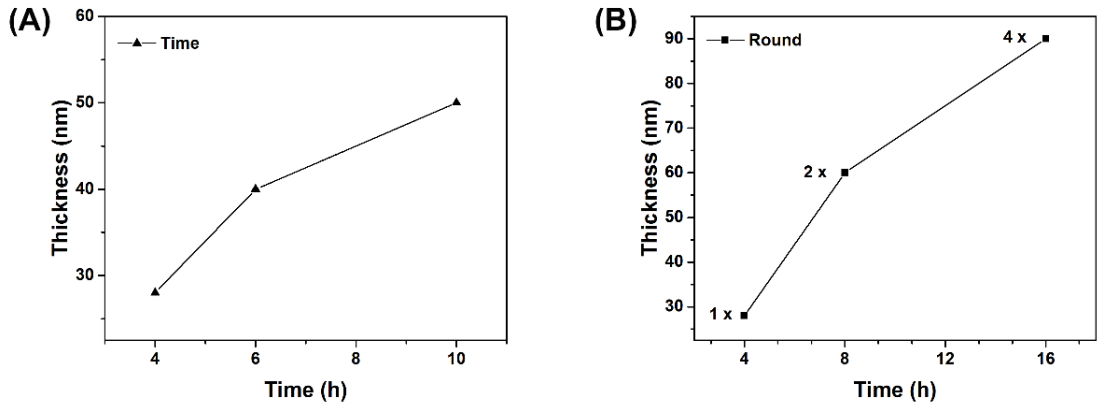

Figure A3 Dependence of the coating thickness on the coating time (A) and coating rounds (B).

Plasma treatment plays a vital role in the formation of uniform mineralized coating via transferring the hydrophobic fiber surface to hydrophilic one with opened carboxylic groups.[138] Without plasma treatment, fine coating is hard to form (Figure A4A). We found that a uniform and close-grained coating could be obtained with proper plasma treatment time (2 min, Figure A4C). When the plasma treatment time is too short (30 S) or too long (10 min), uneven coatings are formed (Figure A4 (B, D)). It indicates that the plasma treatment on the surface of PCL fibers will affect the deposition of coating ions or groups on the fiber surface via changing the surface hydrophilicity and nucleation site. If the plasma treatment time is too short, only partially hydrophilic surface and small number of nucleation sites can be formed, leading to microsphere aggregation (Figure A4B); if the plasma time is too long, the fiber surface could be destroyed and cracked, resulting in a cracking coating (Figure A4D).

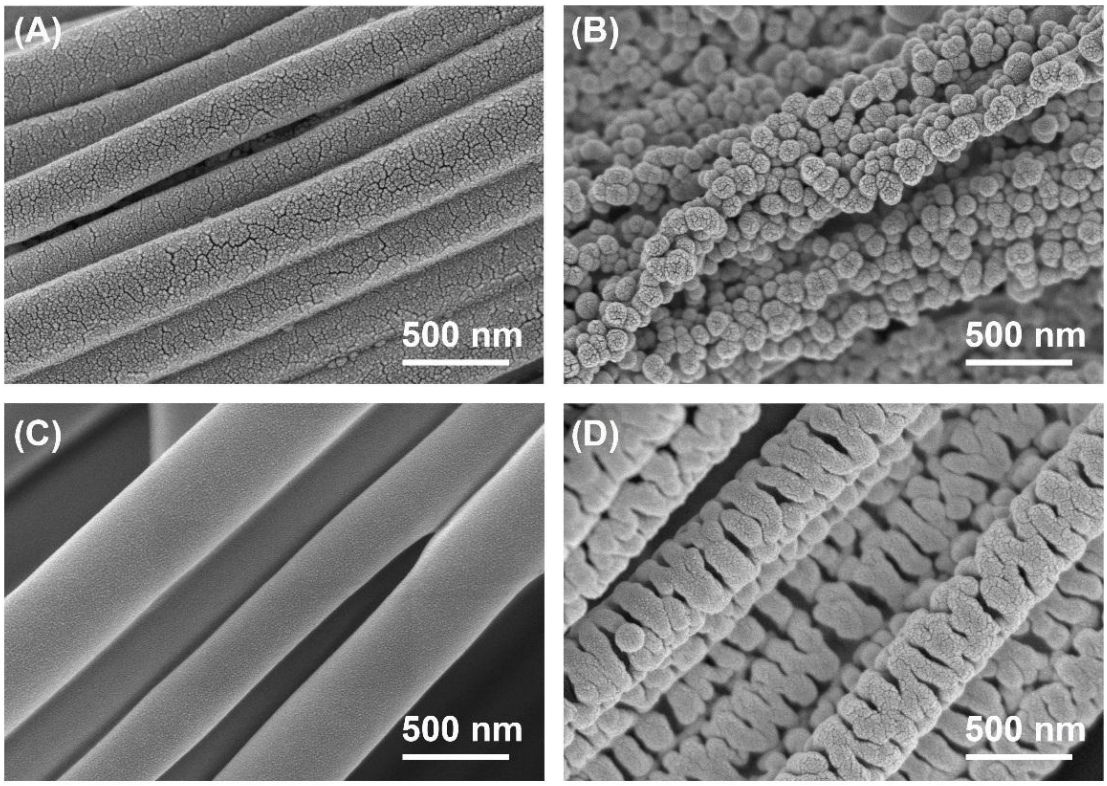

Figure A4 Mineralized coating on the PCL microfibers after plasma treatment for (A) 0, (B) 0.5, (C) 2, and (D) 10 min.

To understand the composition and structure, XRD patterns, FTIR spectra, SEM image and EDS mapping were utilized for analysis of the PCL fibers and surface coatings. The XRD pattern in Figure A5A(a) illustrates that the PCL microfibers have a semi-crystalline structure with characteristic peaks at 21.4° and 23.6°, corresponding to the orthorhombic planes (110 and 200) of PCL. Figure A5A(b) shows the pattern of silica coating with a diffusive peak at about 20-30°, which demonstrates a typical structure of amorphous hydrated silica. In Figure A5B(a) of PCL fibers, the peaks at 2945 cm^{-1}, 2867 cm^{-1}, and at 1238 cm^{-1}, 1171 cm^{-1} belong to the asymmetric and symmetric stretching vibration of -CH_2 and -C-O-C, respectively. The absorption peak at 1731 cm^{-1} is related to the carbonyl stretching. Figure A5B(b) displays three characteristic peaks of silica.[23] The absorption peaks at 1097 cm^{-1} and 803 cm^{-1} correspond to the stretching vibration of Si-

OH and Si-O, respectively. The peak at 470 cm^{-1} corresponds to bending vibration of the Si–O–Si bond. In addition, 3443 cm^{-1} ascribes to the O-H stretching vibration of physically adsorbed water, 1632 cm^{-1} is bending vibration absorption of physically adsorbed water. An SEM image of silica coating sheath is shown in Figure A5C after dissolving the PCL fiber core by DCM. The coating exhibits continuous and uniform tubular structure with a certain wall thickness. EDS analysis on the coating wall in Figure A5D shows the presence of Si and O elements. The results indicate that the mineralized coating is composed of amorphous silica.

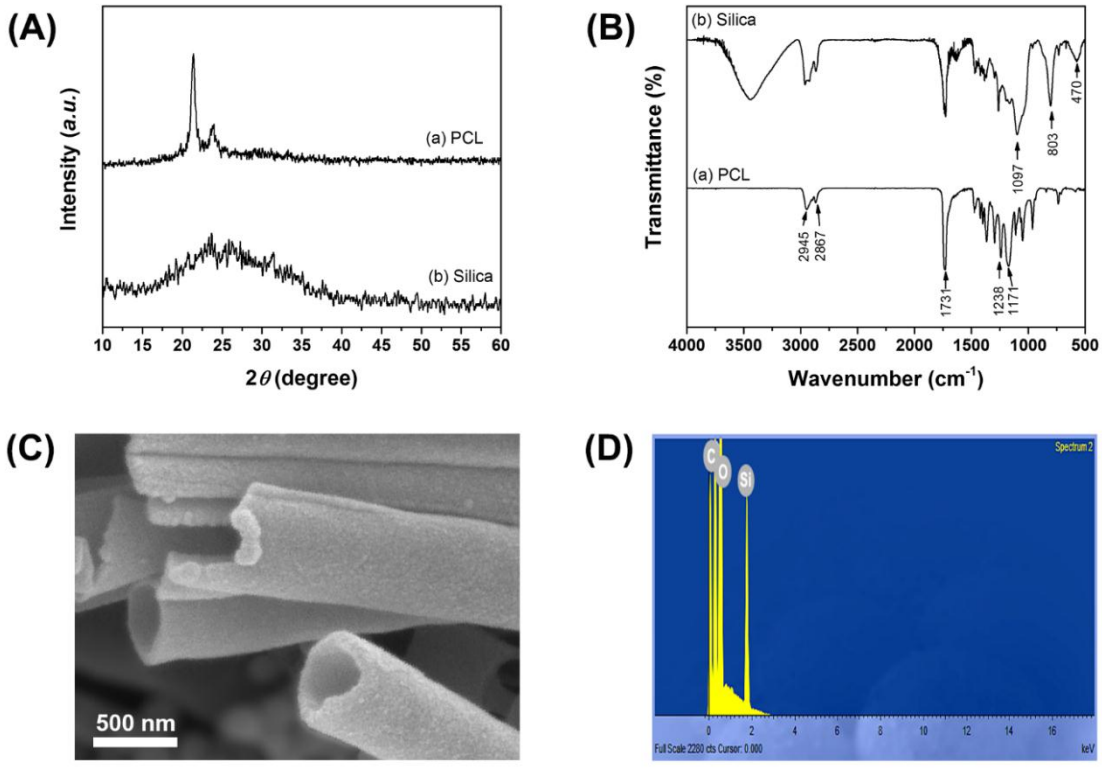

Figure A5 XRD patterns (A) of the PCL microfibers (a) and silica coating (b), FT-IR spectra (B) of the PCL microfibers (a) and silica coating (b), SEM image (C) of silica coating sheath after dissolving PCL fiber core, and EDS mapping of coating elements.

Figure A6 gives a schematic diagram to illustrate the formation mechanism of silica coating. After plasma treatment, the surface carboxyl (COO-) groups of PCL fibers react

with the hydrolyzate (Si-OH) groups of TOES to form C-O-Si bonds, then the condensations of neighbor Si-OH groups produce abundant Si-O-Si bonds, on which nucleation comes up, accompanied by continuous growth of silica coating.

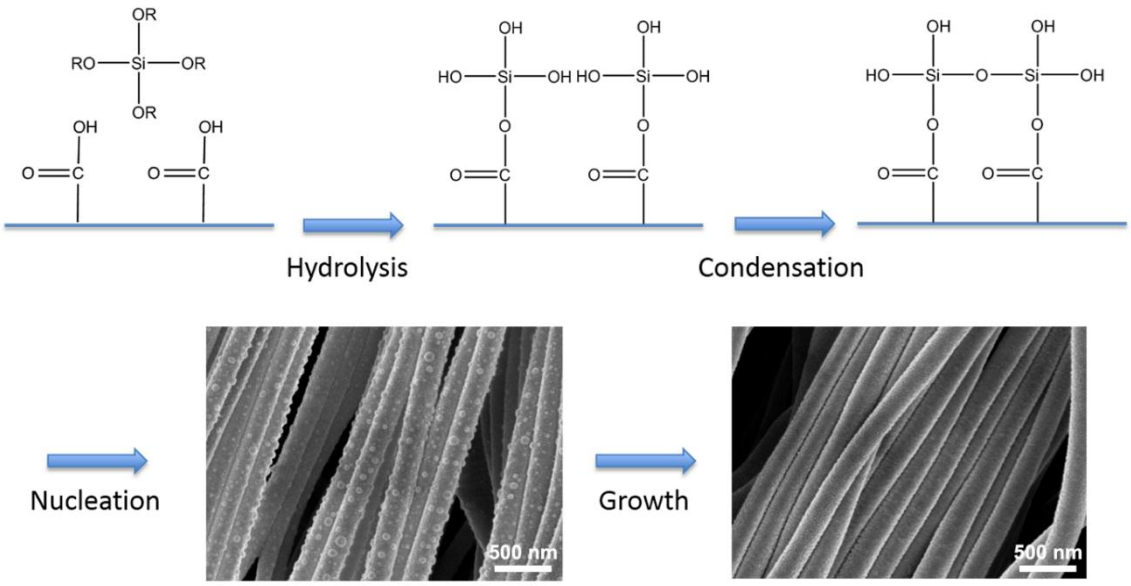

Figure A6 Schematic diagram showing the mechanism of the formation of silica coating.

As we know, both the HA coating and the silica coating have good cell affinity and a capacity for bonding with bone tissue.[135-137] Comparing with the HA coating on microfibers,[138] the silica coating (Figure A2) looks more uniform and close-grained, especially it shows an amorphous structure that could be helpful for faster degradation and absorption with new tissue formation over time. When mineralized coating is formed on polymer fibers, usually the elastic modulus of the coated fibers or fiber scaffolds will increase with the coating formation. However, a reverse phenomenon appears in this experiment. As shown in Figure A7A, the silica-coated PCL fiber scaffolds with a coating time 4, 6, and 10 h have a smaller modulus than the pure PCL fiber scaffold (0 h). Among the three coated fiber scaffolds, the 6 h sample shows a highest value of modulus. For the toughness, all the three coated scaffolds have a bigger value of toughness than that of pure

PCL scaffold. The scaffold coated for 6 h holds the highest toughness (Figure A7B) and yield stress (i.e. strength, in Figure A7C). This reveals that the 6 h silica-coated PCL fiber scaffold may possess superior interface quality between the coating and PCL fibers.

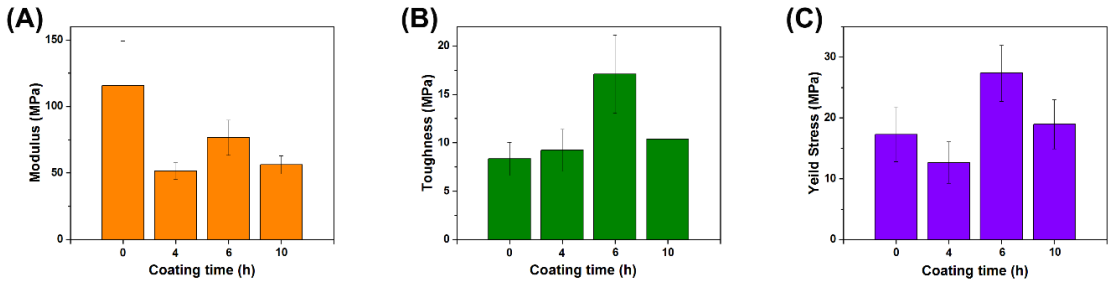

Figure A7 Young's modulus, fracture toughness and yield stress of PCL fiber scaffolds before and after silica coating for different time.

The reduction of modulus after coating should be closely related to the swelling of PCL fibers in the ethanol-TEOS solution. It has been reported that the ethanol solution could cause swelling of the polyester fiber scaffold and largely decrease the fiber modulus.[139] Also, ethanol has sometimes been used for the swelling test of PCL matrix. From the TEM insets of Figure A2(B-D), the small increase in fiber diameter with the coating time could demonstrate the swelling occurrence of the PCL fiber scaffolds in the ethanol-TEOS solution during the coating process, and even after freeze-drying, the swelling of PCL matrix cannot be completely reversed. This should be the main reason for the modulus reduction of the coated PCL fiber scaffolds. Swelling or structure relaxation of PCL matrix happens chiefly in the non-crystalline region, because the crystallinity of the crystalline region does not show significant difference (Figure A8A). As we know, the degradation of PCL matrix mainly starts from its amorphous region. The swelling or chain relaxation of PCL amorphous region could facilitate the water penetration of body fluid into the PCL matrix, then speeding up the hydrolysis of ester linkage and the *in vivo* degradability of PCL matrix.

After coating for 4 h, the modulus reduction is mainly caused by the ethanol induced net swelling and chain relaxation of PCL matrix, although the silica coating can increase the modulus to some extent. At 6 hours, the effect of rapidly increased coating thickness on the increase of modulus exceeds the effect of gradual swelling of PCL fibers on the modulus reduction, resulting synthetically in the rise of the modulus. For 10 hours of coating, the subsequent incrassation of coating may lead to increased interfacial stress between the silica coating and PCL fibers, thus reducing again the modulus of the coated fiber scaffold. When the coating becomes too thick, the interfacial stress between coating and fiber, and internal stress of coating itself will even cause interface debonding and coating cracking (Figure A8B). Therefore, control of the coating time or coating thickness is crucial for obtaining high quality coating interface.

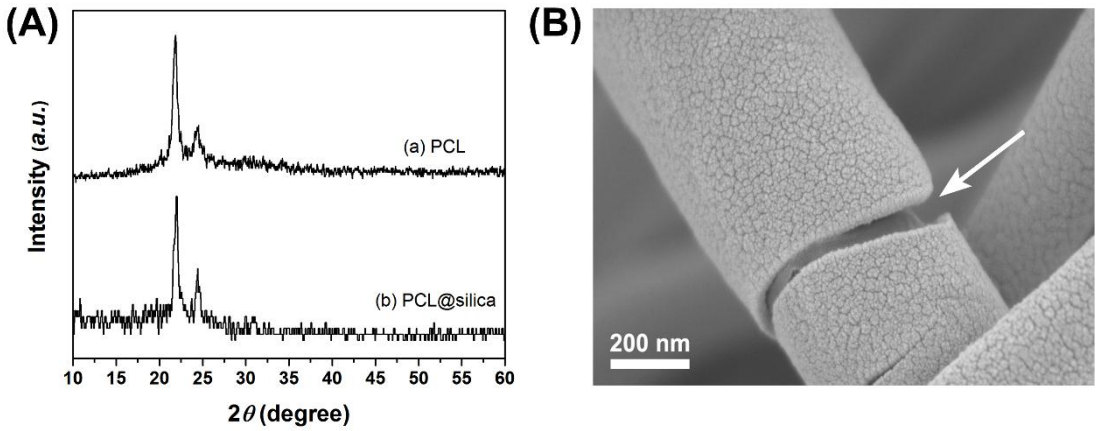

Figure A8 XRD patterns (A) of the pure PCL fibers and the silica-coated PCL fibers, and TEM image (B) showing the loosened interface between PCL fiber and thick silica coating.

MTT assay was conducted to study the response of cells to the PCL fiber scaffolds with different silica coating thickness. Figure A9 shows that the cell proliferation rate of different coating thickness groups increases markedly and continuously with the culture time. And all experimental groups show a higher proliferation rate than the pure PCL

control (P <0.05). On Day 3, they still exhibit a normal growth status. It indicates that the silica coating affords superior cellular affinity, and the silica-coated PCL fiber scaffolds have good cytocompatibility, suitable for further *in vivo* investigation.

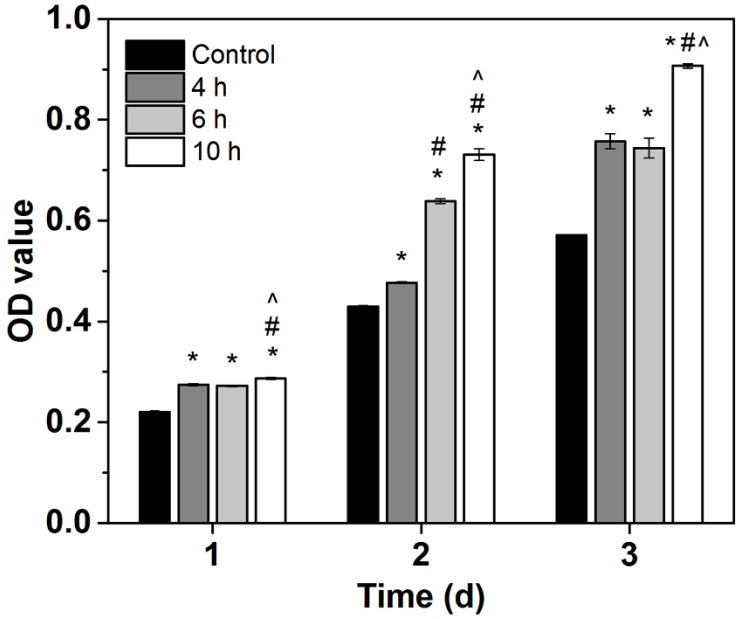

Figure A9 MTT assay for cell proliferation cultured with PCL fiber scaffolds of different thickness for 1, 2, and 3 days, error bars represent mean ± SD from triplicate experiments, $p < 0.05$ (* vs. control, # vs. 4 h, ^ vs. 6 h).

It is important to optimize a scaffold by adjusting each component. A bone scaffold must have good biocompatibility and must be osteoconductive. Both the PCL matrix and the silica coating are biologically safe for living body, and the silica coating provides an osteoconductive capacity to bond with bone tissue. Biodegradability is another crucial factor for scaffolds.[140] The scaffold should serve to provide a temporary structure, which subsequently degrades in tandem with new tissue formation over time.[141] PCL polymer is a biodegradable material with relatively slow degradation rate.[130] Reduction in size and modulus would be an effective way to accelerate its degradability. The use of ultrafine electrospun PCL fibers and the reduced elastic modulus in this experiment would be

beneficial to an achievement of a faster biodegradation. The use of amorphous silica coating is also helpful for more rapid *in vivo* degradation comparing with the crystalline coatings. In addition, when used for bonding to bone at the tendon-to-bone insertion site, the aligned ECM-like fiber structure, and the improved toughness and strength of the silica-coated PCL fibrous scaffold have also an advantage to allow effective energy transmission along the long axis of adjacent muscle loading, except the uniaxially aligned electrospun PCL microfibers can mimic the highly anisotropic structure of a tendon tissue. Consequently, the core-sheath PCL fiber scaffold with nanoscale amorphous silica coating will present a promising prospect for future biomedical applications.

Conclusion

In this experiment, nanoscale amorphous silica coating with a uniform and close-grained structure has been successfully formed on the ultrafine PCL electrospun fibers via a mixed solution of ethanol and tetraethyl orthosilicate. The coating technique leads to an increase in fracture toughness and yield strength, and a reduction in the elastic modulus of the coated fibrous scaffolds. Swelling of PCL matrix by ethanol should be responsible for the modulus reduction. The ultrafine fibers and the reduced scaffold modulus would be beneficial to an achievement of a faster biodegradation regarding to the slow *in vivo* degradation rate of PCL matrix. The silica coating can provide a capacity for the fiber scaffolds to bond with bone tissue. In summary, we have demonstrated a simple and versatile method to produce amorphous silica coating on PCL microfibers, and to adjust the nano-coating thickness and mechanical properties. The *in vivo* investigation of this scaffold is expected to carry out to present its promising prospect in biomedical applications.

Acknowledgment

This work was supported in part by a grant from the National Institutes of Health (R01 AR060820) and startup funds from the Georgia Institute of Technology (to Y.X.). Part of the characterization work was performed at the Institute for Electronics and Nanotechnology.

REFERENCES

[1] Hench LL, Best SM. Chapter I.2.4 - Ceramics, Glasses, and Glass-Ceramics: Basic Principles A2 - Lemons, Buddy D. RatnerAllan S. HoffmanFrederick J. SchoenJack E. Biomaterials Science (Third Edition): Academic Press; 2013. p. 128-151.

[2] Marten A, Fratzl P, Paris O, Zaslansky P. On the mineral in collagen of human crown dentine. Biomaterials. 2010; 31 (20): 5479-5490.

[3] Jiang H, Zuo Y, Zou Q, Wang H, Du J, Li Y, et al. Biomimetic spiral-cylindrical scaffold based on hybrid chitosan/cellulose/nano-hydroxyapatite membrane for bone regeneration. ACS Applied Materials & Interfaces. 2013; 5 (22): 12036-12044.

[4] Chen H, Sun K, Tang Z, Law RV, Mansfield JF, Clarkson BH. Synthesis of Fluorapatite Nanorods and Nanowires by Direct Precipitation from Solution. Crystal Growth and Design. 2006; 6 (6): 1504-1508.

[5] Dvir T, Timko BP, Kohane DS, Langer R. Nanotechnological strategies for engineering complex tissues. Nature nanotechnology. 2011; 6 (1): 13-22.

[6] Place ES, Evans ND, Stevens MM. Complexity in biomaterials for tissue engineering. Nature Materials. 2009; 8 (6): 457-470.

[7] Appel AA, Anastasio MA, Larson JC, Brey EM. Imaging challenges in biomaterials and tissue engineering. Biomaterials. 2013; 34 (28): 6615-6630.

[8] Roldan JC, Detsch R, Schaefer S, Chang E, Kelantan M, Waiss W, et al. Bone formation and degradation of a highly porous biphasic calcium phosphate ceramic in presence of BMP-7, VEGF and mesenchymal stem cells in an ectopic mouse model. Journal of Cranio-Maxillo-Facial Surgery. 2010; 38 (6): 423-430.

[9] Liebi M, Georgiadis M, Menzel A, Schneider P, Kohlbrecher J, Bunk O, et al. Nanostructure surveys of macroscopic specimens by small-angle scattering tensor tomography. Nature. 2015; 527 (7578): 349-352.

[10] Syamchand SS, Sony G. Multifunctional hydroxyapatite nanoparticles for drug delivery and multimodal molecular imaging. Microchimica Acta. 2015; 182 (9-10): 1567-1589.

[11] Georgakoudi I, Rice WL, Hronik-Tupaj M, Kaplan DL. Optical spectroscopy and imaging for the noninvasive evaluation of engineered tissues. Tissue Engineering Part B: Reviews. 2008; 14 (4): 321-340.

[12] Nam SY, Ricles LM, Suggs LJ, Emelianov SY. Imaging strategies for tissue engineering applications. Tissue Engineering Part B: Reviews. 2015; 21 (1): 88-102.

[13] Ntziachristos V. Going deeper than microscopy: the optical imaging frontier in biology. Nature Methods. 2010; 7 (8): 603-614.

[14] Ward A, Quinn KP, Bellas E, Georgakoudi I, Kaplan DL. Noninvasive metabolic imaging of engineered 3D human adipose tissue in a perfusion bioreactor. PloS One. 2013; 8 (2): e55696.

[15] Chang T, Zimmerley MS, Quinn KP, Lamarre-Jouenne I, Kaplan DL, Beaurepaire E, et al. Non-invasive monitoring of cell metabolism and lipid production in 3D engineered human adipose tissues using label-free multiphoton microscopy. Biomaterials. 2013; 34 (34): 8607-8616.

[16] Yang Q, Peng J, Guo Q, Huang J, Zhang L, Yao J, et al. A cartilage ECM-derived 3-D porous acellular matrix scaffold for in vivo cartilage tissue engineering with PKH26-labeled chondrogenic bone marrow-derived mesenchymal stem cells. Biomaterials. 2008; 29 (15): 2378-2387.

[17] Cohen BE. Biological imaging: Beyond fluorescence. Nature. 2010; 467 (7314): 407-408.

[18] Bunzli JC. Lanthanide luminescence for biomedical analyses and imaging. Chemical Reviews. 2010; 110 (5): 2729-2755.

[19] Suri S, Ruan G, Winter J, Schmidt CE. Chapter I.2.19 - Microparticles and Nanoparticles A2 - Lemons, Buddy D. RatnerAllan S. HoffmanFrederick J. SchoenJack E. Biomaterials Science (Third Edition): Academic Press; 2013. p. 360-388.

[20] Chan WC, Nie S. Quantum dot bioconjugates for ultrasensitive nonisotopic detection. Science. 1998; 281 (5385): 2016-2018.

[21] Larson DR, Zipfel WR, Williams RM, Clark SW, Bruchez MP, Wise FW, et al. Water-soluble quantum dots for multiphoton fluorescence imaging in vivo. Science. 2003; 300 (5624): 1434-1436.

[22] Tian G, Gu Z, Zhou L, Yin W, Liu X, Yan L, et al. Mn^{2+} dopant-controlled synthesis of $NaYF_4$:Yb/Er upconversion nanoparticles for in vivo imaging and drug delivery. Advanced Materials. 2012; 24 (9): 1226-1231.

[23] Wang F, Han Y, Lim CS, Lu Y, Wang J, Xu J, et al. Simultaneous phase and size control of upconversion nanocrystals through lanthanide doping. Nature. 2010; 463 (7284): 1061-1065.

[24] Gai S, Li C, Yang P, Lin J. Recent progress in rare earth micro/nanocrystals: soft chemical synthesis, luminescent properties, and biomedical applications. Chemical Reviews. 2014; 114 (4): 2343-2389.

[25] Liu G. Advances in the theoretical understanding of photon upconversion in rare-earth activated nanophosphors. Chemical Society Reviews. 2015; 44 (6): 1635-1652.

[26] Liu X, Deng R, Zhang Y, Wang Y, Chang H, Huang L, et al. Probing the nature of upconversion nanocrystals: instrumentation matters. Chemical Society Reviews. 2015; 44 (6): 1479-1508.

[27] Liu X, Yan CH, Capobianco JA. Photon upconversion nanomaterials. Chemical Society Reviews. 2015; 44 (6): 1299-1301.

[28] Park YI, Lee KT, Suh YD, Hyeon T. Upconverting nanoparticles: a versatile platform for wide-field two-photon microscopy and multi-modal in vivo imaging. Chemical Society Reviews. 2015; 44 (6): 1302-1317.

[29] Bloembergen N. Solid State Infrared Quantum Counters. Physical Review Letters. 1959; 2 (3): 84-85.

[30] Idris NM, Jayakumar MK, Bansal A, Zhang Y. Upconversion nanoparticles as versatile light nanotransducers for photoactivation applications. Chemical Society Reviews. 2015; 44 (6): 1449-1478.

[31] Idris NM, Li Z, Ye L, Sim EK, Mahendran R, Ho PC, et al. Tracking transplanted cells in live animal using upconversion fluorescent nanoparticles. Biomaterials. 2009; 30 (28): 5104-5113.

[32] Liu Q, Peng J, Sun L, Li F. High-efficiency upconversion luminescent sensing and bioimaging of Hg(II) by chromophoric ruthenium complex-assembled nanophosphors. ACS Nano. 2011; 5 (10): 8040-8048.

[33] Liu Y, Zhou S, Tu D, Chen Z, Huang M, Zhu H, et al. Amine-functionalized lanthanide-doped zirconia nanoparticles: optical spectroscopy, time-resolved fluorescence resonance energy transfer biodetection, and targeted imaging. Journal of the American Chemical Society. 2012; 134 (36): 15083-15090.

[34] Jin J, Gu YJ, Man CW, Cheng J, Xu Z, Zhang Y, et al. Polymer-coated $NaYF_4$:Yb^{3+}, Er^{3+} upconversion nanoparticles for charge-dependent cellular imaging. ACS Nano. 2011; 5 (10): 7838-7847.

[35] Wang YF, Liu GY, Sun LD, Xiao JW, Zhou JC, Yan CH. Nd(3+)-sensitized upconversion nanophosphors: efficient in vivo bioimaging probes with minimized heating effect. ACS Nano. 2013; 7 (8): 7200-7206.

[36] Zhou A, Wei Y, Wu B, Chen Q, Xing D. Pyropheophorbide A and c(RGDyK) comodified chitosan-wrapped upconversion nanoparticle for targeted near-infrared photodynamic therapy. Molecular Pharmaceutics. 2012; 9 (6): 1580-1589.

[37] Osanai T, Kuroda S, Sugiyama T, Kawabori M, Ito M, Shichinohe H, et al. Therapeutic Effects of Intra-Arterial Delivery of Bone Marrow Stromal Cells in Traumatic Brain

Injury of Rats—In Vivo Cell Tracking Study by Near-Infrared Fluorescence Imaging. Neurosurgery. 2012; 70 (2): 435-444

[38] Liu H, Xu CT, Andersson-Engels S. Potential of multi-photon upconversion emissions for fluorescence diffuse optical imaging. Optics Express. 2014; 22 (15): 17782-17790.

[39] Wolfbeis OS. An overview of nanoparticles commonly used in fluorescent bioimaging. Chemical Society Reviews. 2015; 44 (14): 4743-4768.

[40] Vetrone F, Naccache R, Mahalingam V, Morgan CG, Capobianco JA. The Active-Core/Active-Shell Approach: A Strategy to Enhance the Upconversion Luminescence in Lanthanide-Doped Nanoparticles. Advanced Functional Materials. 2009; 19 (18): 2924-2929.

[41] Ghosh P, Oliva J, Rosa EDl, Haldar KK, Solis D, Patra A. Enhancement of Upconversion Emission of $LaPO_4$:Er@Yb Core−Shell Nanoparticles/Nanorods. The Journal of Physical Chemistry C. 2008; 112 (26): 9650-9658.

[42] Legeros RZ, Legeros JP. Hydroxyapatite. Bioceramics and their Clinical Applications 2008. p. 367-394.

[43] Kay MI, Young RA, Posner AS. Crystal Structure of Hydroxyapatite. Nature. 1964; 204 (4963): 1050-1052.

[44] LeGeros RZ. Calcium phosphates in oral biology and medicine. 1st ed: S. Karger; 1991.

[45] Young RA, Elliott JC. Atomic-scale bases for several properties of apatites. Archives of Oral Biology. 1966; 11 (7): 699-707.

[46] Legfros RZ, Sakae T, Bautista C, Retino M, Legeros JP. Magnesium and Carbonate in Enamel and Synthetic Apatites. Advances in Dental Research. 1996; 10 (2): 225-231.

[47] Pak CY, Adams-Huet B, Sakhaee K, Bell NH, Licata A, Johnston C, et al. Comparison of nonrandomized trials with slow-release sodium fluoride with a randomized placebo-controlled trial in postmenopausal osteoporosis. Journal of Bone and Mineral Research. 1996; 11 (2): 160-168.

[48] LeGeros RZ, Ben-Nissan B. Introduction to Synthetic and Biologic Apatites. In: Ben-Nissan B, editor. Advances in Calcium Phosphate Biomaterials. Berlin, Heidelberg: Springer Berlin Heidelberg; 2014. p. 1-17.

[49] Balamurugan A, Rebelo AH, Lemos AF, Rocha JH, Ventura JM, Ferreira JM. Suitability evaluation of sol-gel derived Si-substituted hydroxyapatite for dental and maxillofacial applications through in vitro osteoblasts response. Dental Materials. 2008; 24 (10): 1374-1380.

[50] Capuccini C, Torricelli P, Sima F, Boanini E, Ristoscu C, Bracci B, et al. Strontium-substituted hydroxyapatite coatings synthesized by pulsed-laser deposition: in vitro osteoblast and osteoclast response. Acta Biomaterialia. 2008; 4 (6): 1885-1893.

[51] Spence G, Patel N, Brooks R, Rushton N. Carbonate substituted hydroxyapatite: resorption by osteoclasts modifies the osteoblastic response. Journal of Biomedical Materials Research, Part A. 2009; 90 (1): 217-224.

[52] Liu Y, Sun Y, Cao C, Yang Y, Wu Y, Ju D, et al. Long-term biodistribution in vivo and toxicity of radioactive/magnetic hydroxyapatite nanorods. Biomaterials. 2014; 35 (10): 3348-3355.

[53] Jarcho M, Bolen CH, Thomas MB, Bobick J, Kay JF, Doremus RH. Hydroxylapatite synthesis and characterization in dense polycrystalline form. Journal of Materials Science. 1976; 11 (11): 2027-2035.

[54] Kijima T, Tsutsumi M. Preparation and Thermal Properties of Dense Polycrystalline Oxyhydroxyapatite. Journal of the American Ceramic Society. 1979; 62 (9-10): 455-460.

[55] McDowell H, Gregory TM, Brown WE. Solubility of $Ca_5\{PO_4)_3OH$ in the System $Ca(OH)_2$-H_3PO_4-H_2O at 5, 15, 25, and 37 °C. Journal of research of the National Bureau of Standards - A Physics and Chemistry. 1977; 81 A (2-3): 273-281.

[56] Wang X, Zhuang J, Peng Q, Li YD. Liquid–Solid–Solution Synthesis of Biomedical Hydroxyapatite Nanorods. Advanced Materials. 2006; 18 (15): 2031-2034.

[57] Qi C, Zhu Y-J, Ding G-J, Wu J, Chen F. Solvothermal synthesis of hydroxyapatite nanostructures with various morphologies using adenosine 5′ -monophosphate sodium salt as an organic phosphorus source. RSC Advances. 2015; 5 (5): 3792-3798.

[58] Roche KJ, Stanton KT. Precipitation of biomimetic fluorhydroxyapatite/polyacrylic acid nanostructures. Journal of Crystal Growth. 2015; 409: 80-88.

[59] Tao J, Pan H, Zeng Y, Xu X, Tang R. Roles of amorphous calcium phosphate and biological additives in the assembly of hydroxyapatite nanoparticles. The Journal of Physical Chemistry C. 2007; 111 (47): 13410-13418.

[60] Cho JS, Chan Kang Y. Advanced yolk–shell hydroxyapatite for bone graft materials: kilogram-scale production and structure-in vitro bioactivity relationship. RSC Advances. 2014; 4 (48): 25234.

[61] Hui J, Xiang G, Xu X, Zhuang J, Wang X. Monodisperse F-substituted hydroxyapatite single-crystal nanotubes with amphiphilic surface properties. Inorganic Chemistry. 2009; 48 (13): 5614-5616.

[62] Ternane R, Trabelsi-Ayedi M, Kbir-Ariguib N, Piriou B. Luminescent properties of Eu^{3+} in calcium hydroxyapatite. Journal of Luminescence. 1999; 81 (3): 165-170.

[63] Mondéjar SP, Kovtun A, Epple M. Lanthanide-doped calcium phosphate nanoparticles with high internal crystallinity and with a shell of DNA as fluorescent probes in cell experiments. Journal of Materials Chemistry. 2007; 17 (39): 4153.

[64] Zheng W, Huang P, Tu D, Ma E, Zhu H, Chen X. Lanthanide-doped upconversion nano-bioprobes: electronic structures, optical properties, and biodetection. Chemical Society Reviews. 2015; 44 (6): 1379-1415.

[65] Hui J, Wang X. Luminescent, colloidal, F-substituted, hydroxyapatite nanocrystals. Chemistry. 2011; 17 (25): 6926-6930.

[66] Yang C, Yang P, Wang W, Wang J, Zhang M, Lin J. Solvothermal synthesis and characterization of Ln (Eu^{3+}, Tb^{3+}) doped hydroxyapatite. Journal of Colloid and Interface Science. 2008; 328 (1): 203-210.

[67] Hosseini SM, Drouet C, Al-Kattan A, Navrotsky A. Energetics of lanthanide-doped calcium phosphate apatite. American Mineralogist. 2014; 99 (11-12): 2320-2327.

[68] Nam SH, Bae YM, Park YI, Kim JH, Kim HM, Choi JS, et al. Long-term real-time tracking of lanthanide ion doped upconverting nanoparticles in living cells. Angewandte Chemie, International Edition in English. 2011; 50 (27): 6093-6097.

[69] Xing Y, Rao J. Quantum dot bioconjugates for in vitro diagnostics & in vivo imaging. Cancer Biomarkers. 2008; 4 (6): 307-319.

[70] Huang CH, Ed. Coordination Chemistry of Rare Earth Complexes. Beijing: Science Press; 1997.

[71] Lai B, Feng L, Zhang J, Wang J, Su Q. Multi-phonon-assisted relaxation and Yb^{3+} sensitized bright red-dominant upconversion luminescence of Ho^{3+} in YF_3-BaF_2-$Ba(PO_3)_2$ glass. Applied Physics B. 2012; 110 (1): 101-110.

[72] Goldmacher GV, Nasser R, Lee DY, Yigit S, Rosenwasser R, Iacovitti L. Tracking transplanted bone marrow stem cells and their effects in the rat MCAO stroke model. PloS One. 2013; 8 (3): e60049.

[73] Wang F, Liu X. Multicolor tuning of lanthanide-doped nanoparticles by single wavelength excitation. Accounts of Chemical Research. 2014; 47 (4): 1378-1385.

[74] Zhou J, Liu Z, Li F. Upconversion nanophosphors for small-animal imaging. Chemical Society Reviews. 2012; 41 (3): 1323-1349.

[75] Wickleder MS. Inorganic lanthanide compounds with complex anions. Chemical Reviews. 2002; 102 (6): 2011-2088.

[76] Hench LL, Wilson J. An Introduction to Bioceramics: World Scientific; 1993.

[77] Webster TJ, Massa-Schlueter EA, Smith JL, Slamovich EB. Osteoblast response to hydroxyapatite doped with divalent and trivalent cations. Biomaterials. 2004; 25 (11): 2111-2121.

[78] Sun LJ, Ni PF, Guo DG, Fang CQ, Wang J, Yang F, et al. Synthesis and Characterization of Tb-incorporated Apatite Nano-scale Powders. Journal of Materials Science & Technology. 2012; 28 (9): 773-778.

[79] Di W, Wang X, Chen B, Lu S, Zhao X. Effect of OH- on the Luminescent Efficiency and Lifetime of Tb3+-Doped Yttrium Orthophosphate Synthesized by Solution Precipitation. The Journal of Physical Chemistry B. 2005; 109 (27): 13154-13158.

[80] Stouwdam JW, van Veggel FCJM. Near-infrared Emission of Redispersible Er^{3+}, Nd^{3+}, and Ho^{3+} Doped LaF3Nanoparticles. Nano Letters. 2002; 2 (7): 733-737.

[81] Di W, Wang X, Chen B, Lu S, Zhao X. Effect of OH^- on the luminescent efficiency and lifetime of Tb^{3+}-doped yttrium orthophosphate synthesized by solution precipitation. The Journal of Physical Chemistry C. 2005; 109 (27): 13154-13158.

[82] Zeng H, Li X, Xie F, Teng L, Chen H. Dextran-coated fluorapatite nanorods doped with lanthanides in labelling and directing osteogenic differentiation of bone marrow mesenchymal stem cells. Journal of Materials Chemistry B. 2014; 2 (23): 3609.

[83] Bose S, Tarafder S. Calcium phosphate ceramic systems in growth factor and drug delivery for bone tissue engineering: a review. Acta Biomaterialia. 2012; 8 (4): 1401-1421.

[84] Bae YM, Park YI, Nam SH, Kim JH, Lee K, Kim HM, et al. Endocytosis, intracellular transport, and exocytosis of lanthanide-doped upconverting nanoparticles in single living cells. Biomaterials. 2012; 33 (35): 9080-9086.

[85] Lencer WI, Weyer P, Verkman AS, Ausiello DA, Brown D. FITC-dextran as a probe for endosome function and localization in kidney. American Journal of Physiology - Cell Physiology. 1990; 258 (2): C309-C317.

[86] Escudero A, Calvo ME, Rivera-Fernandez S, de la Fuente JM, Ocana M. Microwave-assisted synthesis of biocompatible europium-doped calcium hydroxyapatite and fluoroapatite luminescent nanospindles functionalized with poly(acrylic acid). Langmuir. 2013; 29 (6): 1985-1994.

[87] Hui J, Zhang X, Zhang Z, Wang S, Tao L, Wei Y, et al. Fluoridated HAp:Ln^{3+} (Ln = Eu or Tb) nanoparticles for cell-imaging. Nanoscale. 2012; 4 (22): 6967-6970.

[88] Li L, Liu Y, Tao J, Zhang M, Pan H, Xu X, et al. Surface Modification of Hydroxyapatite Nanocrystallite by a Small Amount of Terbium Provides a Biocompatible Fluorescent Probe. The Journal of Physical Chemistry C. 2008; 112 (32): 12219-12224.

[89] Auzel F. Upconversion and anti-Stokes processes with f and d ions in solids. Chemical Reviews. 2004; 104 (1): 139-173.

[90] Chen Z, Chen H, Hu H, Yu M, Li F, Zhang Q, et al. Versatile synthesis strategy for carboxylic acid-functionalized upconverting nanophosphors as biological labels. Journal of the American Chemical Society. 2008; 130 (10): 3023-3029.

[91] Mullen TJ, Zhang M, Feng W, El-khouri RJ, Sun LD, Yan CH, et al. Fabrication and characterization of rare-earth-doped nanostructures on surfaces. ACS Nano. 2011; 5 (8): 6539-6545.

[92] Yi G, Peng Y, Gao Z. Strong Red-Emitting near-Infrared-to-Visible Upconversion Fluorescent Nanoparticles. Chemistry of Materials. 2011; 23 (11): 2729-2734.

[93] Li Z, Zhang Y. Monodisperse silica-coated polyvinylpyrrolidone/$NaYF_4$ nanocrystals with multicolor upconversion fluorescence emission. Angewandte Chemie, International Edition in English. 2006; 45 (46): 7732-7735.

[94] Liu Y, Chen M, Cao T, Sun Y, Li C, Liu Q, et al. A cyanine-modified nanosystem for in vivo upconversion luminescence bioimaging of methylmercury. Journal of the American Chemical Society. 2013; 135 (26): 9869-9876.

[95] Chen H, Banaszak Holl M, Orr BG, Majoros I, Clarkson BH. Interaction of dendrimers (artificial proteins) with biological hydroxyapatite crystals. Journal of Dental Research. 2003; 82 (6): 443-448.

[96] Sun Y, Yang H, Tao D. Preparation and characterization of Eu^{3+}-doped fluorapatite nanoparticles by a hydrothermal method. Ceramics International. 2012; 38 (8): 6937-6941.

[97] Wang C, Cheng L, Xu H, Liu Z. Towards whole-body imaging at the single cell level using ultra-sensitive stem cell labeling with oligo-arginine modified upconversion nanoparticles. Biomaterials. 2012; 33 (19): 4872-4881.

[98] Wang X, Zhuang J, Peng Q, Li Y. A general strategy for nanocrystal synthesis. Nature. 2005; 437 (7055): 121-124.

[99] Zhang XX, Hong P, Bass M, Chai BHT. Ho^{3+} to Yb^{3+} back transfer and thermal quenching of upconversion green emission in fluoride crystals. Applied Physics Letters. 1993; 63 (19): 2606-2608.

[100] Sangeetha NM, van Veggel FCJM. Lanthanum Silicate and Lanthanum Zirconate Nanoparticles Co-Doped with $Ho^{3+}$and Yb^{3+}: Matrix-Dependent Red and Green Upconversion Emissions. The Journal of Physical Chemistry C. 2009; 113 (33): 14702-14707.

[101] Hu X, Zhu J, Li X, Zhang X, Meng Q, Yuan L, et al. Dextran-coated fluorapatite crystals doped with Yb^{3+}/Ho^{3+} for labeling and tracking chondrogenic differentiation

of bone marrow mesenchymal stem cells in vitro and in vivo. Biomaterials. 2015; 52 (0): 441-451.

[102] Liu Y, Lim J, Teoh SH. Review: development of clinically relevant scaffolds for vascularised bone tissue engineering. Biotechnology Advances. 2013; 31 (5): 688-705.

[103] Zhou H, Lee J. Nanoscale hydroxyapatite particles for bone tissue engineering. Acta Biomaterialia. 2011; 7 (7): 2769-2781.

[104] Curtin CM, Cunniffe GM, Lyons FG, Bessho K, Dickson GR, Duffy GP, et al. Innovative collagen nano-hydroxyapatite scaffolds offer a highly efficient non-viral gene delivery platform for stem cell-mediated bone formation. Advanced Materials. 2012; 24 (6): 749-754.

[105] Liu J, Wang X, Jin Q, Jin T, Chang S, Zhang Z, et al. The stimulation of adipose-derived stem cell differentiation and mineralization by ordered rod-like fluorapatite coatings. Biomaterials. 2012; 33 (20): 5036-5046.

[106] Yang P, Quan Z, Li C, Kang X, Lian H, Lin J. Bioactive, luminescent and mesoporous europium-doped hydroxyapatite as a drug carrier. Biomaterials. 2008; 29 (32): 4341-4347.

[107] Chen F, Huang P, Zhu YJ, Wu J, Zhang CL, Cui DX. The photoluminescence, drug delivery and imaging properties of multifunctional Eu^{3+}/Gd^{3+} dual-doped hydroxyapatite nanorods. Biomaterials. 2011; 32 (34): 9031-9039.

[108] Li X, Zeng H, Teng L, Chen H. Comparative investigation on the crystal structure and cell behavior of rare-earth doped fluorescent apatite nanocrystals. Materials Letters. 2014; 125 (0): 78-81.

[109] Li X, Zhu J, Man Z, Ao Y, Chen H. Investigation on the structure and upconversion fluorescence of Yb^{3+}/Ho^{3+} co-doped fluorapatite crystals for potential biomedical applications. Scientific Reports. 2014; 4: 4446.

[110] Gouveia-Neto AS, Bueno LA, Afonso ACM, Nascimento JF, Costa EB, Messaddeq Y, et al. Upconversion luminescence in Ho^{3+}/Yb^{3+}- and Tb^{3+}/Yb^{3+}-codoped fluorogermanate glass and glass ceramic. Journal of Non-Crystalline Solids. 2008; 354 (2-9): 509-514.

[111] He F, Yang P, Wang D, Li C, Niu N, Gai S, et al. Preparation and up-conversion luminescence of hollow La_2O_3:Ln (Ln = Yb/Er, Yb/Ho) microspheres. Langmuir. 2011; 27 (9): 5616-5623.

[112] Dong H, Sun LD, Yan CH. Energy transfer in lanthanide upconversion studies for extended optical applications. Chemical Society Reviews. 2015; 44 (6): 1608-1634.

[113] Dong H, Du SR, Zheng XY, Lyu GM, Sun LD, Li LD, et al. Lanthanide Nanoparticles: From Design toward Bioimaging and Therapy. Chemical Reviews. 2015; 115 (19): 10725-10815.

[114] Chung JH, Ryu JH, Lee SY, Lee JH, Choi BG, Shim KB. Yellow lighting upconversion from Yb^{3+}/Ho^{3+} co-doped $CaMoO_4$. Materials Research Bulletin. 2012; 47 (8): 1991-1995.

[115] Gavrilović TV, Jovanović DJ, Trandafilović LV, Dramićanin MD. Effects of Ho^{3+} and Yb^{3+} doping concentrations and Li^{+} co-doping on the luminescence of $GdVO_4$ powders. Optical Materials. 2015; 45: 76-81.

[116] Dong H, Sun LD, Yan CH. Basic understanding of the lanthanide related upconversion emissions. Nanoscale. 2013; 5 (13): 5703-5714.

[117] Le AX, Miclau T, Hu D, Helms JA. Molecular aspects of healing in stabilized and non-stabilized fractures. Journal of Orthopaedic Research. 2001; 19 (1): 78-84.

[118] Oryan A, Monazzah S, Bigham-Sadegh A. Bone injury and fracture healing biology. Biomedical and Environmental Sciences. 2015; 28 (1): 57-71.

[119] Dimitriou R, Jones E, McGonagle D, Giannoudis PV. Bone regeneration: current concepts and future directions. BMC Medicine. 2011; 9 (1): 66.

[120] Ohba S, Yano F, Chung U-i. Tissue engineering of bone and cartilage. IBMS BoneKEy. 2009; 6 (11): 405-419.

[121] Lanza R, Langer R, Vacanti J. Principles of Tissue Engineering. 2nd ed: Academic Press; 2000.

[122] Matthews JA, Wnek GE, Simpson DG, Bowlin GL. Electrospinning of collagen nanofibers. Biomacromolecules. 2002; 3 (2): 232-238.

[123] Jia B, Li Y, Yang B, Xiao D, Zhang S, Rajulu AV, et al. Effect of microcrystal cellulose and cellulose whisker on biocompatibility of cellulose-based electrospun scaffolds. Cellulose. 2013; 20 (4): 1911-1923.

[124] Rnjak-Kovacina J, Wise SG, Li Z, Maitz PK, Young CJ, Wang Y, et al. Electrospun synthetic human elastin:collagen composite scaffolds for dermal tissue engineering. Acta Biomaterialia. 2012; 8 (10): 3714-3722.

[125] Jin HJ, Chen J, Karageorgiou V, Altman GH, Kaplan DL. Human bone marrow stromal cell responses on electrospun silk fibroin mats. Biomaterials. 2004; 25 (6): 1039-1047.

[126] Giannoudis PV, Dinopoulos H, Tsiridis E. Bone substitutes: an update. Injury. 2005; 36 (3): S20-27.

[127] Puppi D, Chiellini F, Piras AM, Chiellini E. Polymeric materials for bone and cartilage repair. Progress in Polymer Science. 2010; 35 (4): 403-440.

[128] Liu W, Thomopoulos S, Xia Y. Electrospun nanofibers for regenerative medicine. Advanced Healthcare Materials. 2012; 1 (1): 10-25.

[129] Hutmacher DW. Scaffolds in tissue engineering bone and cartilage. Biomaterials. 2000; 21 (24): 2529-2543.

[130] Sultana N, Hassan MI, Lim MM. Composite Synthetic Scaffolds for Tissue Engineering and Regenerative Medicine. 1st ed: Springer International Publishing; 2015.

[131] Agarwal S, Wendorff JH, Greiner A. Progress in the field of electrospinning for tissue engineering applications. Advanced Materials. 2009; 21 (32-33): 3343-3351.

[132] Fukushima K, Feijoo JL, Yang M-C. Comparison of abiotic and biotic degradation of PDLLA, PCL and partially miscible PDLLA/PCL blend. European Polymer Journal. 2013; 49 (3): 706-717.

[133] Lee HW, Seo SH, Kum CH, Park BJ, Joung YK, Son TI, et al. Fabrication and characteristics of anti-inflammatory magnesium hydroxide incorporated PLGA scaffolds formed with various porogen materials. Macromolecular Research. 2013; 22 (2): 210-218.

[134] Kasuga T, Nogami M, Niinomi M, Hattori T. Bioactive calcium phosphate invert glass-ceramic coating on β-type Ti–29Nb–13Ta–4.6Zr alloy. Biomaterials. 2003; 24 (2): 283-290.

[135] Hench LL. An Introduction to Bioceramics. Second edition ed: Imperial College Press; 2013.

[136] Kawai T, Takemoto M, Fujibayashi S, Tanaka M, Akiyama H, Nakamura T, et al. Comparison between alkali heat treatment and sprayed hydroxyapatite coating on thermally-sprayed rough Ti surface in rabbit model: Effects on bone-bonding ability and osteoconductivity. Journal of Biomedical Materials Research, Part B: Applied Biomaterials. 2015; 103 (5): 1069-1081.

[137] Piétrement O, Jallot E. AFM mechanical mapping at the interface between a bioactive glass coating and bone. Nanotechnology. 2002; 13 (1): 18.

[138] Li X, Xie J, Lipner J, Yuan X, Thomopoulos S, Xia Y. Nanofiber scaffolds with gradations in mineral content for mimicking the tendon-to-bone insertion site. Nano Letters. 2009; 9 (7): 2763-2768.

[139] Holly Shearer, Marianne J. Ellis, Semali P. Perera, Chaudhuri JB. Effects of Common Sterilization Methods on the Structure and Properties of Poly(D,L Lactic-Co-Glycolic Acid) Scaffolds Tissue Engineering. 2006; 12 (10): 2717-2727.

[140] Sabir MI, Xu X, Li L. A review on biodegradable polymeric materials for bone tissue engineering applications. Journal of Materials Science. 2009; 44 (21): 5713-5724.

[141] Olszta MJ, Cheng X, Jee SS, Kumar R, Kim Y-Y, Kaufman MJ, et al. Bone structure and formation: A new perspective. Materials Science and Engineering: R: Reports. 2007; 58 (3-5): 77-116.

PUBLICATIONS

1. Li, X.; Zeng, H.; Teng, L.; Chen, H. Comparative investigation on the crystal structure and cell behavior of rare-earth doped fluorescent apatite nanocrystals. Materials Letters 2014, 125, 78-81.
2. Li, X.; Zhu, J.; Man, Z.; Ao, Y.; Chen, H. Investigation on the structure and upconversion fluorescence of Yb^{3+}/Ho^{3+} co-doped fluorapatite crystals for potential biomedical applications. Scientific Reports 2014, 4, 4446.
3. Zeng, H.; Li, X.; Xie, F.; Teng, L.; Chen, H. Dextran-coated fluorapatite nanorods doped with lanthanides in labelling and directing osteogenic differentiation of bone marrow mesenchymal stem cells. Journal of Materials Chemistry B 2014, 2 (23), 3609-3617.
4. Hu, X.; Zhu, J.; Li, X.; Zhang, X.; Meng, Q.; Yuan, L.; Zhang, J.; Fu, X.; Duan, X.; Chen, H.; Ao, Y. Dextran-coated fluorapatite crystals doped with Yb^{3+}/Ho^{3+} for labeling and tracking chondrogenic differentiation of bone marrow mesenchymal stem cells *in vitro* and *in vivo*. Biomaterials 2015, 52, 441-451.
5. Liu, W.; Lipner, J.; Moran, C. H.; Feng, L.; Li, X.; Thomopoulos, S.; Xia, Y. Generation of Electrospun Nanofibers with Controllable Degrees of Crimping Through a Simple, Plasticizer-Based Treatment. Advanced Materials 2015, 27 (16), 2583-258.
6. Li, X.; Chen, H. Lanthanide Yb^{3+}/Ho^{3+} co-doped apatite nanoparticles with upconversion luminescence for tracking of *in vivo* materials. In submission.

VITA

Xiyu Li

Xiyu was born in Chengdu, Sichuan, China. He attended public schools in Chengdu, Sichuan, received a B.A. in Chemistry from Sichuan University, China in 2011 before coming to Peking University to pursue a doctorate in Biomedical Engineering (Georgia Tech/Emory/Peking University joint Ph.D. program). When he is not working on his research, Mr. Li enjoys taking photos and travelling.